ANATOMY-WISE COMPUTED TOMOGRAPHY-DERIVED LUNG VENTILATION IMAGING FOR PRECISE FUNCTIONAL LUNG AVOIDANCE RADIATION THERAPY

CHEN ZHI

PhD

The Hong Kong Polytechnic University

2025

The Hong Kong Polytechnic University

Department of Health Technology and Informatics

ANATOMY-WISE COMPUTED TOMOGRAPHY-DERIVED LUNG VENTILATION IMAGING FOR PRECISE FUNCTIONAL LUNG AVOIDANCE RADIATION THERAPY

CHEN ZHI

A thesis submitted in partial fulfilment of the requirements

for the degree of Doctor of Philosophy

Dec 2024

CERTIFICATE OF ORIGINALITY

I hereby declare that this thesis is my own work and that, to the best of my knowledge and belief, it reproduces no material previously published or written, nor material that has been accepted for the award of any other degree or diploma, except where due acknowledgement has been made in the text.

_____ (Signed)

CHEN Zhi (Name of student)

Abstract

Background: Functional lung avoidance radiotherapy (FLART) is an innovative approach aimed at preserving lung function during treatment planning. It achieves this by minimizing radiation exposure to the high functional volume (HFV) of the lung. To create an accurate treatment plan, FLART combines functional lung images (ventilation/perfusion images). However, the current standard clinical techniques for lung ventilation imaging rely on radioactive gases or aerosols, such as Single Photon Emission Computed Tomography (SPECT) with Tc-99m or Positron Emission Tomography (PET) with Ga-68. While effective in assessing pre-treatment pulmonary function, these methods require additional imaging scans and the injection of radioactive material, resulting in extra costs and radiation dose.

Purpose: To propose an anatomy-wise lung ventilation imaging method ($CTVI_{AW}$) that integrates information from lung parenchyma and tumor-blocked pulmonary segments based on planning computed tomography (CT) images for FLART.

Methods and materials: Our study involves the development and application of the $CTVI_{AW}$ method in radiotherapy treatment planning. In the first part, $CTVI_{AW}$ was developed by considering the underlying causes of impaired pulmonary ventilation, specifically pulmonary parenchymal injury and airway blockages. First, an Atlas-based method was developed to divide the lung volume into 18 pulmonary segments. Then, each segment was visually inspected to determine if the connected airway branch was blocked. The blocked segments were considered functionally

lost (assigned a value of 0). For unblocked segments, we used a super-voxel-based method to assess functional ability of the pulmonary parenchymal to generate the final $CTVI_{AW}$. To evaluate the accuracy of our Atlas-based pulmonary segments segmentation, we utilized CT images from 150 patients as a patient library to generate pulmonary segmentations using a bronchial tree-based method. Additionally, we manually segmented pulmonary segments in 14 patients and used them as a reference for comparison (using the Dice similarity coefficient index, DSC). For $CTVI_{AW}$ evaluation, we analyzed 66 patients who had 4DCT and SPECT/PET as lung references ventilation images (RefVI). The Spearman's correlation coefficient was calculated to assess the similarities between $CTVI_{AW}$ and the RefVI. Out of the sixty-six patients, eleven exhibited airway blockages caused by tumors. These tumor-blocked segments were then compared to the low functional volume (LFV) obtained from the RefVI for these specific eleven patients. In the second part, the $CTVI_{AW}$ was employed to guide treatment planning. The lung was further divided into HFV, recoverable LFV (rLFV, tumor-blocked segments with potential high functional value by analyzing with super-voxel-based method), and unrecoverable LFV (uLFV, the remaining LFV) instead of the traditional HFV and LFV volumes. The rLFV requires protection as the HFV during the planning. Five patients underwent weekly 4DCT and found with tumor shrinkage were selected to create three intensity-modulated photon plans to evaluate the efficiency of our plan strategy: an anatomical-based plan (aPlan), a functional-guided plan (fPlan) that considered only HFV, and a functional-guided plan (rfPlan) that protected both HFV and rLFV.

Results: For the pulmonary segments segmentation, the Atlas-based method achieved

a mean DSC value of 0.70 ± 0.11 for left lung and 0.72 ± 0.11 for the right lung when compared to manual segmentations. The LFV in the RefVI and the tumor-blocked segments had a high overlap similarity coefficient value of 0.90 ± 0.07. The novel $CTVI_{AW}$ method demonstrated a mean Spearman's correlation coefficient of 0.59 (range: 0.31 to 0.82) with the RefVI. For the 11 patients with tumor-blocked segments, the mean Spearman correlation between $CTVI_{AW}$ and RefVI was 0.72 ± 0.05. This correlation was higher than the correlation between the super-voxel-based method ($CTVI_{svd}$, without considering the airway blockage) and RefVI (0.51± 0.14). For the comparison of the five patients' treatment plans, the V5, V20 and mean dose of the HFV in fPlan were 10.6% ± 25.3%, 14.3% ± 9.5%, and 10.0% ± 9.3% lower, respectively, than those in aPlan. The overall HFV dose in the recoverable functional-guided plan (rfPlan) was similar to that in fPlan. By incorporating dose constraints for rLFV, the dose of rLFV in rfPlan was lower than in both fPlan and aPlan. Specifically, the V5, V20, and mean dose of rLFV in rfPlan were lower than in aPlan by 0.3% ± 0.5%, 12.1% ± 8.4%, and 13.0% ± 6.4%, respectively. Notably, these parameters in rfPlan were substantially lower than in fPlan by 1.0% ± 2.1%, 14.9% ± 9.8%, and 15.9% ± 6.5%, respectively. Regarding other evaluation parameters, all three plans showed comparable results and remained within tolerance.

Conclusions: In this study, we developed a novel anatomy-wise lung ventilation imaging method to generate surrogate ventilation images directly from CT images for precise functional lung avoidance radiotherapy planning. Unlike traditional methods, $CTVI_{AW}$ considers both air transport and lung parenchymal features, providing a comprehensive understanding of impaired lung ventilation. Importantly, during

treatment planning, $CTVI_{AW}$ can be used to identify and reduce radiation dose to the potential recoverable region. This region may regain high function if the tumor shrinks post-treatment. This is the first time that recoverable regions have been incorporated into the treatment planning process, potentially preserving more lung function for patients. The findings contribute to the development of personalized and precise treatment planning methods.

Publications during PhD study

Journal articles:

1. **Chen, Z.**, Huang, Y. H., Kong, F. M., Ho, W. Y., Ren, G., & Cai, J. (2023). A super-voxel-based method for generating surrogate lung ventilation images from CT. Frontiers in Physiology (IF: 3.89), DOI:10.3389/fphys.2023.1085158.

2. **Chen, Z.**, Wo, B. W. B., Chan, O. L., Huang, Y. H., Teng, X., Zhang, J., Dong, Y., Xiao, L., Ren, G., & Cai, J. (2024). Deep learning-based bronchial tree-guided semi-automatic segmentation of pulmonary segments in computed tomography images. Quantitative Imaging in Medicine and Surgery (IF: 2.87), DOI:10.21037/qims-23-1251

3. **Chen, Z.**, Li, Z., Huang, Y. H., Teng, X., Zhang, J., Xiong, T., Dong, Y., Song, L., Ren, G., & Cai, J. (2025) Anatomy-Wise Lung Ventilation Imaging for Precise Functional Lung Avoidance Radiation Therapy. Physics in Medicine & Biology (IF: 3.44) DOI: 10.1088/1361-6560/adb123

4. Ma, P., **Chen, Z.**, Huang, Y. H., Zhao, M., Li, W., Li, H., Cao, D., Jiang, Y., Zhou, T., Cai, J., & Ren, G. (2025) Motion and Anatomy Dual Aware Lung Ventilation Imaging by Integrating Jacobian Map and Average CT Image Using Dual Path Fusion Network. Medical Physics (IF: 3.75) DOI: 10.1002/mp.17466 (Co-first author)

5. Huang, Y. H., Teng, X., Zhang, J., **Chen, Z.**, Ma, Z., Ren, G., Ge, H., & Cai, J. (2023). Respiratory Invariant Textures From Static Computed Tomography

Scans for Explainable Lung Function Characterization. Journal of Thoracic Imaging (IF: 3.40), DOI:10.1097/RTI.0000000000000717.

6. Li, W., Zhao, D., Zeng, G., **Chen, Z.**, Huang, Z., Lam, S., Cheung, A. L., Ren, G., Liu, C., Liu, X., Lee, F. K. H., Au, K. H., Lee, V. H. F., Xie, Y., Qin, W., Cai, J., & Li, T. (2024). Evaluating Virtual Contrast-enhanced MRI (VCE-MRI) in Nasopharyngeal Carcinoma Radiotherapy: A Retrospective Analysis for Primary Gross Tumor Delineation. International Journal of Radiation Oncology, Biology, Physics. (IF: 7.0) DOI:10.1016/j.ijrobp.2024.06.015.

7. Xiong, T., Zeng, G., **Chen, Z.**, Huang, Y. H., Li, B., Liu, X., Sheng, Y., Ren, G., Wu, Q., Ge, H., & Cai, J. (2024) Automatic planning based on function-guided beam angle selection and plan optimization for functional lung avoidance radiotherapy. Physics in Medicine & Biology (IF: 3.44) DOI: 10.1088/1361-6560/ad5ef5.

8. Li, Z., Zhao, M., Li, Z., Huang, Y. H., **Chen, Z.**, Pu, Y., Zhao, M., Liu, X., Wang, M., Wang, K., Yeung, M. H. Y., Geng, L., Cai, J., Zhang, W., Yang, R., & Ren, G. (2024) Quantitative texture analysis using machine learning for predicting interpretable pulmonary perfusion from non-contrast computed tomography in pulmonary embolism patients. Respiratory Research, (IF: 4.7) DOI: 10.1039/d3mo00214d.

9. Huang, Y. H., Teng, X., Xiong, T., **Chen, Z.**, Li, B., Lou, Z., Dong, Y., Teng, X., Ma, Z., Ge, H., Ren, G., & Cai, J. (2025) Constructing Surrogate Lung Ventilation Maps from 4DCT-derived Subregional Respiratory Dynamics. International Journal of Radiation Oncology, Biology, Physics. (IF: 7.0) DOI:

10.1016/j.ijrobp.2024.11.074

10. Xiong, T., Zeng, G., **Chen, Z.**, Huang, Y. H., Li, B., Zhou, D., Sheng, Y., Ren, G., Wu, Q., Ge, H., & Cai, J. Automatic lung dose painting for functional lung avoidance radiotherapy through multi-modality-guided dose prediction. International Journal of Radiation Oncology, Biology, Physics. (IF: 7.0) (under review)

Conference abstract:

1. **Chen, Z.**, Huang, Y., Ren, G., & Cai, J. A Novel Super-Voxel Method for Generating Robust Lung Ventilation Image From CT. 2022 AAPM Annual meeting, Washington, DC, United State. (Abstract).

2. **Chen, Z.**, Huang, Y. H., Teng, X., Zhang, J., Dong, Y., Kong, F. M., Ho, W. Y., Ren, G., & Cai, J. Atlas-Based Auto-Segmentation of Bronchopulmonary Segments for Functional Lung Avoidance Radiation Therapy. 2023 AAPM Annual meeting, Houston, TX, United State. (Abstract)

3. **Chen, Z.**, Huang, Y. H., Xiong, T., Li, B., Ge, H., Ren, G., & Cai, J. Identifying temporary defected lung regions for functional lung avoidance-based intensity modulated proton therapy for lung cancer. 2024 Annual PTCOG Conference (Abstract)

Acknowledgement

First and foremost, I extend my deepest gratitude to my chief supervisor, Prof. Jing Cai, and co-supervisor, Dr. Ge Ren for their support, guidance, and encouragement throughout my PhD journey. Besides, I would like to express my special thanks to Dr. Jing Cai. His expertise and constructive feedback significantly contributed to the quality of this thesis. It has been an honor and joy to study under his guidance. I will always treasure the knowledge and diligence he shared with me.

Then, I want to express my heartfelt thanks to my group members. Their selfless assistance, camaraderie, and shared experiences have made this PhD period memorable.

Next, I would like to give many thanks to HTI staffs for their constant assistances.

After that, I would like to give special thanks to the friends and teachers that I have met for their help, support, suggestions, and encouragements.

Lastly, I owe a debt of gratitude to my parents and my brother and sisters. Their silent but steadfast support over the years has been my anchor. Their understanding, trust, and unwavering expectations have fueled my determination to succeed.

Contents

List of Figures

List of Tables

Abbreviation

3DCRT	Three-dimensional conformal radiotherapy
3DCT	Three-dimensional computed tomography
4D-CBCT	Four dimensional cone beam computed tomography
4D-FBCT	Four dimensional fan beam computed tomography
4DCT	Four-dimensional computer tomography
aPlan	Anatomical lung guided plan
ATM22	Airway tree modeling challenge 2022
BHCT	Breath-hold CT
BT	Bronchial tree
CFRT	Conventionally fractionated radiation therapy
COPD	Chronic obstructive pulmonary disease
CT	Computed tomography
CT_{ex}	Peak-exhale phase computed tomography
CT_{in}	Peak-inhale phase computed tomography
CTVI	Computed tomography-derived ventilation imaging
$CTVI_{AW}$	Four dimensional fan beam computed tomography
$CTVI_{HU}$	Hounsfield unit-based computed tomography-derived ventilation imaging

$CTVI_{Jac}$	Jacobian-based computed tomography-derived ventilation imaging
$CTVI_{SVD}$	Super-voxel-based computed tomography-derived ventilation imaging
$CTVI_{SVHU}$	Super-voxel-based hounsfield unit-based computed tomography-derived ventilation imaging
$CTVI_{SVJac}$	Super-voxel-based jacobian-based computed tomography-derived ventilation imaging
D_{mean}	Mean density value
DIR	Deformable image registration
DSC	Dice similarity coefficient
DSC_h	Dice similarity coefficient value of the high functional volume
DSC_l	Dice similarity coefficient value of the low functional volume
DTPA	Diethylenetriamine pentaacetate
DVF	Deformable vector field
DVH	Dose volume histogram
FLART	Functional lung avoidance radiotherapy
fMLD	Functional-weighted mean lung dose
fPlan	Functional lung guided plan
fVx	Functional-weighted volume receiving more than x Gy

GLCOM	Gray-level co-occurrence matrix
GLRLM	Gray-level run length matrix
HD95	Robust hausdroff distance (95^{th} percentile of the surface distances)
HFV	High functional volume
HRCT	High resolution computed tomography
HU	Hounsfield unit
IJF	Integrated jacobian formulation
IMPT	Intensity modulated proton therapy
IMRT	Intensity modulated radiation therapy
LFV	Low functional volume
LLL	Left lower lobe
LUL	Left upper lobe
MCVC	Mass conserving volume change
MLD	Mean lung dose
MRI	Magnetic resonance imaging
MSD	Mean surface distance
NCCN	National Comprehensive Cancer Network
NSCLC	Non-small cell lung cancer

OAR	Organ at risk
OS	Overall survival
OSC	Overlap similarity coefficient
PA	Pulmonary arteries
PET	Positron emission tomography
PTV	Planning target volume
RefVI	Reference ventilation image
RF	Radiation fibrosis
rfPlan	Recoverable functional lung guided plan
RILI	Radiation-induced lung injuries
rLFV	Recoverable low functional volume
RLL	Right lower lobe
RML	Right middle lobe
RP	Radiation pneumonitis
RT	Radiotherapy
RTOG	Radiation therapy oncology group
RUL	Right upper lobe
SABR	Stereotactic ablative radiation therapy

SBRT	Stereotactic body radiation therapy
SLIC	Simple linear iterative clustering
sMLD	Mean lung dose of the high functional volume
SPECT	Single photon emission computed tomography
sVx	High functional volume receiving more than x Gy
TCIA	The cancer imaging archive
TPS	Treatment planning system
uLFV	Unrecoverable low functional volume
V/Q	Ventilation/perfusion
$\text{Vent}_{\text{mean}}$	Mean ventilation value
VMAT	Volumetric modulated arc therapy
Vx	Volume receiving more than x Gy

1 Introduction

1.1 Radiotherapy for lung cancer

Lung cancer, with an estimated 2.5 million new cases and 1.8 million deaths in 2022, is the most commonly diagnosed malignant disease in both men and women [1]. Radiotherapy (RT) is an important treatment modality for lung cancer patients, with evidence-based indications for 77% of patients with lung cancer [2, 3]. RT can be used for curative or palliative treatment in all stages of the disease. For early-stage (stage I-II) non-small cell lung cancer (NSCLC), RT can be used as one of the primary modes of treatment, particularly for those who are unsuitable or unwilling to undergo surgery, according to the National Comprehensive Cancer Network (NCCN) guidelines [4]. Although stereotactic ablative RT (SABR) is not equivalent to lobectomy, some prospective series have demonstrated similar overall and cancer-specific survival [5–7]. A combination of radiation and chemotherapy is often employed for stage III or higher. Treatment options for advanced or metastatic disease may include targeted therapy or immunotherapy based on the identification of specific biomarkers. However, these targeted therapy or immunotherapy may result in significant adverse effects, owing to the heightened sensitivity of both the tumor and healthy organs to radiation in conjunction with other treatments. Consequently, the implementation of precise radiation therapy is imperative to ensure optimal protection of vital organs, such as the lungs.

The administration of RT for the management of lung cancer poses several challenges, particularly concerning ensuring efficacious tumor control while safeguarding vital organs. Radiation-induced lung injury is a significant concern in cancer treat-

ment, leading to treatment-related morbidity. After lung radiation therapy, up to 15-40% of patients experience clinically significant radiation pneumonitis (RP) [8]. Unfortunately, these side effects adversely impact patient survival rates. The development of RP was associated with reduced survival, decreasing from 29 months to 8 months [9]. Additionally, the damaged lung tissue cannot be repaired, further diminishing the patient's quality of life [10, 11]. The Radiation Therapy Oncology Group (RTOG) 0617 clinical trial has demonstrated that increasing dosage to target areas may not necessarily translate into improved overall survival (OS) rates [12]. Such an approach may increase the risk of patient mortality due to severe side effects. Thus, it is imperative to accurately identify and selectively administer an augmented dosage to high-risk target areas. Furthermore, the uneven distribution of pulmonary function in patients induced by underlying conditions necessitates the identification of normal lung areas for protection, thereby minimizing the risk of post-treatment lung function impairment and enhance the quality of care delivered to patients.

The functional lung volume that can be irradiated in such patients is limited, as irradiation of functioning tissue can lead to RP and respiratory failure. Currently, the percentage of the lung volume receiving at least 20 Gy ($V20$) and the mean lung dose (MLD) are used to predict the risk of pulmonary injury [13] or the maximum acceptable dose to deliver to a lesion [14]. However, these parameters are evaluated across the whole lung volume and do not account for functional differences between lung regions. Recently, regional lung functionality assessment has been shown to enable highly functional lung areas to be spared from irradiation and thus can be used to design treatment plans that reduce the risk of injury [15–18].

1.2 Functional image in radiotherapy for lung cancer

The functional ventilation/perfusion images have been utilized for evaluating the function lost caused by the RT. Studies found a linear relationship between reductions in ventilation and perfusion and the dose [19, 20]. Boersma et al. [19] found that the estimated mean relative reduction of local perfusion or ventilation can predict the change in overall lung function within 10% of the actual values in 63% to 73% of breast patients. In 2000, Seppenwoolde et al. [21] applied the dose-effect relations on lung cancer. They found that well-perfused lung regions showed the same effects as breast cancer, while poorly perfused regions showed less damage than predicted. This could be the reason for the reperfusion effect in hypoperfused regions caused by the tumor obstruction subsequent to radiation therapy. In 2018, Owen et al. [22] modeled a patient-specific dose function response for lung cancer. They also found that voxels with initially higher functioning are damaged at a higher rate than lower functioning ones. These studies reveal that voxels with higher doses can experience a significant reduction in function.

Since function reduction can be caused by RT, functional (ventilation/perfusion) images have been utilized for functional lung avoidance RT (FLART). In 1992, Marks et al. [23] were the first to propose using perfusion imaging for treatment planning to optimize beam angle selection and reduce dose to high functional regions. In 2002, Seppenwoolde et al. [23] used lung perfusion imaging directly for plan optimization to reduce function-weighted V20 ($fV20$) and function-weighted mean lung dose ($fMLD$). They discovered that patients with large defect regions could benefit most from applying perfusion imaging. However, the method they used, which involved using the functional map of the entire lung as an input into the optimization

process to give different weights to each voxel, was not supported by the current commercial clinic used treatment planning system (TPS). As a result, researchers had to develop their planning optimization module to realize it, which could hinder the application of functional imaging in clinical planning. In 2005, Christian et al. [24] proposed another method to implement functional information into planning by defining a high functional volume (HFV) with an individual threshold value for each patient and using the HFV for optimization to reduce the $V20$ of the HFV, instead of the whole lung. This method could be implemented in the treatment planning system. After that, several studies [25–30] used different threshold values to divide the lung into well-function and poorly-functioning regions and reduced the dose to the well-functioning region. However, the disadvantage of this approach is that there is no standardized threshold value. Iqbal et al. [31] compared the voxel-based method with the HFV-based method for treatment planning for 19 patients with four-dimensional computed tomography (4DCT) derived ventilation images and concluded that the voxel-based method outperformed the HFV-based method. However, these results might be affected by different factors, such as target size, location of the functional/defect region, and the relation between the tumor and the defect regions.

1.3 Functional lung images

Lung ventilation images can provide regional functional information. Clinical-standard lung ventilation imaging techniques require radioactive gases or aerosols. For example, single photon emission computed tomography (SPECT) uses Technetium-99m (Tc-99m) [32] and positron emission tomography (PET) uses Gallium-68 (Ga-68)

[33]. However, not all hospitals can perform PET or SPECT scans, and the radiopharmaceuticals used for imaging expose patients to additional radiation doses. There are some flaws in these images [34, 35]. First, the images may show anterior–posterior gradient increase, which is likely gravity induced. Second, clumping hotspots could exist in some patients' images. The clinical interpretation of aerosol clumping will depend on the physical properties of the aerosol itself, the presence of lung disease, as well as the respiratory effort of the patient. This could be also caused by the chronic obstructive pulmonary disease (COPD) or the tumor blockage. Although the clumping hotspots show high signal, the around area could be functional defect. These require carefully interpreting the images before apply to the treatment planning design. Hyperpolarized noble gas magnetic resonance imaging (MRI) ventilation [36–39] is another non-invasive imaging technique used to generate ionizing radiation-free ventilation images for lung function assessment. However, MRI ventilation requires a tracer gas and specialized equipment, which may limit the availability of this modality in clinical practice. Computed tomography (CT)-derived ventilation imaging (CTVI) is another method of generating ventilation images. Moreover, as CT scans of patients undergoing RT are routinely performed, CTVI methods could potentially help patients avoid unnecessary radiation doses and medical costs.

1.4 CTVI imaging methods

Current CTVI methods are mainly based on volume changes (Jacobian-based, $\mathrm{CTVI_{Jac}}$ or density changes $\mathrm{CTVI_{HU}}$ and use four-dimensional CT (4DCT) and deformable image registration (DIR) [40]. However, because these methods are performed at the voxel level, their results are substantially affected by image artifacts and DIR

accuracy. Therefore, sub-regional level analysis methods have been developed to improve the accuracy and robustness of CTVI [41, 42]. These methods have yielded some improvements, but they also are DIR-based, which means that their accuracy depends on DIR algorithms; thus, they are affected by the parameters of DIR algorithms and the sensitivity of DIR to 4DCT image artifacts. Other CTVI methods that do not use DIR have been devised. For example, Kipritidis et al. developed a modified Hounsfield unit (HU)-based method [43] that generates robust ventilation images without DIR. However, this method may overestimate areas with edges between solid tissue and normal parenchyma within the lung, such as the peritumoral lung and the pleural space. Some deep learning-based methods can generate highly accurate functional lung images [44–47], but these results lack anatomical explanations.

1.5 Temporary recovery of lung function during/after radiotherapy

Yuan et al. [48], Meng et al. [49], and Kipritidis et al. [50] reported that the function of the lung could vary during the treatment. In addition to designing treatment plans based on functional images before treatment, some studies also obtained functional images during treatment courses for evaluation or adaptive planning. Yuan et al. [48] and Meng et al. [49] published their observations that some patients with centrally located tumors temporarily blocked the airway and caused function lost of the corresponding pulmonary segments. The regions with normal lung parenchyma in the blocked pulmonary segments could re-function after the tumor shrank during the treatment as shown in Figure 1. They suggested that reacquiring the patient's functional image during the treatment can help to alter the treatment planning to

achieve better effectiveness. Their studies indicated insufficient functional planning based on the functional image acquired prior to treatment. Yamamoto et al. [51] acquired two CT scans at two time points (16-20 Gy and 30-34 Gy) during the treatment for adaptive planning. The results showed that functional planning significantly reduced the functional mean lung dose by 5.0% compared to anatomic planning in the adapted scenario. The adaptive re-planning due to the variety in lung function could help patients to preserve more function after the treatment. However, the re-planning process requires additional PET/SPECT, which could aggravate resource scarcity and increase the patient's dose and monetary costs.

As suggested by Yuan's study, the functional lung regions could be divided into four different sections excluding the tumor regions [48]. Region A denotes a complete function impairment caused by COPD or other irreversible diseases. Region B represents reduced pulmonary function induced by unrecoverable diseases. Region C consists of temporarily dysfunctional regions induced by tumor compression or other potentially recoverable diseases. Region D is the normally functioning region. The optimization of the RT plan for these regions could adhere to the following principles: the type A regions, with unrecoverable nonfunctioning "bad" regions, can be given high-dose without causing changes in global pulmonary function; type B regions, with unrecoverable low-functioning regions, may receive high doses (in the absence of a healthier lung region) without causing remarkable changes in global pulmonary function; type C regions should be spared whenever possible and may be given high-dose if they remains nonfunctioning during treatment; the dose to type D regions should be minimized to decrease the occurrence of functionally or clinically significant complications [48].

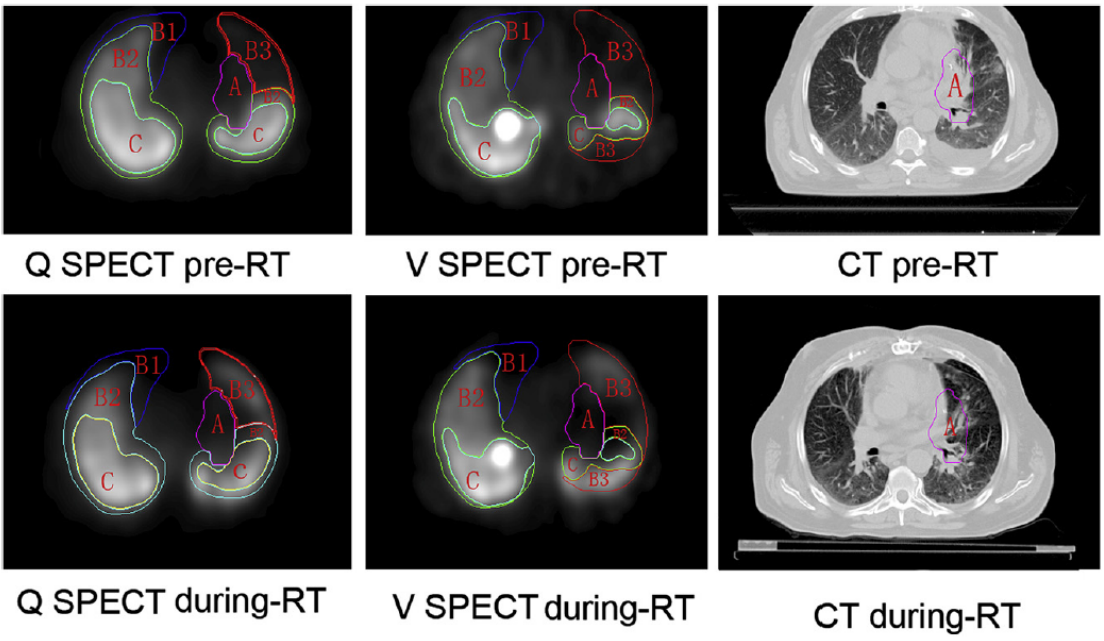

Figure 1: The perfusion (Q) and ventilation (V) functional images change during the radiotherapy treatment course [48]. A is the functional defect region corresponding to the tumor location, B1 is the complete function defect region, B2 is the function reduction induced by some disease, B3 is the temporarily dysfunctional lung induced by tumor or other potentially recoverable diseases, C is the normal lung region. Reproduced with the permission of Ref [48]. copyright © 2012 Elsevier.

1.6 Auto-segmentation of the pulmonary segments

As mentioned above, the tumor obstructs airway could cause the corresponding pulmonary segments function loss[48]. Identification of the blocked segments can help for CTVI generation and further used for treatment planning. The pulmonary segment is considered the fundamental anatomical unit of the lung, possessing its own bronchus, pulmonary arterial and venous systems, and lymphatic systems [52]. The left and right lung can be divided into 18 pulmonary segments. Current auto-segmentation of pulmonary segments rely on airway and vessel segmentation [53–55]. However, for the patients with tumor blockage, the segmentation for airway and vessel could be incomplete due to the tumor blockage, which would compromise the segmentation of the pulmonary segments[55].

1.7 Research gap

Current CTVI methods were based on the mechanism motion of the lung or the features of parenchyma without considering the tumor blockage causing function loss, which could lead to suboptimal results. To identify the blocked regions, a new method that can auto-segment the pulmonary segments without airway and vessel segmentation is needed. In addition, a new method that considers both the features of parenchyma and tumor blockage to generate CTVI is needed.

As mentioned previously that temporary hypo-ventilation regions may occur in certain patients, necessitating careful protection of these regions during treatment planning. Current CTVI-based FLART studies primarily rely on CTVI data acquired before treatment and often employ a simple division of the lung into well-functional and low-functional regions for treatment planning. However, none of them can iden-

tify the temporary hypo-ventilation regions before the treatment to guide the treatment planning, which may result in insufficient protection of these regions. While ART may offer an opportunity to address temporary hypo-ventilation regions in the later stage of the treatment course, potential damage to these regions might have already occurred during the initial stages of treatment. Additionally, implementing ART could exacerbate resource scarcity, increase patient radiation exposure, and incur higher monetary costs. Further research is required to explore methodologies for identifying the four different regions as suggested by Yuan et al.[48], especially the temporarily dysfunctional regions, prior to treatment.

1.8 Research aim and objectives

This study aims to develop an anatomy-wise CTVI method for precise functional lung avoidance treatment planning, utilizing information derived from the lung parenchyma's characteristics and airway transport. Specifically, the study aims to achieve the following three objectives:

1) To develop a new method for auto-segmenting the eighteen pulmonary segments in the lung without airway or vessel segmentation of the lung.

2) To develop an anatomy-wise CTVI method based on the features of lung parenchyma and airway transport.

3) To develop a new strategy for functional avoidance treatment planning based on the features of lung parenchyma and airway transport.

2 Literature Review

2.1 The lung pulmonary segments

2.1.1 The applications of the pulmonary segment

The lungs consist of three lobes in the right lung (upper, middle, and lower) and two lobes in the left lung (upper and lower), which are physically demarcated by fissures. Each lobe is further divided into several pulmonary segments. The right lobes encompass ten segments, while the left lobes encompass eight segments as shown in Figure (2). The pulmonary segment is considered the fundamental anatomical unit of the lung, possessing its own bronchus, pulmonary arterial and venous systems, and lymphatic systems. As a result, individual segments can be surgically excised while preserving the function of neighboring segments [52]. Each of the eighteen lung segments—ten in the right lung and eight in the left is supplied by its own segmental bronchus and a corresponding branch of the pulmonary artery, which ensures both airflow and blood flow to the region. The blood flow basins, or perfusion zones, are closely aligned with these segments, as the pulmonary arteries branch in a pattern that mirrors the bronchial tree.In healthy lungs, blood flow is distributed in a way that matches ventilation, ensuring efficient gas exchange. However, in pathological conditions such as tumor obstruction, this relationship can be disrupted. For example, a tumor compressing a segmental bronchus may impair ventilation in that segment, while the corresponding blood flow basin may remain initially unaffected, leading to a mismatch of ventilation and perfusion.

CT currently serves as the most suitable imaging modality for early detection examinations of lung cancer due to its exceptional spatial resolution and contrast

resolution that enable the precise visualization of the chest's anatomical structures. Radiologists, pulmonologists, and surgeons use pulmonary segments as a reference to determine the location of lung lesions. The accurate identification and visualization of these segmental structures enhance the reliability and precision of individualized treatment plans (e.g., resection by lobectomy or segmentectomy). Several studies have shown that segmentectomy helps to maintain lung parenchyma and preserves 2–3.5% higher lung function in patients with early stage lung cancer while achieving a similar overall survival rate to that of lobectomy [56, 57].

Additionally, segmentation of pulmonary segments has the potential to be useful in radiation therapy. The segmentation of pulmonary segments could also help in FLART. Research indicates that certain regions may regain function after radiotherapy in patients with central tumors [48]. This phenomenon occurs when the tumor obstructs the airway prior to treatment, subsequently shrinking post-treatment and allowing for the re-ventilation of the corresponding region. The identification of segments on a patient's diagnostic high-resolution CT can help to identify temporarily hypo-ventilated regions.

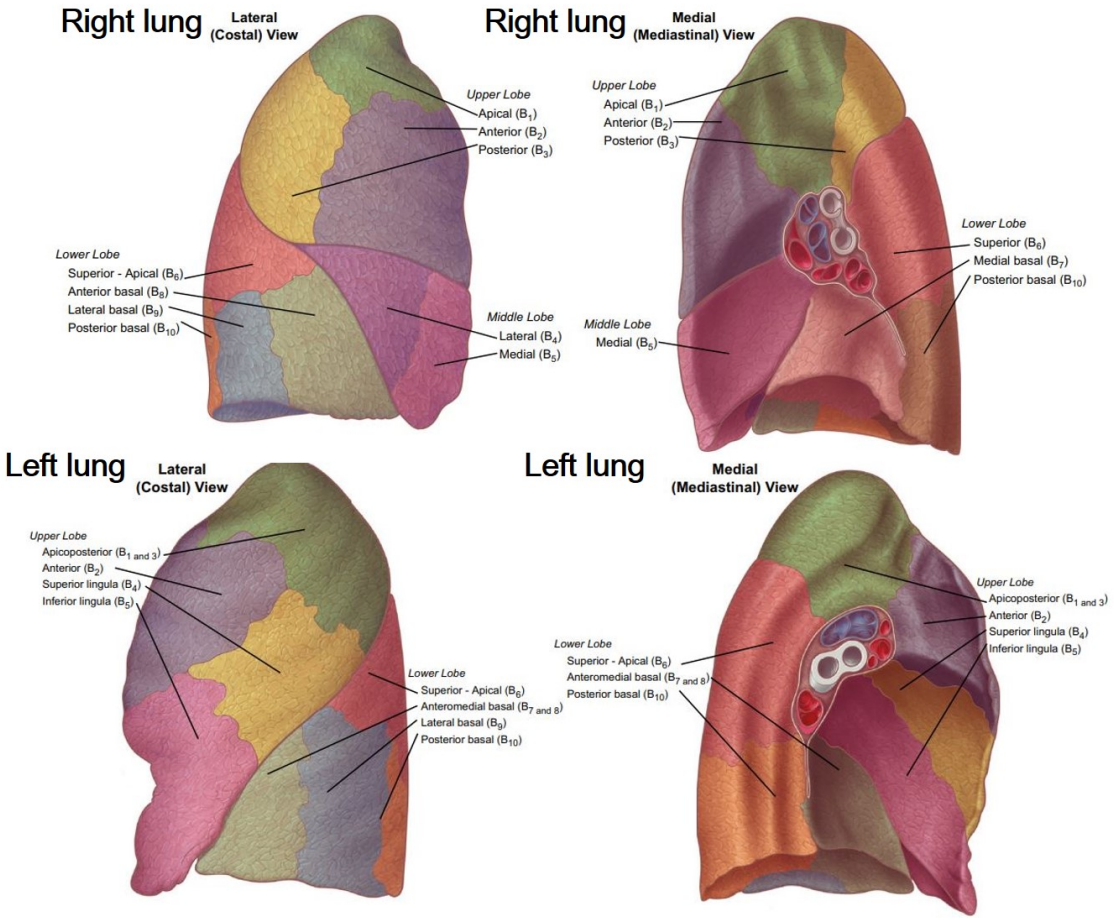

Figure 2: The topographic anatomy of the bronchopulmonary segments for both left and right lung. Reproduced with the permission of Ref [52], copyright © 2007 Elsevier.

2.1.2 The auto-segmentation methods of the pulmonary segments

Despite the extensive clinical benefits related to the segmentation of pulmonary segments, its practical application is limited by the time-intensive process of delineating segment boundaries within three-dimensional computed tomography (3DCT) images. Typically, no distinct physical boundaries separate these segments. The complexity of segmenting these segments further compounds this issue. Van Rikxoort et al. [58] developed a fully automatic method that subdivides each lobe into segments using voxel classification. This approach considers voxel features based on their relative positions within the lobe and their spatial relationship to detected lobar fissures, and had 77% accuracy in identifying tumor locations, albeit without validating the segment boundaries. Kuang et al. [59] developed the ImPulSe deep-learning model for the segmentation of pulmonary segments, which had an overall segmentation dice similarity coefficient (DSC) of 0.846. However, in certain cases, the existing models used for the segmentation of pulmonary segments may not be suitable. For example, the upper part of the left upper lobe can be divided into three segments (apical, anterior and posterior) rather than the common two segments (apico-posterior and anterior) [60, 61]. In other instances, it may be necessary to further divide a segment into two to three sub-segments to achieve a more precise analysis. In these situations, the standard models for segment segmentation may not adequately capture the anatomical variability or provide the level of detail required. Consequently, manual revision on a slice-by-slice basis may be necessary.

Some anatomical-based methods have been developed to address the limitations of existing models [53–55]. These methods take into account the specific anatomical characteristics of the lung, such as the distribution of the bronchial tree (BT) or

pulmonary arteries (PAs). Kuhnigk et al. [53] proposed a BT-based method to extract pulmonary segments from 3DCT data. After lobe segmentation, the method approximated lung segments by assigning each lung voxel to the nearest point of the segmented BT within the same lobe. Validation studies reported an accuracy DSC of 0.8 on two in-vitro left lungs. Stoecker et al. [54] introduced a PA-based segment segmentation approach, achieving a mean surface distance (MSD) of 2–3 mm compared to the ground truth. However, the manual generation of PAs in Stoecker et al.'s study took 4–6 hours, which poses a barrier to the widespread adoption of this method in clinical settings.

2.2 The methods of generating ventilation images from CT image

Since the surrogate of lung ventilation maps generated using CT images emerged, CT-based ventilation research has rapidly developed. As many lung cancer patients undergo 4DCT simulation as part of the standard treatment planning process, generating CT-ventilation images provides functional information without burdening the patient with an extra imaging procedure. There are three main methods for generating ventilation images from CT, (A) DIR-based method, (B) feature-based method, and (C) Deep learning-based method.

2.2.1 DIR-based method

For DIR-based methods, the peak-inhale phase CT (CT_{in}) and peak-exhale phase CT (CT_{ex}) are selected from 4DCT data to represent the largest regional volume differences and changes in HU values. The rationale underlying density change-based methods is that each lung CT voxel represents a combination of water-like and air-

like tissues [62], so the density of the lung voxel in the CT_{in} decreases when air is inhaled. The density change in each voxel then can be calculated by applying DIR to map the voxels between CT images of inhalation and exhalation. The Jacobian-based methods use the volume change in a given lung voxel due to inhaled air. The volume change can be calculated as the Jacobian of the generated DIR [63].

The two main conventional DIR-based methods are HU-based and Jacobian-based. Both methods require DIR between the CT_{in} and CT_{ex}. In the HU-based method, a voxel at spatial position p of the CT_{ex} is mapped toward a voxel at spatial position p' of the CT_{in} by DIR. The ventilation value at position p can be directly calculated using Equation (1) [34].

$$Vent(p) = \frac{-1000 \times (HU_{ex}(p) - HU_{in}(p'))}{HU_{ex}(p) \times (HU_{in}(p') + 1000)} \tag{1}$$

In $CTVI_{Jac}$, the volume change of a voxel at position p is calculated using the determinant of the Jacobian of the deformation field at position p. This process is performed using Equation (2).

$$Vent(p) = \begin{vmatrix} 1 + \frac{\partial u_x(p)}{\partial x} & \frac{\partial u_x(p)}{\partial y} & \frac{\partial u_x(p)}{\partial z} \\ \frac{\partial u_y(p)}{\partial x} & 1 + \frac{\partial u_y(p)}{\partial y} & \frac{\partial u_y(p)}{\partial z} \\ \frac{\partial u_z(p)}{\partial x} & \frac{\partial u_z(p)}{\partial y} & 1 + \frac{\partial u_z(p)}{\partial z} \end{vmatrix} - 1 \tag{2}$$

However, these methods are calculated at the voxel level, and the image artifacts and the DIR accuracy will seriously affect their results. To improve the robustness of the CTVI, alternative methods focusing on sub-regional analysis have been developed [41, 42, 64–66]. To reduce the uncertainty caused by the DIR, sub-regional

based methods were implemented to calculate the volume/density changes as Figure (3) shown. For instance, Castillo et al. introduced the Integrated Jacobian Formulation (IJF) and Mass Conserving Volume Change (MCVC) numerical methods, which represent two distinct classes of ventilation methods: transformation-based and intensity-based (HU-based) methods, respectively [65, 66]. The IJF and MCVC methods utilize sub-regional volume change measurements that satisfy a certain uncertainty tolerance.

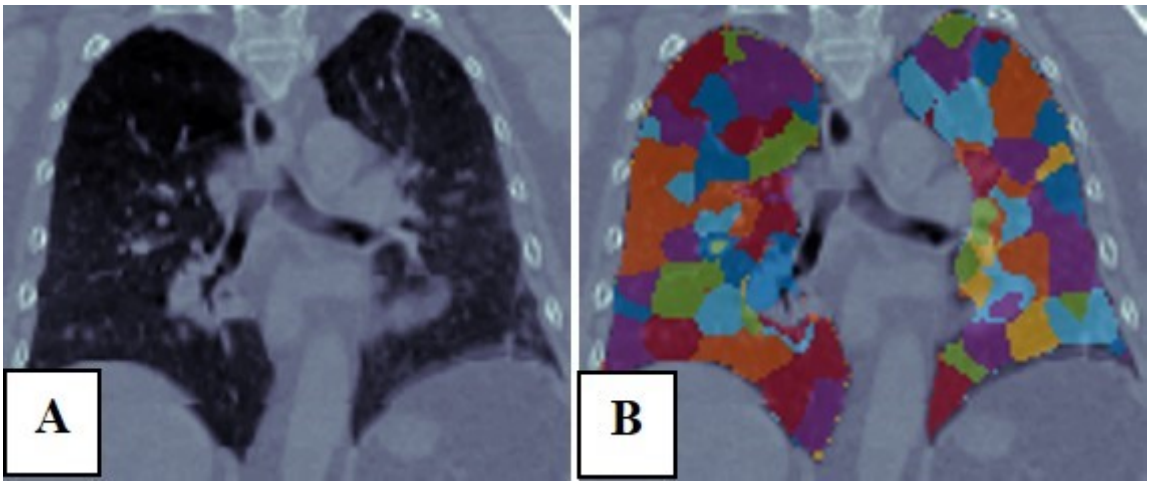

Figure 3: The result of the sub-volume clustering from the CT image. Figure (A) shows the CT image. Figure (B) shows the sub-volume segmentation results in the lung region.

Similarly, Szmul et al. applied the super-voxel concept to the CTVI generation [41]. The super-voxel segmentation was performed with the Simple Linear Iterative Clustering (SLIC) algorithm [67]. These methods rely on sub-regional estimates of volume change that possess quantitatively characterized and controllable levels of uncertainty. Consequently, they exhibit robustness against minor variations in DIR methods, thereby enhancing the overall reproducibility of the resulting ventilation images. However, it is important to note that these methods still rely on DIR and are thus subject to its inherent limitations. DIR accuracy can be compromised by 4DCT image artifacts and the specific parameters employed, thus limiting the overall accuracy of the obtained results.

2.2.2 feature-based method

There have been other methods proposed in the literature without using DIR. For example, Kipritidis et al. devised a modified HU-based method [43] that generates robust ventilation images without DIR. The generation of the CTVI was based on the following Equations (3) and (4).

$$Vent_{\overline{HU}}(p) = \sum_{\phi=1}^{N} V_{\phi}(p)/N \tag{3}$$

$$V_\phi(p) = \begin{cases} f_\phi^{Air}(p) \times f_\phi^{Tissue}(p), & p \in L(\phi) \\ 0, & p \notin L(\phi) \end{cases}$$
$$= \begin{cases} \dfrac{HU_\phi(p)}{-1000} \times \dfrac{HU_\phi(p)+1000}{1000}, & p \in L(\phi) \\ 0, & p \notin L(\phi) \end{cases} \tag{4}$$

Here, $HU_\phi(p)$ is the HU value at voxel location (p) and 4DCT phase bin ϕ=1,. . . ,N. The terms for HU values in the range $[-1000, 0]$ represent each voxel's air and tissue fraction, respectively.

$$f_\phi^{Air}(p) = \frac{HU_\phi(p)}{-1000} \tag{5}$$

$$f_\phi^{Tissue}(p) = 1 - f_\phi^{Air}(p) = \frac{HU_\phi(p)+1000}{1000} \tag{6}$$

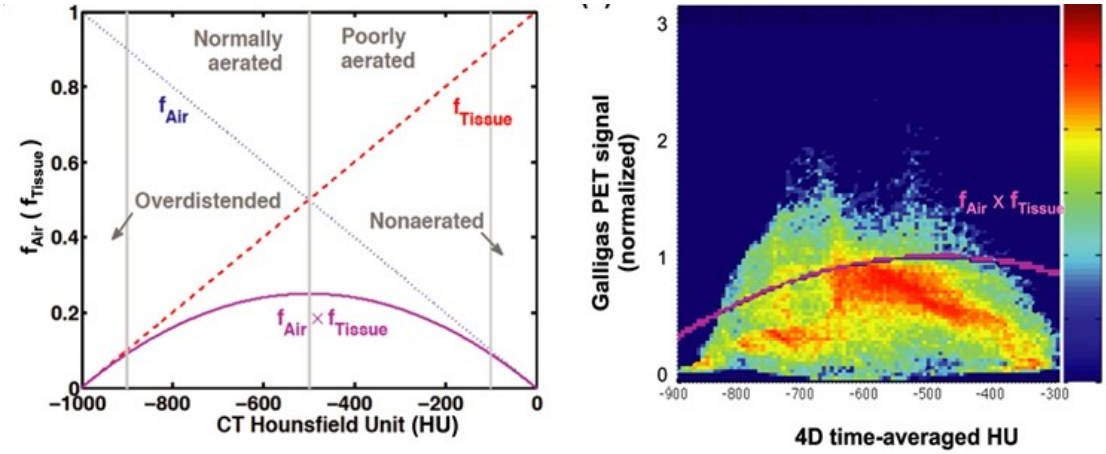

Figure 4: Figure (A) is the comparison of the air and tissue fractions $f_\phi^{Air}(p)$ and $f_\phi^{Tissue}(p)$ at each voxel location p as a function of HU values in the 4DCT phase ϕ. The solid curve shows the model for regional aeration, $V_\phi(p) = f_\phi^{Air}(p) \times f_\phi^{Tissue}(p)$. Figure (B) is an example density plot comparing normalized Galligas PET and 4D-averaged HU values for corresponding lung voxels in a single scan. Reproduced with the permission of Ref [43], copyright © 2016 American Association of Physicists in Medicine.

The justification of this method is based on the understanding that physiological ventilation, which involves blood-gas exchange, operates through diffusion. By utilizing the HU values at each voxel location to represent fractional air/tissue content, we can create a straightforward HU-based model for physiological ventilation. This model computes the voxel-wise product of air and tissue densities, serving as an estimate for the rate of blood-gas exchange in that voxel. Figure 4 (A) shows the ventilation model, $V_\phi(p)$ as a function of HU values in the range $[-1000, 0]$, and Figure 4 (B) shows the comparison between $V_\phi(p)$ and the actual normalized ventilation value of one patient.

The regional product of f^{Air} and f^{Tissue} is distinct from the breathing-induced air volume changes estimated by DIR-based methods, which can be interpreted as reflecting the "dynamic" or breathing-induced ventilation averaged over many breaths. An advantage of this approach was the ability to minimize the impact of phase-specific 4DCT image artifacts by averaging the air–tissue product over multiple phase bins for the each voxel. However, it's worth noting that this method may tend to overestimate areas with edges between solid tissue and normal parenchyma, such as the peritumoral lung and the pleural space. Instead of using the 10 phases of the 4DCT, Yuan et al. [68] utilized the average CT to generate the ventilation image, obtaining similar results as Kipritidis's method [43].

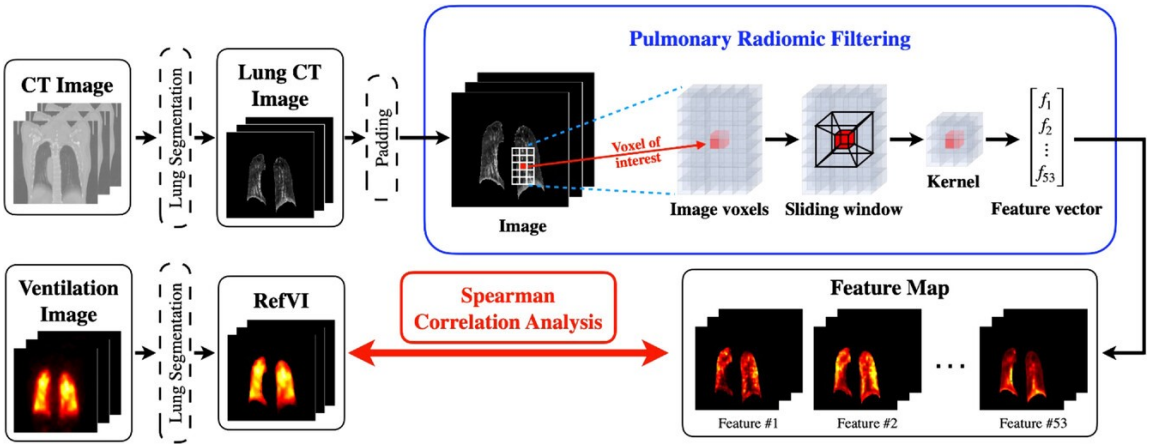

Figure 5: The workflow of the radiomic-based method. Reproduced with the permission of Ref [69], copyright © 2022 American Association of Physicists in Medicine.

Another method is the radiomics-based method. In Lafata's study [70], thirty-nine radiomic features were extracted from the lungs of 64 patients to explore their potential as imaging biomarkers for pulmonary function. These features collectively captured the lung's morphology, intensity variations, fine-texture, and coarse-texture of the pulmonary tissue. Comparing the extracted lung radiomics data to conventional pulmonary function tests, they found that patients with larger lungs of homogeneous, low attenuating pulmonary tissue (as measured via radiomics) were associated with poor spirometry performance and a lower diffusing capacity for carbon monoxide.

In a different study by Yang, radiomic feature maps such as Gray-level run length matrix (GLRLM)-based Run-Length Non-Uniformity and Gray-level co-occurrence matrix (GLCOM)-based Sum Average were used to generate the ventilation image [69]. Figure 5 illustrates the workflow of the radiomic feature-based method, where the feature maps are extracted from the lung CT image and then reconstructed to the CTVI after radiomic filtering. The achieved p ($median\,[range]$) for the two features were 0.46 $[0.05, 0.67]$ and 0.45 $[0.21, 0.65]$ across 46 patients, respectively. Huang et al. employed a sparse-to-fine radiomics framework, identifying eight function-correlated features to generate a ventilation image that exhibited moderate-to-strong voxel-wise correlations with the reference [71].

2.2.3 Deep learning-based method

With the rapid development of deep learning, it has been successfully applied to generate functional images from CT scans, showing high correlation with SPECT/PET images [44–47]. Deep learning-based approaches can be broadly categorized into two main methods. The first method involves using a deep learning model to learn

the volume or density changes of corresponding voxels between two phases of CT images to generate the functional image. In the studies of Zhong and Liu [46, 47], the input data consist of CT_{in} and CT_{ex} images. Both models demonstrated a high correlation between the predicted images and the RefVI, where RefVI represents the SPECT/PET images considered as the ground truth. The second method hypothesizes that texture features of the local region can reflect the function, similar to the radiomics feature-based method. Ren's studies [44, 45] employed input data containing a single CT image acquired at the same posture as the SPECT image. These methods are based on the fact that the HU value is influenced by the air/tissue ratio, which in turn determines the attenuation coefficient in a specific location. In the lung parenchyma, the fractional air/tissue can act as a surrogate for the blood-gas exchange rate. Consequently, pulmonary diseases involving abnormal blood-gas exchange often exhibit textural alterations in the lung parenchyma.

While deep learning methods have shown promising results, they do have certain limitations. One such limitation is their requirement for a large amount of training data. Data from other sources may not generalize well and could lack interpretability. Additionally, the complexity of deep learning models can make it challenging to understand the reasoning behind their predictions.

2.3 The application of functional images to treatment plan design

2.3.1 Parameters in functional image-guided radiotherapy

In traditional lung cancer RT, the MLD, $V20$, and $V5$ (Vx means the relative volume of the lung received at least x Gy) are commonly used parameters to predict the occurrence of RP. However, with the emergence of FLART, functional images such as

perfusion and ventilation have been incorporated into the radiotherapy of lung cancer to identify more powerful biomarkers for accurately predicting radiation-induced lung injuries (RILI), including RP, radiation fibrosis (RF), and the global pulmonary function [15, 19–22, 72–75]. Consequently, combining the functional images has led to the proposal of new parameters like fVx, $fMLD$, sVx, and $sMLD$. These parameters offer improved predictive capability for incidents of RILI compared to traditional parameters, enabling a more precise and personalized approach to lung cancer radiation therapy. The definition of fVx is expressed as Equation (7).

$$fVx = \frac{\sum_{i \in R_x} f_i}{\sum_{i \in R} f_i} \tag{7}$$

Let R represents the set of voxels in the entire lung, R_x denote the set of the voxels in the entire lung that receive at least x Gy dose, f_i is the functional value of the voxel $i \in R$. The $fMLD$ can be represented as Equation (8), where D_i is the dose of the voxel $i \in R$.

$$fMLD = \frac{\sum_{i \in R} f_i \times D_i}{\sum_{i \in R} f_i} \tag{8}$$

sVx and $sMLD$ can be calculated as Equations (9) and (10).

$$sVx = \frac{\sum_{i \in R_x \cap R_f} v_i}{\sum_{i \in R_f} v_i} \tag{9}$$

$$sMLD = \frac{\sum_{i \in R_f} v_i \times D_i}{\sum_{i \in R_f} v_i} \tag{10}$$

v_i is the volume of the voxel $i \in R$, R_f is the set of voxels with a higher functional value than f in the entire lung. The f can be interpreted as the threshold value that used to separate the whole lung into the FHV and low functional volume (LFV) and

the R_f represents the HFV. Figure (6) shows the functional weight value of each voxel used to calculate the traditional and functional weighted parameters.

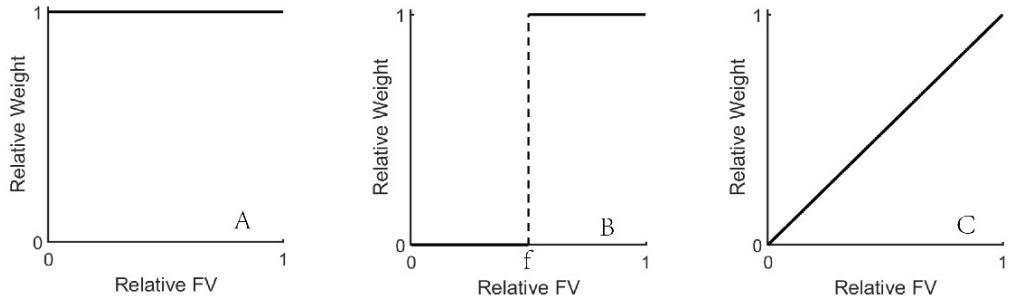

Figure 6: Represents the functional weight value strategy used for calculating the traditional and the functional weighted parameters. FV means the functional value scale to 0-1. Figure (A). means the functional weight value of all the voxels inside the lung is the same. All of them are equal to 1. Figure (B). shows the lung is separated into two parts based on the threshold value f. Only the voxel with high functional value can contribute to the calculation for $sDVH$ and $sMLD$. Figure (C). represents that each voxel's weighted value equals the relative FV for the $fDVH$ and $fMLD$ calculation.

2.3.2 The methods of functional image-guided treatment plan design

Functional images have shown potential not only in predicting RILI, but also in treatment plan optimization for lung cancer radiotherapy. The use of perfusion images for treatment planning optimization was first proposed by Marks in 1992 [76], where beam angle selection was optimized to reduce the dose to high functional regions. Subsequently, Seppenwoolde et al. in 2002 [23] directly utilized lung perfusion images for plan optimization, leading to reductions in $fV20$ and $fMLD$. They observed that patients with large defect regions could benefit the most from applying the perfusion image. However, this method required using the functional image of the whole lung as input into the optimization process, which was not supported by the current commercial clinical TPS. Researchers had to develop their planning optimization modules to implement this approach, which could hinder its widespread clinical application.

To address this limitation, Christian et al. proposed an alternative method in 2005 [24]. They defined a HFV with an individual threshold value for each patient and used the HFV for optimization to reduce $sV20$ instead of considering the weight of each voxel in the lung. This HFV-based approach could be implemented in the TPS. Following this, many studies [25–30, 77–90] employed various threshold values to divide the lung into HFV and LFV and subsequently reduced the dose to the HFV.

One disadvantage of the HFV-based approach is the lack of a standardized threshold value, which can introduce variability in the optimization process. Researchers have attempted to compare the voxel-based method with the HFV-based method. For instance, Iqbal et al. [31] conducted a study comparing both methods for treat-

ment planning in 19 patients and concluded that the voxel-based method outperformed the HFV-based method. However, the results may be influenced by various factors, including target size, location of the functional/defect region, and the relationship between the tumor and the defect regions.

In summary, functional images have demonstrated potential in improving treatment planning optimization by considering high functional regions and reducing radiation doses to these regions. However, challenges such as the lack of standardized threshold values and compatibility with commercial TPS need to be addressed to facilitate their broader clinical application. Ongoing research and advancements in technology will likely further enhance the integration of functional images into the optimization process for lung cancer radiotherapy.

2.3.3 The impact of the treatment techniques

The current treatment techniques include three-dimensional conformal radiotherapy (3DCRT), intensity modulated radiation therapy (IMRT), volumetric modulated arc therapy (VMAT), and intensity modulated proton therapy (IMPT). The treatment modality could also affect the plan's effectiveness. For the comparison between the IMRT and VMAT, Mounessi et al. [91] and Yamamoto et al. [80] concluded that IMRT and VMAT could achieve comparable results. Compared to the photon beam, the proton beam has the physical properties of Bragg peak, which has no dose in the distal area. As for the patients, the defect regions usually won't show simultaneously at the entrance and the distal area in the beam direction. For the proton beam selection, as long as the entrance of the beam is located at the defect region, the region behind the tumor can be well protected in the IMPT plan compared to the

photon beam plan [82, 92, 93].

2.3.4 Functional images for adaptive radiotherapy

Studies found that the function of the lung could vary during the treatment [48–50, 94]. Yuan et al. [48] and Meng et al. [49] published their observations that some patients with centrally located tumors might have temporary defect regions caused by tumor compression. These regions could re-function after the tumor shrank during the treatment. They suggested that reacquiring the patient's functional image during the treatment can help to alter the treatment planning to achieve better effectiveness. Their studies indicated insufficient functional planning based on the functional image acquired prior to treatment. Yamamoto et al. [51] acquired 2 CT scans at 2 time points (16-20 Gy and 30-34 Gy) during the treatment for adaptive planning. The results showed that functional planning significantly reduced the functional mean lung dose by 5.0% compared to anatomic planning in the adapted scenario. The adaptive re-planning due to the variety in lung function could help patients to preserve more function after the treatment. However, the time points for rescanning functional images need to be investigated in the future to avoid unnecessary dose and monetary costs. Even with the adaptive re-planning strategy, the recoverable regions would receive high dose before they regain the function since these regions were considered as low functional region during the initial treatment planning. For better protection of the recoverable regions, these regions need to be identified before the treatment to reduce the dose.

2.3.5 The clinical trials of functional image-guided radiotherapy

Several clinical trials have successfully integrated functional images into treatment planning for patient treatment, leading to promising results [17, 89, 95–97]. For example, Vinogradskiy et al. conducted a multi-institutional phase 2 clinical trial based on the functional image of the CTVI [17]. The trial demonstrated that the rate of RP 2+ was 14.9%, meeting the expected phase 2 criteria, which was lower than the threshold of 16.4%. In another clinical trial reported by Yamamoto [97], a single-arm prospective study was conducted using the CTVI ventilation image for FLART. In this clinical trial, 24 patients received conventionally fractionated radiation therapy (CFRT), while 9 patients underwent stereotactic body radiation therapy (SBRT). The results showed that for CFRT, the rate of RP 3+ was 4.2%, while none of the patients in the SBRT group experienced RP 3+. These clinical trials provide valuable evidence supporting the integration of functional images into treatment planning for lung cancer patients. The use of functional imaging allows for better understanding and consideration of the individual patient's lung function, leading to more personalized and optimized radiation treatment plans. As technology and research continue to advance, functional images are expected to play an increasingly important role in improving treatment outcomes and reducing the risk of RILI in lung cancer patients.

3 Atlas-based auto-segmentation of the pulmonary segments

3.1 Introduction

The primary function of the airway in the lung is to facilitate the transportation of air, making it a crucial component with a significant impact on the corresponding downstream lung parenchyma area. The pulmonary segments have been recognized as the functional anatomic unit of the lung, with each segment possessing its bronchus, pulmonary arterial, venous, and lymphatic systems [52]. Yuan's study [48] provides evidence that the function of some pulmonary segments in the lung can recover after RT, particularly as tumors shrink, and the associated airway branches become ventilated again. Building upon these findings, we developed a hypothesis that suggests tumors may obstruct the "upstream" airway, leading to the loss of function in the "downstream" parenchyma (corresponding to the pulmonary segments). However, as the tumor diminishes or disappears following treatment, the previously blocked airway reventilates, allowing the corresponding pulmonary segments to regain its ventilation capacity.

To explore the above-mentioned hypothesis, our study involved segmenting the patient's lung into eighteen pulmonary segments, which represent the smallest anatomical functional regions within the lung. Subsequently, we examined whether the tumor blocking any segments and compared the blocked segments with the low functional regions identified from SPECT/PET functional images. Since no distinct physical boundaries separate these segments, the current anatomical-based methods for auto-segmenting the pulmonary segments rely on the segmentation of the airway or vessel of the lung. However, for the patients with tumor blocking the airway or vessels,

the segmentation of the airway or vessel would be insufficient due to the exist of the tumor which could compromise the pulmonary segments segmentation [55]. The deep-learning method usually lacks of robust when deal with data different from the training data [98]. The performance of the deep-learning method on patients with tumor blockage may need to be further evaluated. To achieve the segmentation of the pulmonary segments accurately, we employed an Atlas-based method to contour the segments on the patient's CT image. This approach leverages an atlas of predefined segmentations to guide the segmentation process, ensuring consistent and reliable results.

3.2 Methods and Materials

3.2.1 Scheme overview of Atlas-based auto-segmentation of the pulmonary segments

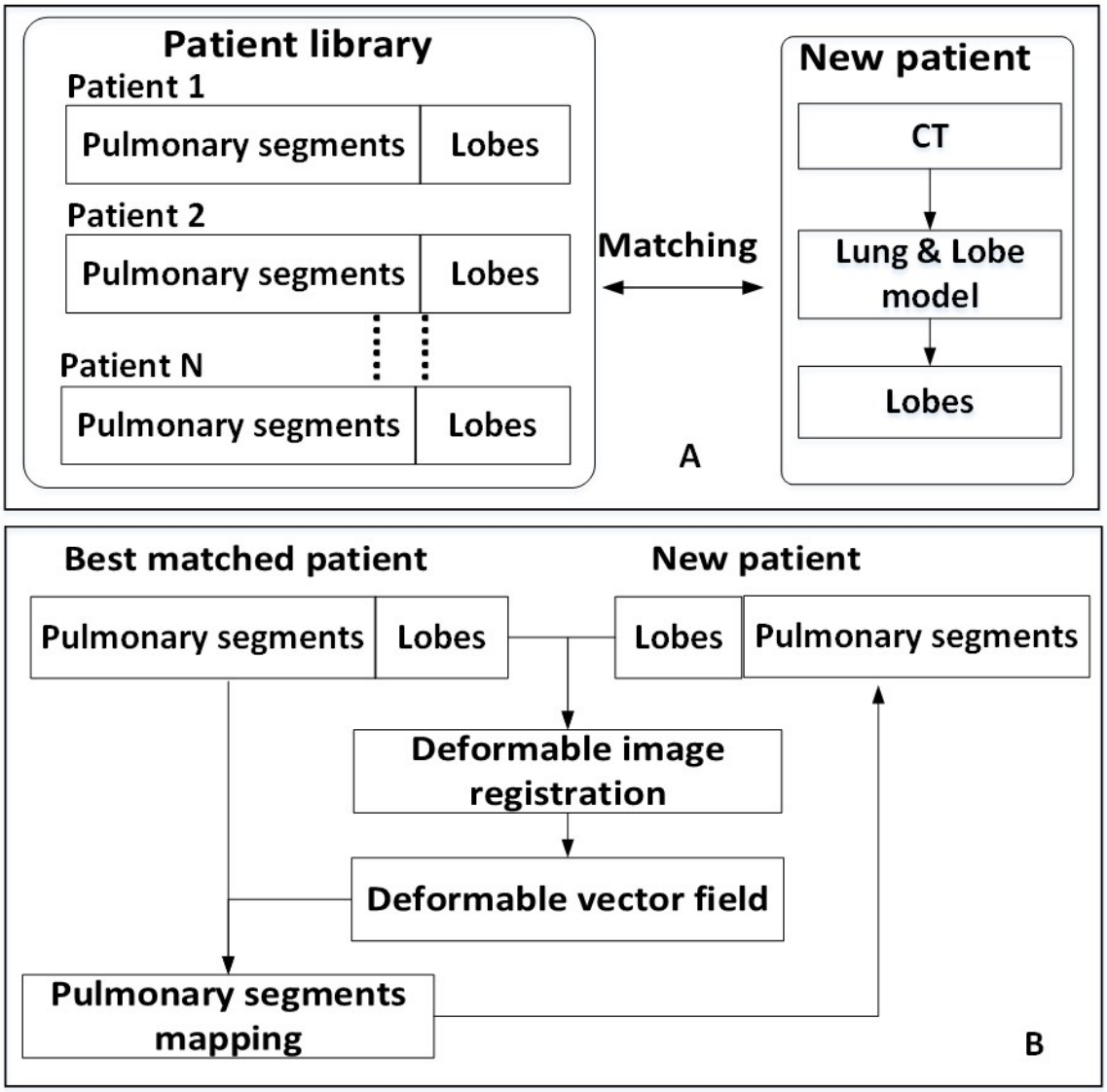

Figure 7: The workflow of the atlas-based auto-segmentation of the pulmonary segment. A is the reference patient search. Firstly, a bronchial tree-based method is used to perform the pulmonary segments' segmentation for N patients to build the library. Then, for a new patient, the lung and lobe segmentations are performed. The lobe mask of the new patient is compared to the lobe mask of the patients in the library to select the most similar patient as the reference patient. B is the atlas-based segmentation scheme. After the selection of the reference patient, a deformable registration is conducted between the lobe mask of the new patient and the reference patient to obtain a deformable vector field. The deformable vector field was then applied to deform the pulmonary segment mask of the reference patient to the new patient.

The proposed bronchopulmonary segments segmentation method on the 4DCT images contains two parts, as illustrated in Figure (7). The first part is a modified bronchial tree-based method [99] for pulmonary segments segmentation for libraries building as Figure (8). This method was performed on 150 breath-hold high resolution CT (HRCT) images to build two patient libraries (left lung and right lung). The second part is an Atlas-based method for segment segmentation on 4DCT images. Fourteen manual segmentation of the pulmonary segments were used to verify the accuracy of the Atlas-based method. Ultimately, the Atlas-based method was applied to generate the bronchopulmonary segments segmentation on input 4DCT images with tumor blocking the main airways connected to the segments. These patients' low functional regions acquired from the ventilation images were compared with the identified blocked segments to determine our hypothesis that the areas blocked should present with low function. These steps are elaborated in the following sections.

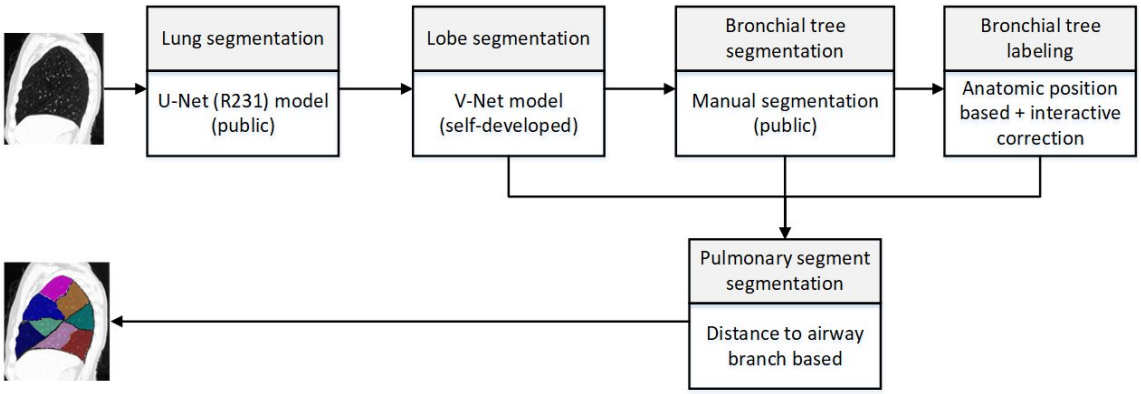

Figure 8: The workflow of generating the bronchopulmonary segments with a bronchial tree-based method.

Table 1: The information on the patients used in this study includes the sources, disease type, image types, labels, numbers, and the corresponding tasks.

Source	Disease	Image type and label	Number	Task
Randomly selected from the LUNA16 dataset	Pulmonary nodule	Low-dose CT and manually labeled lung lobe masks	51	V-net model building for lobe segmentation
ATM'22 dataset	Various pulmonary disease	Breath-hold HRCT	150	Patient library building for bronchopulmonary segments
VIA/I-ELCAP	Pulmonary nodule	Breath-hold HRCT	14	Assessing the accuracy of the Atlas-based segmentation of the pulmonary segments
TCIA	Lung cancer	Galligas PET and 4DCT	20	Evaluating the match between the low function regions caused by the airway block with the corresponding segments
VAMPIRE challenge	Lung cancer	DTPA-SPECT and 4DCT	21	
	Lung cancer	Galligas 4DPET/CT and 4DCT	25	
Total	–	281	–	

3.2.2 Patient Data

Two hundred and eighty-one patients were included in this study, and all the patient's personal information was removed. Table 1 shows the information of the patients in this study. Among them, fifty-one patients were collected from a publicly available dataset (https://github.com/deep-voxel/automatic_pulmonary_lobe_segmentation_using_deep_learning) to build our V-net model for the lobe segmentation. These patients were randomly chosen from the LUNA16 dataset with manually labeled lung lobe masks, and a detailed description of these cases was presented in [100]. One hundred and fifty patients CT images from Airway Tree Modeling Challenge 2022 (ATM22) were collected to build the patient library as shown in Figure 8[101–105]. Each chest CT image was scanned with a slice thickness between 0.450 mm and 1.000 mm. The axial size of each slice is 512 × 512 pixels with a spatial resolution of 0.500–0.919 mm. Fourteen low-dose documented whole-lung HRCT scans from VIA/I-ELCAP Public Access Research Database (https://veet.via.cornell.edu/cgi-bin/datac/signon.cgi) were used collected and the pulmonary segments were manual segmented by a physician and used to valuate the accuracy of the Atlas-based segmentation of the pulmonary segments. The CT scans were obtained in a single breath hold with a 1.25 mm slice thickness. Therefore, there was no noticeable motion artifact shown on the CT images. Sixty-six patients with ventilation images (SPECT/PET) from two sources were included for the low functional region evaluation with the patients' functional images. The ventilation images (SPECT/PET) will be used as RefVI in the whole thesis. A dataset with 20 patients from The Cancer Imaging Archive (TCIA) public access (https://doi.org/10.7937/3ppx-7s22) [106], for these 20 patients, each patient had a 4DCT scan, two inhale/exhale breath-hold CT scans, a Galligas PET scan and

an attenuation correlation CT scan (missing for CT-PET-VI-07). Since there were no time-averaged 4DCT images in the dataset, the CT_{ex} images were used for the bronchopulmonary segments' segmentation. The second dataset contains 46 patients from the VAMPIRE challenge [34]. Among them, twenty-one lung cancer patients have 4DCT images, time-averaged 4DCT images, DTPA-SPECT ventilation, and corresponding lung masks [107]. For these 21 patients, the time-averaged 4DCT images were used for the bronchopulmonary segments segmentation. The other 25 lung cancer patients from Peter MacCallum Cancer Centre have images with Galligas 4DPET/CT, 4DCT [108–110]. For these 25 patients, the CT_{ex} scans were used for the bronchopulmonary segments segmentation since there were no time-averaged 4DCT images in this dataset.

3.2.3 Lung segmentation and lung lobe segmentation

Due to the diversity of the patient CT images, the modality, and the disease-associated lung pattern, the traditional threshold-based method cannot contour the lung mask accurately [111]. The lung mask segmentation in this study was performed using a well-trained U-net (R231) model (https://github.com/JoHof/lungmask) to segment the lung mask [31] automatically. After segmenting the lung mask, we developed a V-net deep learning model [112] to contour the lung lobe. The details about the model's design and optimization settings was shown in Figure 9. It illustrates the network architecture of the 3D V-Net model used in this study, which was designed based on the original V-Net model. The network consists of a compression path on the left and a decompression path on the right. Each compression path is divided into five stages, each containing one to four convolutional layers. In each

stage, the input dimensions of 112 × 112 × 144 are processed by the convolutional layers, and their outputs are added to the output of the last convolutional layer in that stage. This approach enables the network to learn a residual function. On the right side of the network, four stages operate at different resolutions to facilitate the decompression process. The ultimate output of the model is the segmentation of the five lobes. During training, the model used the Adam optimizer and the dice loss function. The training was performed over 300 epochs, with an initial learning rate of 1e-3, which was reduced to 1e-4 after 150 epochs. The training and validation data were acquired from a public access database [25], which contains 51 CT images randomly chosen from the LUNA16 dataset with manually labeled lung lobe masks. Among them, 41 CT images were randomly selected for training, and 10 were for validation. Three metrics (DSC, robust Hausdorff distance ($HD95$), and MSD) [111] were calculated to evaluate the accuracy of the V-net model on the validation dataset. The DSC measures the overlap between two volumes: A (V-net lobe mask) and B (manual lobe mask). The Hausdorff distance is the maximum distance among the surface distances of all the points in surface A. The surface distance of a point in surface A to surface B means the distance from the point to its closest corresponding point in surface B. The $HD95$ represents the 95^{th} percentile of the surface distances of all the surface points in surface A. The MSD is the average surface distance of all points in surface A.

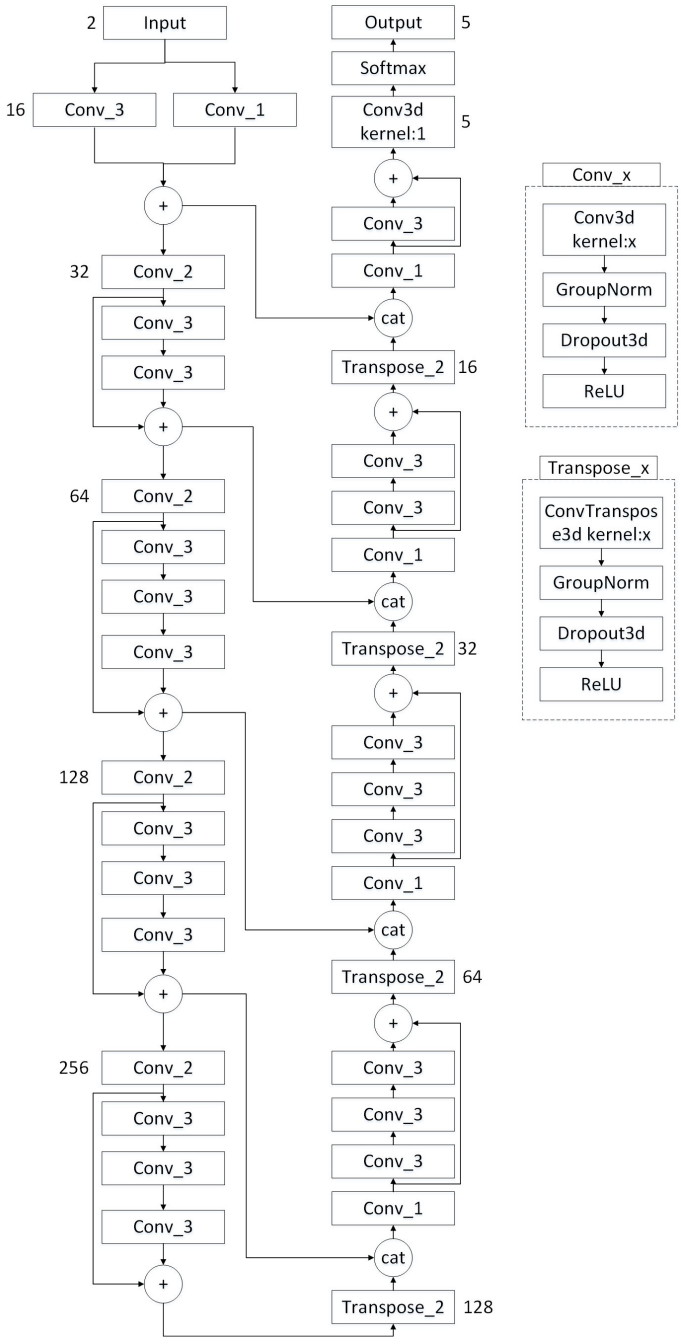

Figure 9: The architecture design of the V-Net model for the segmentation of the lobes.

3.2.4 Atlas-based auto-segmentation of the bronchopulmonary segments on 4DCT images

As Figure 7 (A) shows, for a new patient with a 4DCT image, the trained V-net model will be applied to the 4DCT image to generate the lobe mask. The lobe mask of the new patient will be compared with the lobe mask of every patient in the library to search for the most matched patient as the reference patient. For the lobe mask comparison process between the new patient and the patient in the library, the lobe masks will be aligned based on the center, and the DSC values will be calculated for the mask of the lobes (three for the right lung, two for the left lung). The patient with the maximum average DSC will be selected as the reference. As Figure 7 (B) shows, a deformable registration will be performed between the lobe masks of the new patient and the reference patient to obtain the deformable vector field (DVF). Then the bronchopulmonary segments mask of the reference patient will be deformed to the new patient based on the DVF.

3.2.5 Assessing the accuracy of the Atlas-based pulmonary segments segmentation

Among the 150 patients from ATM22 dataset, seven patients shown insufficient airway segmentation due to the airway blocked by the tumor or diseases other than cancer. Only 143 patients were used to build the patient library. The 14 patients from VIA/I-ELCAP Public Access Research Database with their manual segmentation of the pulmonary segments were used as test dataset to evaluate the accuracy of the Atlas-based segmentation method. Each time one of the patients (patient i) in the test dataset was selected as the new patient, then followed the above-mentioned Atlas-based method to generate the new bronchopulmonary segments for patient i.

The new bronchopulmonary segments were compared with the original ones, and each segment's DSC values were calculated to evaluate the accuracy.

To evaluate if the patient number in the library could affect the accuracy of the Atlas-based method, different number of patients were made up as the library to performed the Atlas-based segmentation. First of all, the order of the patients was randomly shuffled. Then, we selected 10, 20, 30, ..., 130, 143 patients as the patient library to conduct the experiments, respectively.

3.2.6 Evaluation with ventilation functional images

Among the 66 patients, eleven patients showing some bronchial airways blocked by the tumor were selected for this study. These patients were selected based on visual inspection of tumor position and the airway distribution on the CT images. The bronchopulmonary segments of these patients were acquired based on the Atlas-based method. The low functional regions were identified by defining a patient-specific threshold value from Faught's approach [88], calculated as Equation (11).

$$V_T = (\frac{1}{N}) \times (\frac{100 - 15}{100}) \sum_{i=1}^{N} V_{ave,i} (N = 6) \tag{11}$$

The ventilation images were divided into 6 parts as shown in Figure 10. The left and right lungs were divided into 3 equal parts along the z-axis, respectively. $V_{ave,i}$ is the mean ventilation value of part i, V_T is the threshold value. We used the overlap similarity coefficient (OSC) to evaluate the match of the blocked bronchopulmonary

segments with the low functional regions, calculated as Equation (12).

$$OSC = \frac{|A \cap B|}{|B|} \tag{12}$$

Where A is the low functional region in the ventilation image, B is the corresponding blocked bronchopulmonary segments. The reason we used OSC instead of DSC is that the low functional region in the lung may also cause by diseases other than cancer. If these regions exist, the DSC value will underestimate the sensitivity of the calculation for tumor-specific airway blockage.

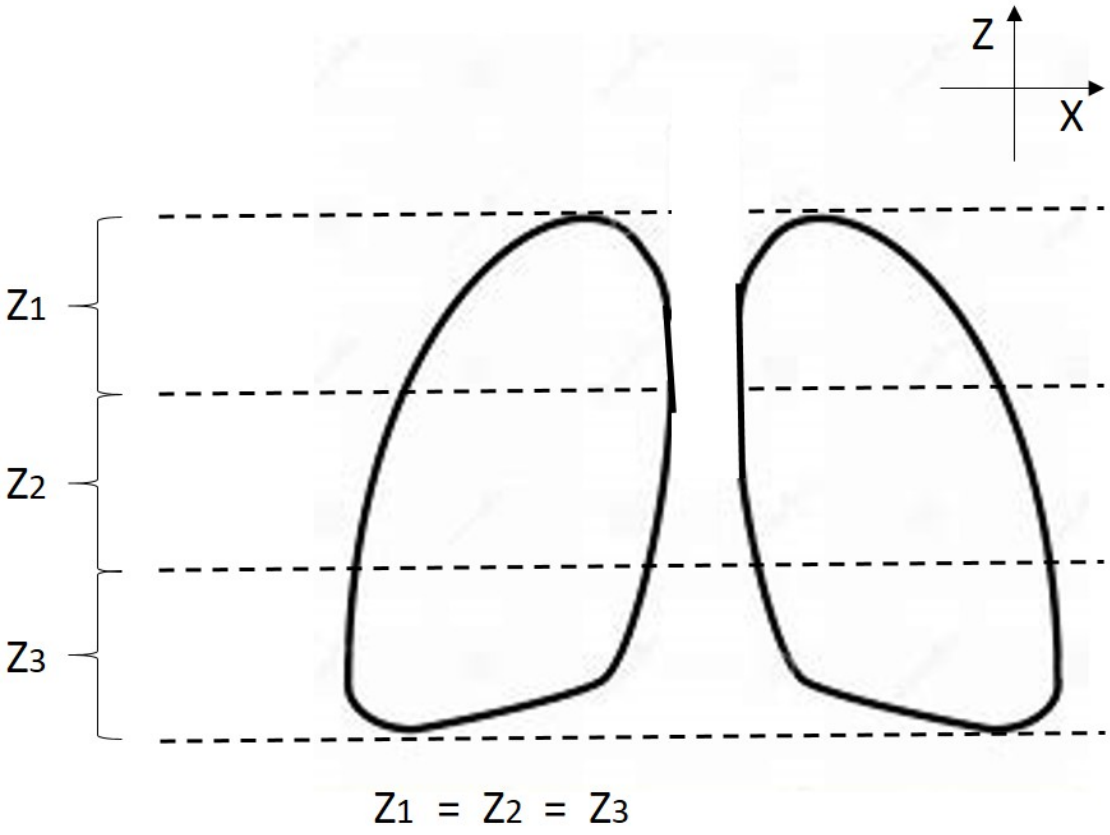

Figure 10: Schematic diagram of lung divided into six parts.

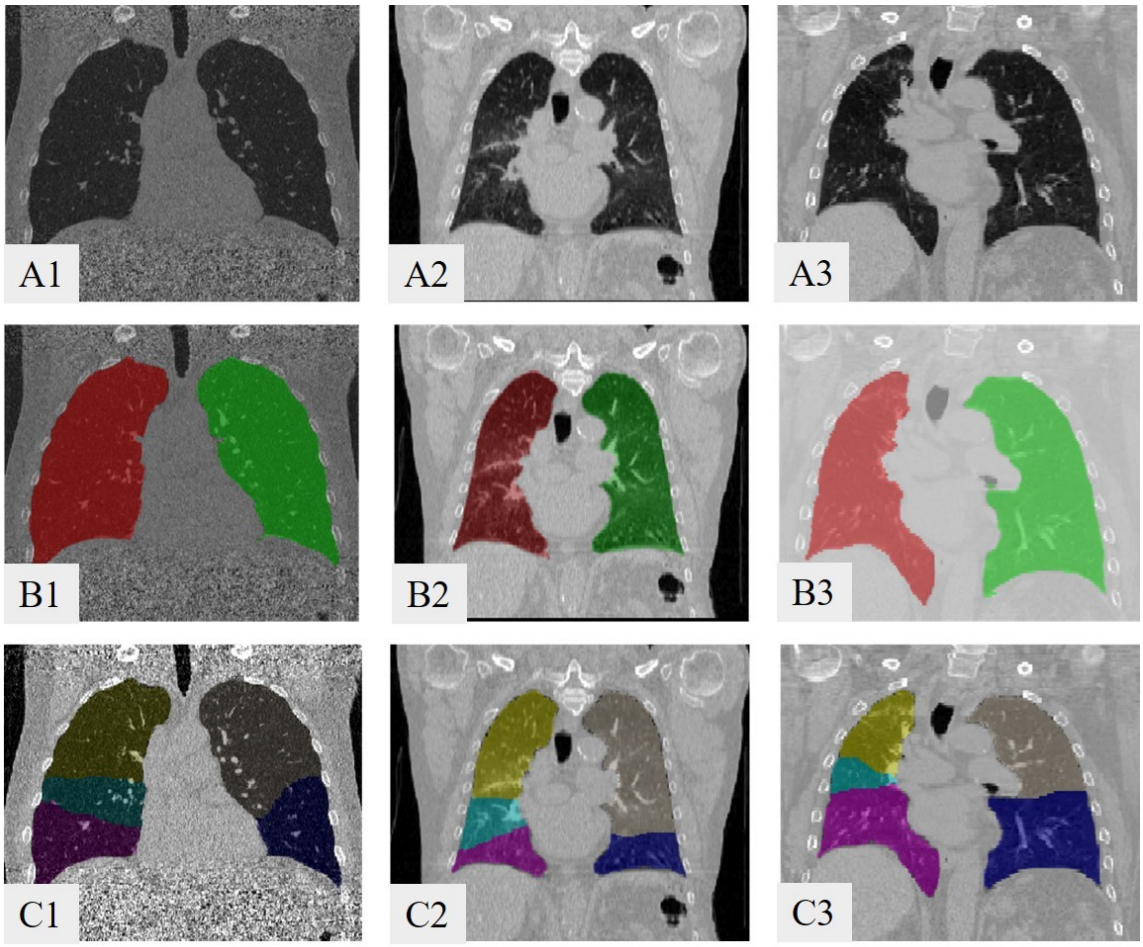

Figure 11: The coronal view of three patients with the CT images (A), lung masks (B), and lobe masks (C). The first column is a patient from ATM'22 dataset, the second column is a patient from the TCIA dataset, and the third column is a patient from the VAMPIRE dataset.

3.3 Results

3.3.1 Lungs and lobes segmentation

In this study, a well-trained lung segmentation model was employed, which had been trained on multiple datasets covering various lung diseases. This model demonstrated high accuracy, achieving a mean DSC value of 0.98 ± 0.03 [111]. Figure 11 (A) and (B) display the coronal view of the CT images and the lung masks generated by the model for three patients.

For the lobe segmentation, the V-net model yielded mean DSC, $HD95$, and MSD scores of 0.94 ± 0.07, 4.59 mm ± 4.65 mm, and 0.93 mm ± 0.90 mm on the validation dataset. For the left lung, the mean DSC value for the lobe segmentation was 0.97, indicating robust segmentation accuracy. However, for the right lung, the mean DSC value was slightly lower at 0.92. Among the right lung lobes, the middle lobe had the lowest DSC of 0.86. The $HD95$ of the right lung's middle lobe and the upper lobe were 6.51 mm and 7.41 mm, respectively, while the other lobes were smaller than 3.01 mm. A similar trend was also shown for the MSD evaluation. The MSD of the middle lobe and the upper lobe of the right lung was 1.18 mm and 1.70 mm, higher than the other lobes, with MSD values smaller than 0.58 mm. The results suggests that right middle lobe's segmentation may be more challenging due to the presence of variations in some patients' images, particularly in identifying the fissure between the right lung's upper lobe and middle lobe. The model was used to generate the lobe masks of the 150 low-dose HRCT images from the ATM'22 dataset, 20 CT_{ex} images from the TCIA dataset, 21 average CT images, and 25 CT_{ex} images from the VAMPIRE dataset. Figure 11 (C) shows examples of the lobe mask

generated by the model for the same patients of lung mask generation.

3.3.2 Assessing the accuracy of the Atlas-based pulmonary segments segmentation

In Figure 12, the Atlas-based method's typical results are presented for one selected right lung and one selected left lung on sagittal slices. Table 2 shows the mean DSC of each bronchopulmonary segment. For the left lung, the mean DSC value for segment segmentation compared to the reference was 0.70 ± 0.11, while this was 0.72 ± 0.11 for the right lung. The superior segment of the lingual part had a DSC value lower than 0.6 in the left upper lobe. In contrast, the portions corresponding to the right lung middle lobe position had a DSC value higher than 0.70. The reason could be that the middle and upper lobes of the right lung are divided by a fissure that the lobe segmentation has been identified. Regarding the lower lobes, the DSC value of superior segments were close to 0.8 for both the left and right lungs. The low-accuracy parts were mainly located at the basal pulmonary segments of the right lower lobe with a DSC value lower than 0.7. Specifically, the right lung's medial, anterior, and posterior pulmonary segments were the regions with relatively lower accuracy. For the left lower lobe, the anterior and posterior pulmonary segments were the regions with relatively lower accuracy.

Figure 13 illustrates the impact of the patient library size on Atlas-based segmentation. Overall, the mean DSC value for both the left and right lungs increased as the number of patients in the library grew. However, it's noteworthy that for certain increments in patient numbers, the mean DSC value exhibited a decrease. This suggests that patients with similar lobe shapes may exhibit varying pulmonary segments distributions within the same lobe.

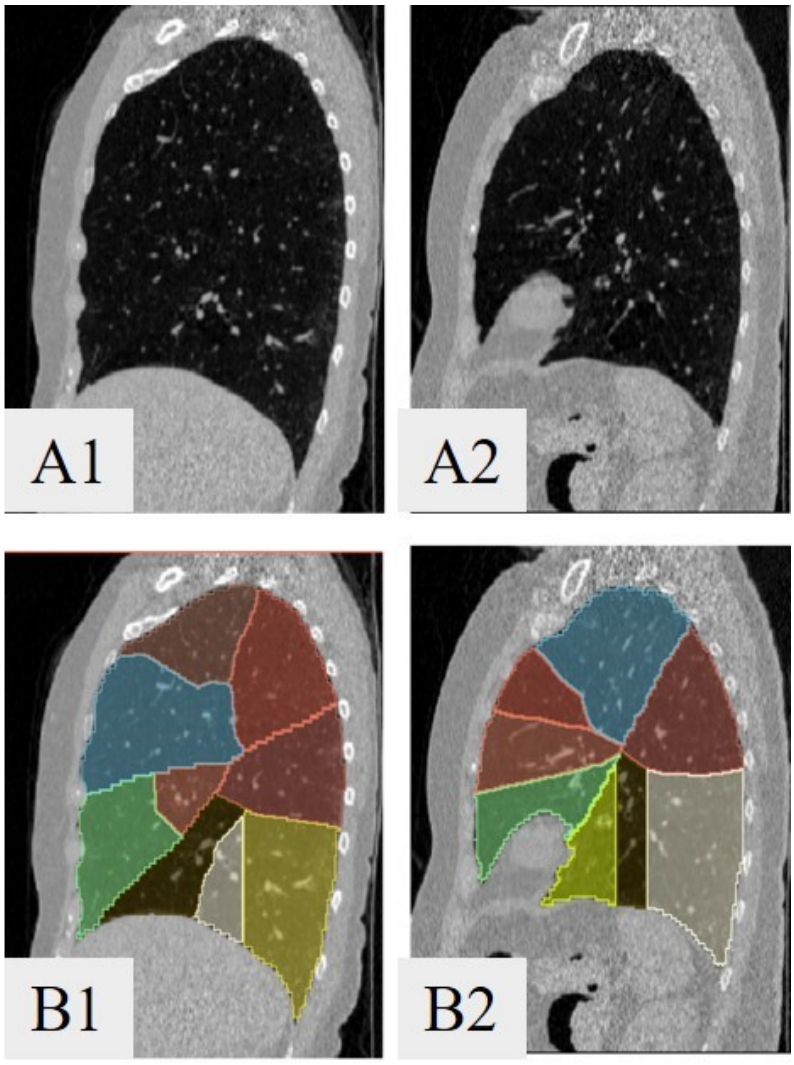

Figure 12: The sagittal view of two patients with the CT images (A), pulmonary segments mask with CT image (B).

Table 2: The result of the Atlas-based pulmonary segments segmentation. The left columns are the result of the left lung, and the right columns are the result of the right lung. The segment columns are the abbreviation of the segment. LUL: left upper lobe, LLL: left lower lobe, RUL: right upper llobe, RML: right middle lobe, RLL: right lower lobe, apic: apicoposterior, ante: anterior, sup: superior, inf: inferior, lat: lateral, post: posterior, med: medial. The code name column means the code name of each segment, L for the left lung, R for the right lung, and the number represents the serial number of the segments. *DSC* columns are the mean DSC values of each segment.

Left Lung			Right Lung		
Code name	Segment	*DSC*	Code name	Segment	*DSC*
L1	LUL_apic	0.78 ± 0.08	R1	RUL_apic	0.79 ± 0.04
L2	LUL_ante	0.71 ± 0.06	R2	RUL_ante	0.74 ± 0.12
L3	LUL_lingual_sup	0.56 ± 0.12	R3	RUL_post	0.80 ± 0.07
L4	LUL_lingual_inf	0.72 ± 0.12	R4	RML_lat	0.72 ± 0.07
L5	LLL_sup	0.77 ± 0.06	R5	RML_med	0.73 ± 0.07
L6	LLL_ante	0.69 ± 0.09	R6	RLL_sup	0.80 ± 0.04
L7	LLL_lat	0.74 ± 0.07	R7	RLL_med	0.68 ± 0.08
L8	LLL_post	0.58 ± 0.09	R8	RLL_ante	0.60 ± 0.11
			R9	RLL_lat	0.72 ± 0.06
			R10	RLL_post	0.60 ± 0.13
Average	–	0.70 ± 0.11	–	–	0.72 ± 0.11

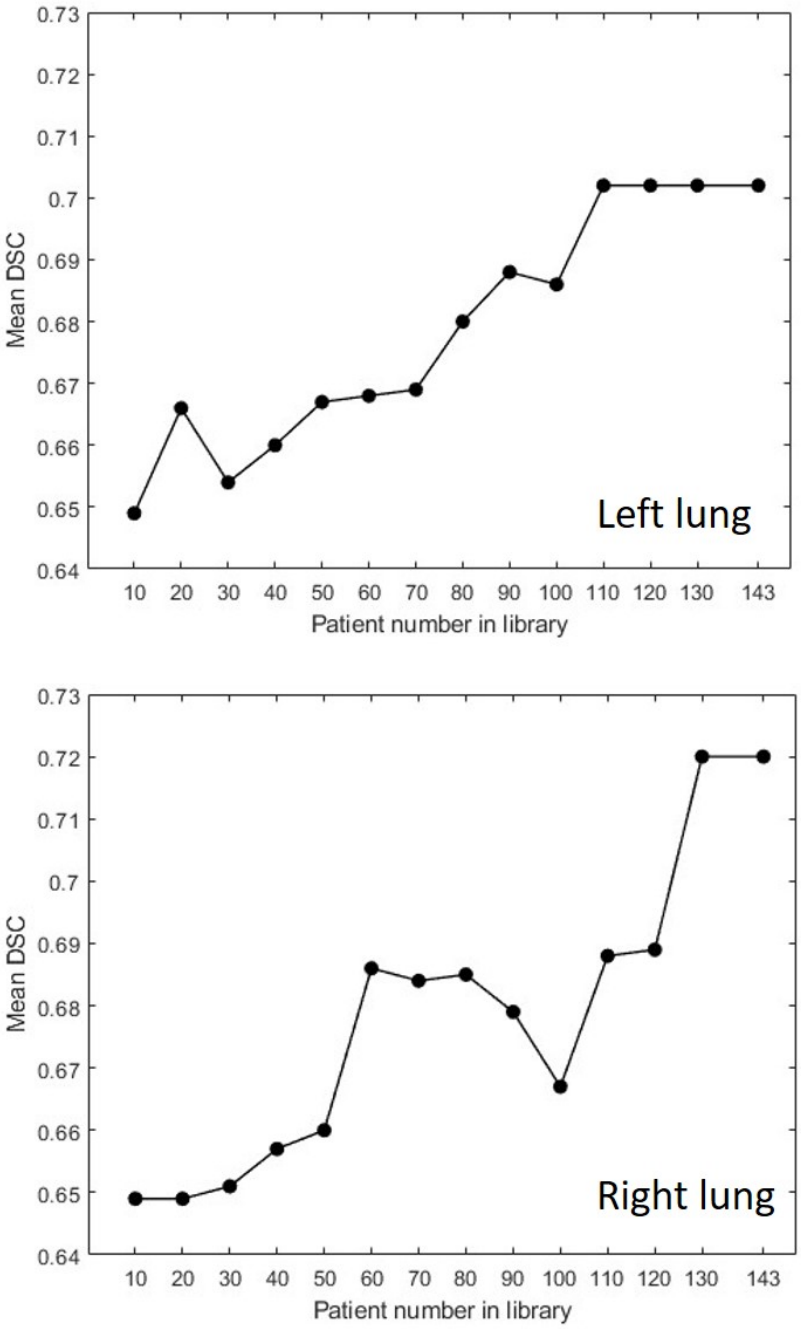

Figure 13: The correlation between the mean DSC value with the number of the patient in the library. The upper figure is for the left lung, the lower figure is for the right lung.

3.3.3 The comparison between the blocked pulmonary segments with the low functional regions

Among the 66 patients, 11 were selected because their tumors were observed to obstruct some airways, resulting in blockage of specific pulmonary segments. Table 3 provides an overview of the blocked pulmonary segments and their corresponding overlap ratio with the low functional regions in these 11 patients. The mean OSC for all 11 patients was found to be 0.90 ± 0.07. Among the selected patients, nine had tumors located in the right lung, while two had tumors in the left lung. For the lower lobe, the tumor tends to block the entire lobe, and in almost all cases, the OSC achieved values above 0.91, indicating a high level of overlap between the blocked segments and low functional regions. Only one case exhibited a slightly lower OSC value of 0.81, suggesting a relatively lower degree of overlap in this specific case. For the upper lobe, the tumor were observed to block 1-3 segments. Figure 14 shows an example of the tumor blockage in the L1 segment, providing a visual representation of the impact of tumor presence on the functional lung regions.

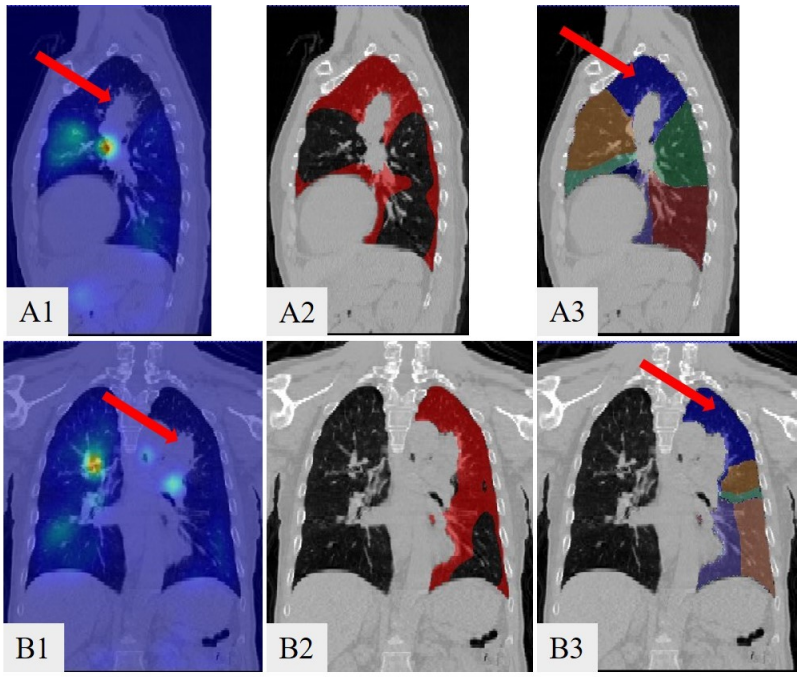

Figure 14: The sagittal and coronal views of an example of the tumor blocked the L1 segment and the comparison between the blocked corresponding bronchopulmonary segments and the low functional region. The red arrows in Figures (A1) and (B1) indicate the tumor's location. Figure (A1) is the sagittal view of the overlap of the CT image with the ventilation image. Figure (A2) shows the sagittal view of the low functional regions (red mask) on the CT image. Figure (A3) shows the sagittal view of the bronchopulmonary segments in the CT image, and the blocked segment is shown in blue. The red arrows in Figures (A3) and (B3) indicate the blocked segment. Figures (B1) – (B3) are the corresponding images in the coronal view.

Table 3: The results of comparing the patients' functional images with the segment segmentations. The blocked regions mean the blocked segments caused by the tumor, R represents the tumor located in the right lung, L means the tumor was located in the left lung. The numbers behind the underline mean the code name of the segment referred to Table 2.

Patient ID	Blocked segments	*OSC*
P1	L_1	0.95
P2	R_123	0.82
P3	R_678910	0.81
P4	R_123	0.88
P5	L_5678	0.91
P6	R_1	0.76
P7	R_123	0.99
P8	R_1	0.93
P9	R_123	0.94
P10	R_678910	0.94
P11	R_678910	0.94
Average	–	0.90 ± 0.07

3.4 Summary and discussion

In this study, an Atlas-based auto-segmentation of pulmonary segments was proposed to identify tumor-blocked regions. For the performance of the Atlas-based auto-segmentation of pulmonary segments, the mean DSC value of the segment segmentation compared to the reference was 0.70 ± 0.11 for the left lung, while this was 0.72 ± 0.11 for the right lung. Our results also showed that the identified blocked segments matched well with the low functional regions in the functional images, with a high mean OSC value of 0.90 ± 0.07, which could support our hypothesis that the blocked segments should be low functional regions. To the best of our knowledge, it is the first time applying the automatic pulmonary segments segmentation for identifying the low functional regions caused by the tumor blockage.

This study showed that the identified blocked segments matched well with the low functional regions in the functional images. However, the segment mask generated based on the Atlas-based method did not show high DSC for every segment. The patients' low functional regions could match well with the segments because the tumor tended to block the whole lobe instead of a single segment among 8 patients, and the accuracy of these patients was dependent on the segmentation of the lobe segmentation. For the patient P3 in Table 3, the OSC value was 0.805, much lower than the other cases. This could be attributed to the fact that the accuracy of the segmentation of the lobe may not be accurate enough in cases where tumors affect the lobe's contouring as in patient P3 with large tumor.

In general, the mean DSC value for both the left and right lungs increased as the number of patients in the library grew. This suggests that with an increasing number of patients, new patients have a higher probability of being matched to a reference

patient with a similar lobe shape. Additionally, the reference patient may exhibit a similar distribution of pulmonary segments within the lobe. However, as Figure 13 demonstrates, the mean DSC value exhibited a decrease for certain increments in patient numbers. The underlying reason could be that while the lobe's shape and the pulmonary segments inside it are correlated to some extent, the lobe's shape alone cannot fully represents the intricate distribution of pulmonary segments. Conversely, pulmonary segments segmentation is highly correlated with the bronchial airway distribution. To enhance the accuracy of Atlas-based segmentation, other novel lobe features should be added to represent the distribution of pulmonary segments within the lobe.

The study's evaluation of tumor obstructive segments was conducted using a relatively small cohort of only 11 patients, which may limit the generalizability and robustness of the findings. Additionally, the study did not account for other pulmonary conditions that the patients might have had, which could significantly influence the outcomes and interpretation of the results. To enhance the reliability, validity, and clinical relevance of the findings, future research should aim to include a larger patient population and incorporate detailed information on comorbid lung diseases. This approach would provide a more comprehensive understanding of how tumor obstructive segments interact with other respiratory pathologies, thereby strengthening the generalizability and statistical significance of the results.

Although the lung segments obstructed by tumors were identified using atlas-based segmentation methods, this approach may lack the precision to detect partial or minor blockages, potentially leading to an inaccurate assessment of ventilation function. To overcome this limitation, future studies could explore topology-based

segmentation methods, which utilize the anatomical distribution of airways and blood vessels to more accurately define lung structures. By analyzing the branching patterns of the bronchial tree and pulmonary vasculature, topology-based methods can improve the detection of subtle obstructions and provide a more reliable evaluation of lung function. This approach not only refines the identification of affected segments but also enhances the understanding of ventilation-perfusion relationships, offering valuable insights for clinical decision-making and treatment strategies.

Despite these limitations, one advantage for our proposed Atlas-based method is that it can be performed on planning CT with thicker slice thickness without the need for complete airway and vessel segmentations for lung cancer patients, which can also be directly used for treatment planning. Furthermore, the sub-segments segmentation can be achieved by using this method if a library with a sub-segments segmentation has been built.

4 Anatomy-wise lung ventilation imaging

4.1 Introduction

The process of lung ventilation involves the flow of air between the atmosphere and the lungs, encompassing air transport through the airway and the exchange of air in the pulmonary alveoli. The pulmonary segments have been recognized as the functional anatomic unit of the lung, with each segment possessing its bronchus, pulmonary arterial, venous, and lymphatic systems [52]. Based on the anatomical information regarding the pulmonary segments and the findings of previous studies [48, 113–115], it is possible that the presence of tumor blockages in a bronchus may correlate with low functional regions in the connected pulmonary segment(s) or sub-segments. Yuan's study [48] highlighted that a tumor-blocked airway can result in the loss of function in connected pulmonary segments. The current CTVI methods could be categorized into DIR-based, texture analysis-based, and Deep learning-based approaches. However, current CTVI methods discussed above have not specifically examined the effects of airway blockage on lung ventilation and its relationship with CTVI. Thus, further research is needed to investigate this aspect and its implications in CTVI analysis.

To effectively apply air transport to ventilation imaging, it is essential to accurately identify the specific areas of the lung that are connected to the corresponding airway branches. For the tumor blocking the airway, the corresponding segments will be considered to have lost the function. For the non-blocked segments, a feature-based analysis method will be applied to analyze their air exchange ability. The super-pixel concept was first proposed and developed as an image segmentation tech-

nology in 2003 [116]. It uses pixel blocks that form specific patterns with adjacent pixels with similar texture, color, and other features. A few super-pixels can represent images, significantly reducing image post-processing complexity. A similar concept, the super-voxel, is used for three-dimensional image analysis. An air exchange unit is evaluated using a volume of approximately 2 cm^3 [107] that contains a cluster of CT voxels with a resolution of approximately 1 mm $\times$ 1 mm $\times$ 3 mm. The CT image of a patient with lung cancer can be pre-processed by segmenting into a small number of super-voxels, where each super-voxel contains a cluster of voxels with similar features and forms perceptually meaningful anatomic features. Drawing on this principle, the current study devised a super-voxel-based method for analyzing the function ability of the segments from the feature of super-voxels and combining the airway transport aspect into the ventilation image generation. The ventilation images generated are based on CT image in the absence of DIR. The results are robust and expected to be directly interpretable and meaningful for predicting the outcomes of patients with lung cancer.

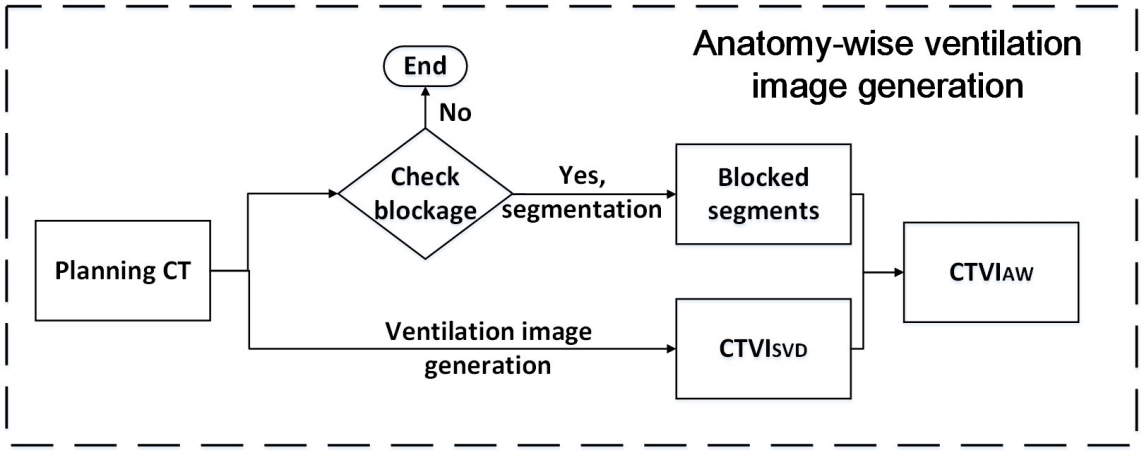

Figure 15: The overall workflow of the anatomy-wise lung ventilation image generation. The planning CT images are used to check if any bronchial airway is blocked. If tumor blocks the airway, then perform pulmonary segments' segmentation and identify the blocked segments. The blocked segments are applied to the generation of $\mathrm{CTVI_{AW}}$ (the anatomy-wise ventilation image) by assigning the functional value in the blocked segments of the $\mathrm{CTVI_{SVD}}$ (super-voxel-based lung ventilation image) to zero.

4.2 Methods and materials

4.2.1 The workflow of the study

In this study, we propose a novel approach for anatomy-wise lung ventilation imaging that takes into account both the air transport in the airway and the air exchange ability in the pulmonary alveoli. To assess the air exchange ability, we employ a super-voxel feature-based method to evaluate the function of each super-voxel and generate the initial CTVI ($CTVI_{SVD}$). For air transport, we used the Atlas-based method that automatically segments pulmonary segments, which allows us to identify tumor-blocked segments. In $CTVI_{SVD}$, the functional value of the tumor-blocked segments is assigned as 0, generating the final anatomy-wise ventilation image $CTVI_{AW}$. The overall flow chart of the $CTVI_{AW}$ generation is shown in Figure 15. Other CTVI methods will be generated and compared with our results. The CT_{ex} and CT_{in} were used to calculate the DIR-based ventilation images ($CTVI_{HU}$ and $CTVI_{Jac}$). A clustering method was used to generate super-voxels, and the feature of the super-voxel was used to calculate the ventilation images $CTVI_{SVD}$ without considering the tumor blockage. The results of $CTVI_{SVD}$ and the DIR-based CTVIs were compared with RefVI for the patients without tumor blockage. For the patients shown tumor blocking the airway, the $CTVI_{SVD}$ and $CTVI_{AW}$ will be compared with the RefVI. The details are presented in the following sections.

4.2.2 Patient data

Sixty-six patients with ventilation images (SPECT/PET) from two sources were included for the evaluation of $CTVI_{SVD}$ and $CTVI_{AW}$. The first dataset includes 20 patients from The Cancer Imaging Archive (TCIA) public access (https://doi.org/10.7937/3ppx-

7s22) [106], for this cohort of 20 patients, each individual underwent a comprehensive imaging protocol, including the following scans: a 4DCT scan, two inhale/exhale breath-hold CT (BHCT) scans, a Galligas PET scan and an attenuation correlation CT scan. All imaging acquisitions took place at the Royal North Shore Hospital between 2013 and 2015 using a Siemens Biograph mCT.S/64 PET/CT scanner located in Knoxville, USA. The 4DCT scans were performed using a helical acquisition technique with tube settings at 120 kVp and 80-200 mA. Two separate BHCT scans were conducted—one during inhalation and another during exhalation. The BHCT settings included 120 kVp, 120 mAs, and a breath-hold time of 10 seconds. The Galligas PET scans along with the corresponding attenuation correction CT, was acquired under free-breathing conditions. The field of view for the CT images was approximately 50 cm from the pharynx to the stomach. Since there were no time-averaged 4DCT images in the dataset, the CT_{ex} images were used for the bronchopulmonary segments' segmentation. The second dataset contains 46 patients from the VAMPIRE challenge [34]. Among them, 21 patients underwent 4DCT and diethylenetriamine pentaacetate (DTPA)-SPECT scans at Stanford University, USA [107]. All patients provided written informed consent to participate in a clinical trial of 4DCT ventilation imaging approved by the institutional review board for a study by Yamamoto [107]. Ten breathing phase CT images and a time-average CT with a slice thickness of 2.0, 2.5, or 3.0 mm were available for each patient. The average time between 4DCT and the following DTPA-SPECT scans, which include low-dose attenuation correction CT was 4 ($\pm$ 5) days. Rigid registration was performed between each SPECT image and the time-average CT image using Mattes mutual information rigid registration in Plastimatch. The DTPA-SPECT scans were linearly interpolated to match

the dimensions of the time-average CT image [34]. For these 21 patients, the time-averaged 4DCT images were used for the bronchopulmonary segments segmentation. The other 25 lung cancer patients from Peter MacCallum Cancer Centre have images with Galligas 4DPET/CT, 4DCT [108–110]. The 4DCT scan was performed using a low-dose cine-mode chest protocol, and the resulting scans were reconstructed into five respiratory phase bins. The in-plane resolution was 1.07 mm $\times$ 1.07 mm, and the slice thickness was 5 mm. The 4DPET scans had an in-plane resolution of 2.86 mm $\times$ 2.86 mm and a slice thickness of 3.3 mm. These scans were inherently coregistered to the 4DCT phase images. For these 25 patients, the $\mathrm{CT_{ex}}$ scans were used for the bronchopulmonary segments segmentation since there were no time-averaged 4DCT images in this dataset. The CT values were converted to density values using Equation (13), as follows:

$$Density = (\frac{HU + 1000}{1000}) \tag{13}$$

Among these 66 patients, 11 patients shown with tumor blocking one or several segments, other 55 patients without tumor blocking the airway. For the 55 patients without tumor blocking the airway, the $\mathrm{CTVI_{SVD}}$ were the same as the $\mathrm{CTVI_{AW}}$. These patients were used to evaluate the $\mathrm{CTVI_{SVD}}$, which were similar to the feature-based methods. Fot the 11 patients shown the segment(s) with tumor blockage, $\mathrm{CTVI_{AW}}$ were different from the $\mathrm{CTVI_{SVD}}$, the ventilation value of the blocked segments were 0 in the $\mathrm{CTVI_{AW}}$ which should be closed to the RefVI while the $\mathrm{CTVI_{SVD}}$ had other values.

4.2.3 DIR-based CTVI methods

The two main conventional DIR-based methods are $CTVI_{HU}$ and $CTVI_{Jac}$. Both methods require DIR between the CT_{in} and CT_{ex}. In $CTVI_{HU}$, a voxel at spatial position p of the CT_{ex} is mapped toward a voxel at spatial position p' of the CT_{in} by DIR. The ventilation value at position x can be directly calculated using Equation (1) [34]. In $CTVI_{Jac}$, the volume change of a voxel at position p is calculated using the determinant of the Jacobian of the deformation field at position p. This process is performed using Equation (2). Both $CTVI_{HU}$ and $CTVI_{Jac}$ images were calculated in this study and used for comparison. DIR between the CT_{in} and CT_{ex} was performed using MIMvista 6.3.4 (MIM Software Inc., Cleveland, OH, USA) with a default spacing resolution of 3mm.

4.2.4 Super-voxel clustering method

SLIC [67] is applied to lung CT 3D images to generate super-voxels with low computational power requirements. The SLIC algorithm first initializes the K_{init} seeds by resampling pixels on a regular grid. Then, it assigns each voxel to the closest seed point to generate K_{init} clusters based on the distance ($Dist$), as described by Equation (14):

$$Dist = \sqrt{dist_c^2 + (\frac{dist_s}{S})^2 \times m^2} \tag{14}$$

where $dist_c$ is the HU value difference, $dist_s$ is the Euclidean distance, S is the initial sampling interval $S = \sqrt{\frac{N}{K_{init}}}$, N is the total voxel number in the lung volume, and m is a weighting value used to control the compactness of the super-voxel. Next, the positions of the centers are moved to the point with the smallest gradient to prevent

placement on the edges of an image or at a noisy voxel. The above steps are repeated until the result converges. Only the super-voxels in the lung mask were used in this study. An in-house tool based on Matlab (MathWorks Inc, Natick, MA, USA) was used, and K_{init} was set as 1,500 for all patients (refer to the Discussion section for commentary). The number of super-voxels generated varied between the patients according to their lung anatomy. All of the CT and RefVI images were interpolated into images of the same size and with a pixel size of 2 mm × 2 mm × 2 mm, and a 3D median filter with dimensions of 5 voxels × 5 voxels × 5 voxels was applied to the images to reduce noise.

4.2.5 Feature selection of the super-voxel

As shown in Figure 16, a super-voxel map was generated on CT_{ex} images. To select the most correlated feature of the super-voxel to represent the ventilation function of the super-voxel, sixteen intensity-based statistical features [117, 118] and one modified mean feature ($\overline{\overline{Mean}}$ representing the product of the air and tissue of the super-voxel) were calculated and analyzed the correlation with the mean ventilation value ($Vent_{mean}$) using the 55 patients without tumor blockage. The selected features were listed in Table 4. The reason of choosing $\overline{\overline{Mean}}$ as one of the features is that the lung diseases could causing the lung density change. Some diseases may cause the density increase such as the consolidation of the tumor and abnormal tissues, which have a high density but should have a low ventilation value, the other may cause the increase of density like emphysema. The $\overline{\overline{Mean}}$ was calculated as Equation 15 which was proposed by Kipritidis [43]. The $Mean$ is the mean fraction of the tissue in the super-voxel, while (1 - $Mean$) is the mean fraction of the air. The $Vent_{mean}$

was calculated using RefVI image data by mapping the super-voxel segmentation results on the RefVI images, as both the RefVI and time-average CT data were registered, and the time-average CT and CT_{ex} images shared the same position. The correlation between the feature and $Vent_{mean}$ of the super-voxels was determined using Spearman's correlation analysis. The most correlated feature was selected as the surrogate of the ventilation function of the super-voxel.

$$\overline{\overline{Mean}} = Mean \times (1 - Mean) \tag{15}$$

4.2.6 Super-voxel based ventilation generation

The $D_{\overline{\overline{Mean}}}$ of the super-voxel has the highest correlation with $Vent_{mean}$, which was used as the surrogate of the ventilation function of the super-voxel.

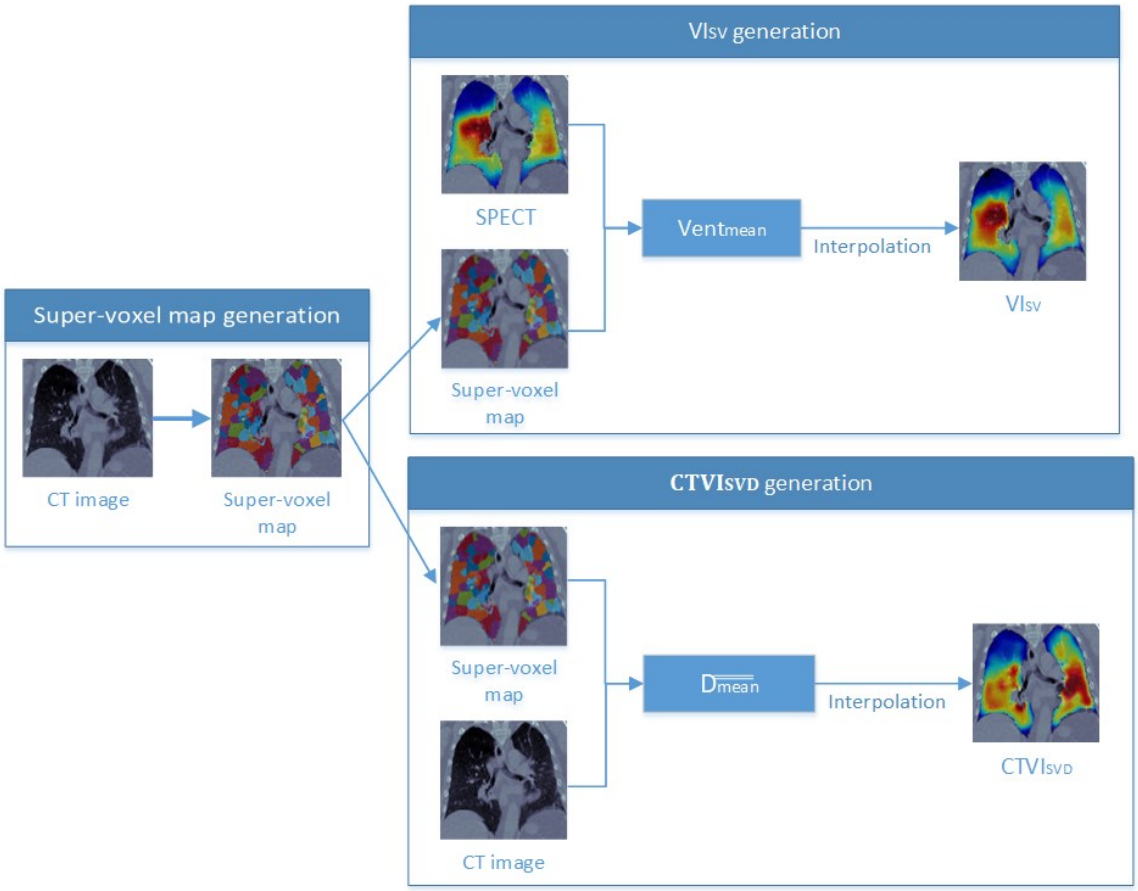

Figure 16: The generations workflow of the $\mathrm{CTVI_{SVD}}$ and $\mathrm{VI_{SV}}$.

Figure 16 shows the workflow for generating the $\mathrm{CTVI_{SVD}}$ images and the ventilation images based on SPECT $\mathrm{VI_{SV}}$. $\mathrm{CTVI_{SVD}}$ image generation requires only a $\mathrm{CT_{ex}}$ image, while $\mathrm{VI_{SV}}$ images require both $\mathrm{CT_{ex}}$ and SPECT images. To demonstrate the feasibility of generating a reasonable ventilation image using hundreds of super-voxels, we generated the $\mathrm{VI_{SV}}$ image and compared it with a RefVI image. The details of $\mathrm{CTVI_{SVD}}$ are presented as follows. To perform $\mathrm{CTVI_{SVD}}$, we used the geometric center of a super-voxel to represent the position of the super-voxel and the $D_{\overline{\overline{Mean}}}$ value as the ventilation value of the super-voxel center positions. The ventilation values of all of the voxels in a lung were then calculated via interpolation with the $D_{\overline{\overline{Mean}}}$ of the super-voxels, as follows (Equations (16) and (17)):

$$V = W \times V_{sup} \tag{16}$$

$$w_{ij} = e^{-(\frac{r_{ij}}{r_{mean}})^2} \tag{17}$$

where V is the vector of the ventilation value of all voxels in the lungs; V_{sup} is the vector calculated only using the $D_{\overline{\overline{Mean}}}$ of the super-voxel; W is the interpolation weight matrix; w_{ij} is the element of the W matrix, which is calculated based on the distance between voxel i and the center position of super-voxel j, as shown in Equation (17); r_{mean} is the mean distance between the super-voxels; and r_{ij} is the distance between voxel i and super-voxel j. The lung volume was divided into the left and right lungs. The ventilation value was interpolated for each voxel using only the super-voxels from the ipsilateral lung. To smooth the final CTVIs, we applied a 3D Gaussian filter with a kernel size of three voxels to each lung voxel. The same

post-processing steps were applied to all CTVIs. The $Vent_{mean}$ of the super-voxels from RefVI was used to generate the $\mathrm{VI_{SV}}$ according to the above-stated interpolation method and the correlation between $\mathrm{VI_{SV}}$ and RefVI was evaluated. Two more super-voxels-based ventilation images were also generated for comparison. The $Vent_{mean}$ of the super-voxels from $\mathrm{CTVI_{HU}}$ and $\mathrm{CTVI_{Jac}}$ was used to generate the $\mathrm{CTVI_{SVHU}}$ and $\mathrm{CTVI_{SVJac}}$ with a similar method as $\mathrm{VI_{SV}}$, respectively. Their correlations with RefVI were also evaluated.

4.2.7 The evaluation of the $\mathbf{CTVI_{SVD}}$ and also for the $\mathbf{CTVI_{HU}}$, $\mathbf{CTVI_{Jac}}$, $\mathbf{CTVI_{SVHU}}$, and $\mathbf{CTVI_{SVJac}}$

The $\mathrm{CTVI_{SVD}}$ images generated in this study were evaluated with the corresponding RefVI images using voxel-wise Spearman correlation analysis. Spearman correlation analysis was also used to compare RefVI images with $\mathrm{CTVI_{HU}}$, $\mathrm{CTVI_{Jac}}$, $\mathrm{CTVI_{SVHU}}$, and $\mathrm{CTVI_{SVJac}}$ images. The comparison between the $\mathrm{CT_{ex}}$ and RefVI was used to show the advantages of analysis at the super-voxel level compared to the voxel level. To assess the concordance of high-functioning regions between CTVI and RefVI, RefVI and $\mathrm{CTVI_{SVD}}$ images from each patient were divided into two volumes by the 66^{th} percentile ventilation value in the lung, which is used to distinguish high- and low-functioning lung regions. This value has been used by other studies [45, 80]. The DSC was used to assess the accuracy of $\mathrm{CTVI_{SVD}}$ in segmenting the high- and low- functioning lung regions. The DSC was also used to compare the high- and low-functioning lung regions segmented by RefVI with those segmented by $\mathrm{CTVI_{HU}}$, $\mathrm{CTVI_{Jac}}$, $\mathrm{CTVI_{SVHU}}$, and $\mathrm{CTVI_{SVJac}}$. Only the intersection between the CT and RefVI lung masks was analyzed in this study.

4.2.8 Impact of the super-voxel number on $\mathbf{CTVI_{SVD}}$ experiments

The size of the super-voxels may influence the results of $\mathrm{CTVI_{SVD}}$. On the one hand, super-voxels that are too large may not be able to identify small defects. On the other hand, super-voxels that are too small may lose their structure-oriented properties. A particular clustering may influence the results of $\mathrm{CTVI_{SVD}}$. For example, by increasing the number of super-voxels, the size of clusters is reduced. To investigate how the size of the super-voxels influences the results, we measured the correlation of $D_{\overline{\overline{Mean}}}$ with $Vent_{mean}$ for different numbers of super-voxels. Performance was evaluated at various values of K_{init} (300, 500, 800, 1,000, 1,500, 2,000, 2,500, 3,000, 4,000, 8,000, 12,000, and 15,000) to cover an extensive range. A large value of K_{init} increases the calculation time and depletes the memory needed to calculate the interpolation matrix W, as described in section 2.5. The computer used for this analysis was equipped with an Intel® Core™ i9-11900K 3.50-GHz processor and 64.0 GB of RAM.

4.2.9 The evaluation of the $\mathbf{CTVI_{AW}}$

As mentioned above, for the 55 patients without tumor blocking the airway, their $\mathrm{CTVI_{AW}}$ are the same as $\mathrm{CTVI_{SVD}}$. The evaluation of these patients has been described in previous parts. For the 11 patients with tumor blocking the airway, the ventilation value in the blocked segments were different. Both the $\mathrm{CTVI_{SVD}}$ and $\mathrm{CTVI_{AW}}$ were compared with the RefVI using Spearman correlation analysis.

4.3 Results

4.3.1 Super-voxel segmentation

The SLIC method was used to divide the lung volumes of the 21 patients into 345–825 super-voxels at a K_{init} of 1,500. Figure 3 shows an example of super-voxel segmentation of the lung volume. Different colors indicate different super-voxel regions. The mean correlation between $\mathrm{VI_{SV}}$ and SPECT was 0.89 (range: 0.69 to 0.98). Figure 17 (B) and (C) show a comparison between RefVI and $\mathrm{VI_{SV}}$ images. The two images have a similar function distribution. The strong correlation between $\mathrm{VI_{SV}}$ and RefVI suggests that a reasonable CTVI image of the whole lung volume can be generated by analyzing hundreds of super-voxels.

4.3.2 Feature selection of the super-voxel

The correlation analysis of the 17 features with the $Vent_{mean}$ of the super-voxel is shown in Table 4. Nine features ($\overline{\overline{Mean}}$, Mean, Variance, Median, Minimum, 10^{th} percentile, Energy, Entropy, and Root mean square) show a absolute correlation value great than 0.40. The most correlated feature was the $\overline{\overline{Mean}}$ value of the super-voxel with a correlation value of 0.50 ± 0.15, which was selected as the surrogate of the ventilation function value to generate the $\mathrm{CTVI_{SVD}}$.

Table 4: The results of the feature selection as the surrogate of the ventilation function.

Feature name	Correlation value
Mean	0.46 ± 0.17
Variance	0.40 ± 0.21
Kurtosis	-0.12 ± 0.26
Median	0.41 ± 0.19
Minimum	0.42 ± 0.21
10^{th} percentile	0.42 ± 0.20
90^{th} percentile	0.39 ± 0.21
Maximum	0.37 ± 0.23
Interquartile range	0.27 ± 0.15
Range	0.27 ± 0.15
Mean absolute deviation	0.21 ± 0.15
Median absolute deviation	0.35 ± 0.17
Coefficient of variation	-0.12 ± 0.22
Energy	-0.42 ± 0.18
Entropy	0.41 ± 0.17
Root mean square	0.40 ± 0.21
$\overline{\overline{\textbf{Mean}}}$	**0.50 ± 0.15**

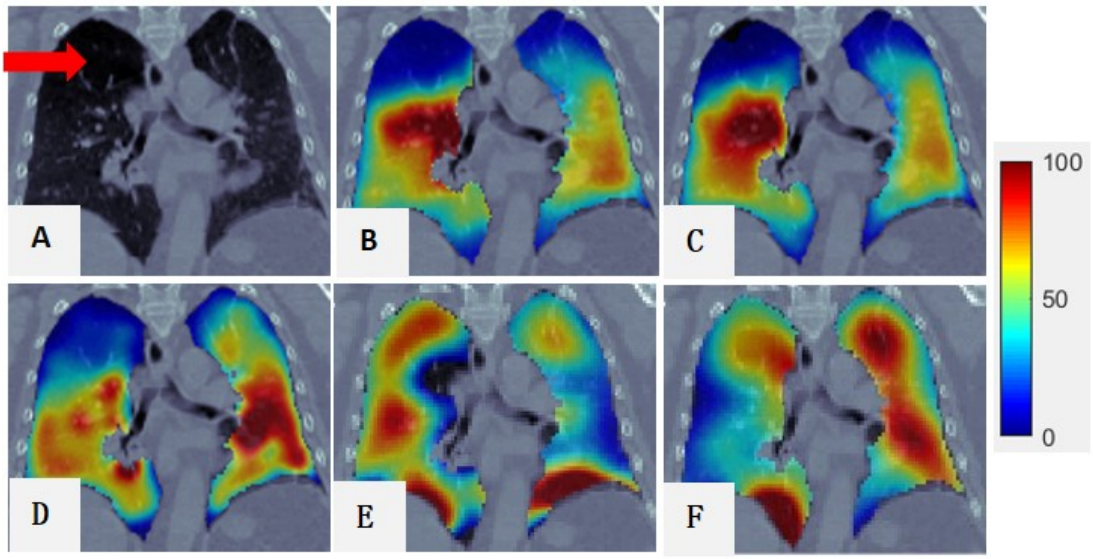

Figure 17: Comparison of RefVI image and CTVI_{SVD} images for a representative case without tumor blocking the airway. Figure (A) is CT; Figure (B) is the RefVI of the lung region superimposed onto the CT; Figure (C) is the VI_{SV} of the lung region superimposed onto the CT; Figure (D) is the CTVI_{SVD} of the lung region superimposed onto the CT; Figure (E) is the CTVI_{Jac} of the lung region superimposed onto the CT; Figure (F) is the CTVI_{HU} of the lung region superimposed onto the CT. For all the figures, their 99^{th} percentile and higher values were scaled to 100 (to reduce the artifact effect caused by the tracer deposited at airways in RefVI for visual inspection), and the minimum value was scaled to 0.

4.3.3 Comparison of $CTVI_{SVD}$, $CTVI_{HU}$, $CTVI_{Jac}$, $CTVI_{SVHU}$, and $CTVI_{SVJac}$ with RefVI

The correlation between the $D_{\overline{\overline{Mean}}}$ from CT and the $Vent_{mean}$ for the super-voxel volume from RefVI was 0.50 ± 0.15, indicating that super-voxels with a lower/higher mean density tend to have a lower function value. This moderate-to-strong correlation means that the $D_{\overline{\overline{Mean}}}$ of a super-voxel can be used as a surrogate for $Vent_{mean}$ when generating $CTVI_{SVD}$. Figure 17 presents a comparison of RefVI with $CTVI_{SVD}$. The low-functioning lung region, indicated by the red arrow in the CT image and by the blue and black-blue area in the ventilation image (Figure 17 (B)), can be identified using $CTVI_{SVD}$ (dark blue area in Figure 17 (D)). The mean correlation coefficient between $CTVI_{SVD}$ and RefVI was 0.59 (range: 0.31 to 0.82). The mean correlation coefficients of RefVI with $CTVI_{HU}$, $CTVI_{Jac}$, $CTVI_{SVHU}$, and $CTVI_{SVJac}$ were 0.34 ± 0.18, 0.20 ± 0.18, 0.38 ± 0.20, and 0.25 ± 0.24 respectively. These results indicate that $CTVI_{SVD}$ is closer to RefVI than conventional DIR-based methods. The super-voxel based method can improve the correlations of the DIR-based CTVIs by 0.04 and 0.05 for $CTVI_{HU}$ and $CTVI_{Jac}$, respectively. A similar improvement was also reported in Szmul's study [41].

The mean DSC values of the high-functioning (DSC_h) and low-functioning regions (DSC_l) on $CTVI_{SVD}$ images were 0.64 ± 0.09 and 0.77 ± 0.13, respectively. Because the criterion for dividing the lung is the 66^{th}, the low-functioning region is larger than the high-functioning region, and DSC_l is higher than DSC_h. As shown in Figure 17, the locations of the low-functioning regions on the $CTVI_{SVD}$ images matched those on the SPECT images, but the highest-functioning regions (dark red area) just exhibited a certain amount of overlap. The mean DSC_h values of $CTVI_{HU}$,

$CTVI_{Jac}$, $CTVI_{SVHU}$, and $CTVI_{SVJac}$ were 0.46 ± 0.13 and 0.43 ± 0.13, 0.49 ± 0.11, and 0.47 ± 0.16, respectively, and the corresponding mean DSC_l values were 0.72 ± 0.12, 0.70 ± 0.15, 0.73 ± 0.12, and 0.72 ± 0.13, respectively.

For some patients, $CTVI_{SVD}$ yielded low correlation with SPECT. However, this could be improved. As indicated by the red arrow in Figure 18 (A), a defective lung region with a high density at the top of the left lung caused a falsely high ventilation value, as shown in Figure 18 (C). Such errors can be corrected by manually contouring the defect regions via assignment to a low ventilation value. In this case, the final correlation coefficient increased to 0.52, as shown in Figure 18 (D).

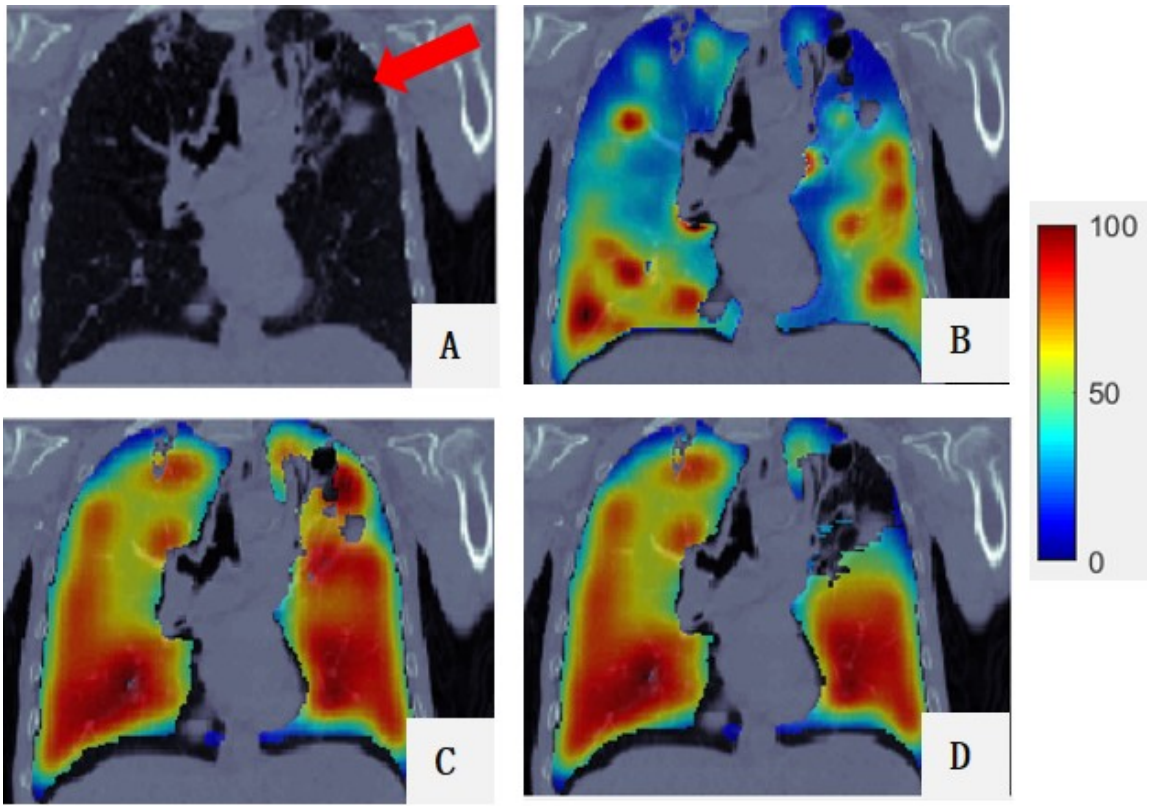

Figure 18: Comparison of RefVI and $CTVI_{SVD}$ images for a representative case. (A) is CT; (B) is the RefVI of the lung region superimposed onto the CT; (C) is the origin $CTVI_{SVD}$ of the lung region superimposed onto the CT; (D) is the corrected $CTVI_{SVD}$ of the lung region superimposed onto the CT;. For all the figures, their 99^{th} percentile and higher values were scaled to 100, and the minimum value was scaled to 0.

4.3.4 Evaluation of the impact of the super-voxel number on $\mathbf{CTVI_{SVD}}$

Figure 19 shows super-voxel segmentation using two values of K_{init}. As the number of super-voxels increased, the size of the super-voxels decreased. The generated $\mathrm{CTVI_{SVD}}$ images show high similarity in highly ventilated regions. As shown in the bottom left row of Figure 19, as the volume of the super-voxel decreased, it became more difficult to contain the whole texture of the sub-region; this presents an obstacle to analysis of the $Vent_{mean}$ with other features of such a super-voxel. Table 5 shows the experimental results obtained with different numbers of super-voxels. On average, approximately 201, 297, 405, 463, 597, 708, 823, 923, 1,148, 1,921, 2,664, and 3,197 super-voxels were extracted from the lung volumes of the 21 patients when K_{init} was set as 300, 500, 800, 1,000, 1,500, 2,000, 2,500, 3,000, 4,000, 8,000, 12,000, and 15,000, respectively. The correlation of $D_{\overline{\overline{Mean}}}$ with $Vent_{mean}$ was strongest when approximately 597 super-voxels were extracted from the lung volume and decreased as the number of super-voxels continued to increase. A paired-samples t-test to compare the $D_{\overline{\overline{Mean}}}$ and $Vent_{mean}$ obtained at a K_{init} of 1,500 with those obtained at other K_{init} values revealed that a K_{init} of 1,500 generated the most reasonable number of super-voxels inside the lungs. The $D_{\overline{\overline{Mean}}}$ exhibited a stronger correlation with $Vent_{mean}$ at a K_{init} of 1,500 than at K_{init} values lower than 1,500 and higher than 3,000. Thus, K_{init} was set as 1,500 to retain as many structure-oriented properties as possible for each super-voxel.

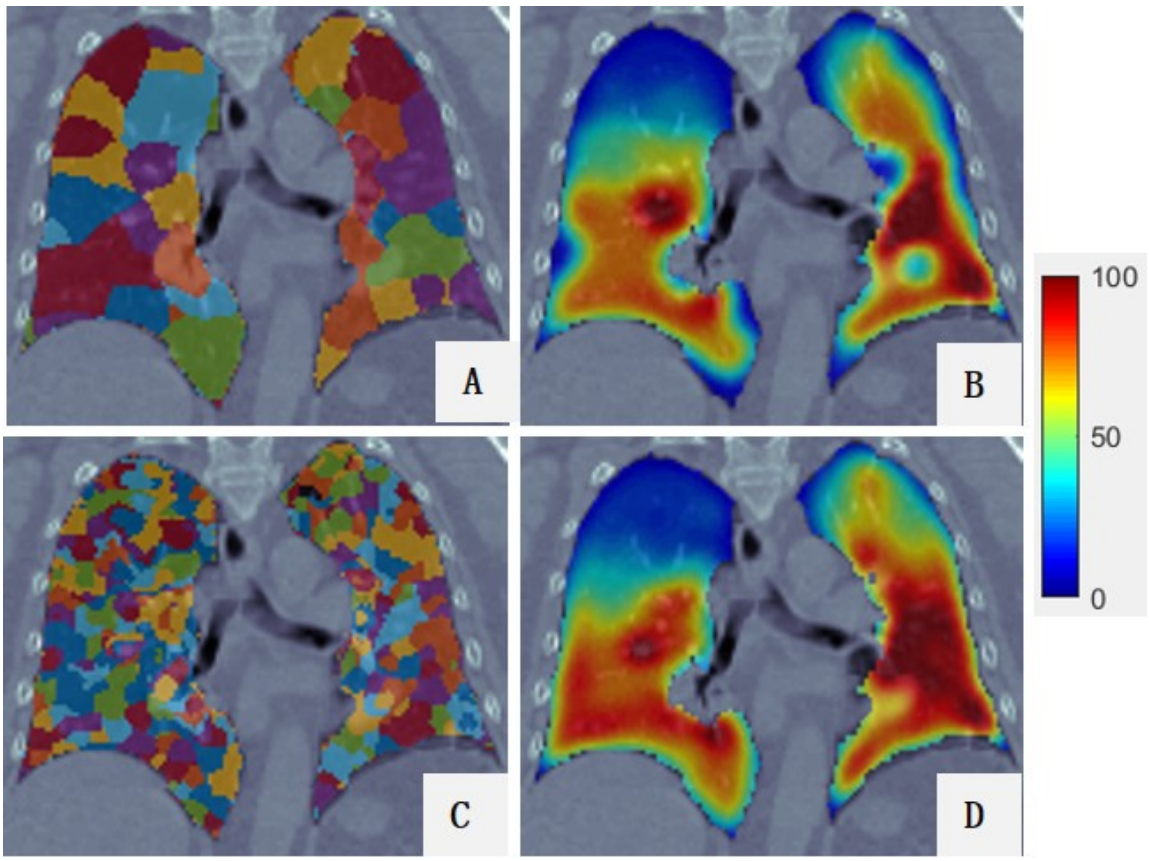

Figure 19: Two different super-voxel segmentations with different K_{init} and the corresponding CTVI_{SVD}. The K_{init} of the top row is 500, and the bottom row is 120000.

Table 5: The influence of the different numbers of the super-voxel. K_{init} means the initial setting of the super-voxel number for the CT image, and K_{final} means the final extracted super-voxel number in the lung volume. The mean correlation value is the mean Spearman correlation value of all the patients. $D_{\overline{\overline{Mean}}}$ is the mean product of the tissue and air of the super-voxel, and $Vent_{mean}$ is the mean ventilation value of the super-voxel. The p-values are obtained from the paired-samples T-test of the K_{init} of other value with the K_{init} of 1500.

K_{init}	K_{final}	Mean correlation value	
		$D_{\overline{\overline{Mean}}}$ vs $Vent_{mean}$	p-value
300	201	0.44 ± 0.15	< 0.0001
500	297	0.44 ± 0.16	< 0.0001
800	405	0.47 ± 0.14	0.0016
1000	463	0.49 ± 0.14	0.0079
1500	597	0.50 ± 0.15	–
2000	708	0.50 ± 0.14	0.2908
2500	823	0.50 ± 0.14	0.2715
3000	923	0.50 ± 0.14	0.3697
4000	1148	0.49 ± 0.14	0.2497
8000	1921	0.46 ± 0.14	0.0100
12000	2664	0.46 ± 0.14	0.0064
15000	3197	0.45 ± 0.15	0.0031

4.3.5 The evaluation of the $CTVI_{AW}$ for the patient with blocked pulmonary segments

For the 11 selected patients, Table 6 shows the blocked pulmonary segments and their Spearman correlation between the $CTVI_{SVD}$ and $CTVI_{AW}$ with the RefVI. The mean Spearman correlation between $CTVI_{AW}$ with RefVI was 0.72 ± 0.05 for all 11 patients. This indicates a relatively strong positive correlation between the $CTVI_{AW}$, which represents the ventilation image considering tumor-blocked segments, and the actual ventilation distribution observed in the RefVI. Comparatively, the Spearman correlation for the $CTVI_{SVD}$ was lower at 0.51 ± 0.14. The $CTVI_{SVD}$ represents the ventilation image, which does not account for the tumor blockage. Figure 20 provides a visual comparison between the $CTVI_{SVD}$, $CTVI_{AW}$, and the RefVI for a patient with a blocked pulmonary segment. The results indicate that considering the segment lost function due to the tumor blockage (represented by $CTVI_{AW}$) leads to a higher correlation with the actual ventilation distribution.

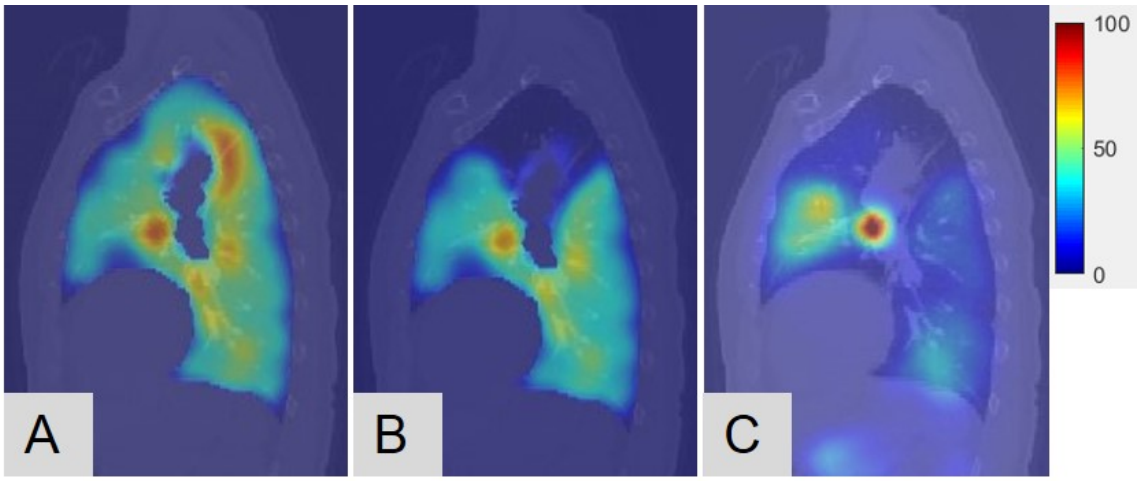

Figure 20: The sagittal view of an example of the tumor blocking the left lung apico-posterior segment. A is the overlap of the CT image with CTVI_{SVD} (super-voxel-based lung ventilation image), B is the overlap of the CT image with CTVI_{AW} (anatomy-wise lung ventilation image), and C is the sagittal view of the overlap of the CT image with the RefVI (reference ventilation image). All the ventilation images are scaled to 0-100 for demonstration. The voxels with functional value of zero in the ventilation images means the voxels have lowest functional ability, while the voxels with functional value of 100 means the voxels have highest functional ability.

Table 6: The results of comparing the patients' functional images with the segment blocked. The blocked regions mean the blocked segments caused by the tumor, R represents the tumor located in the right lung, L means the tumor was located in the left lung. The numbers behind the underline mean the code name of the segment referred to Table 2. The last two columns show the Spearman correlation results between the patients' RefVI with the $CTVI_{SVD}$ and $CTVI_{AW}$, respectively.

Patient ID	Blocked segments	$CTVI_{SVD}$	$CTVI_{AW}$
P1	L_1	0.71	0.78
P2	R_123	0.64	0.74
P3	R_678910	0.50	0.67
P4	R_123	0.47	0.72
P5	L_5678	0.33	0.65
P6	R_1	0.59	0.68
P7	R_123	0.43	0.79
P8	R_1	0.58	0.67
P9	R_123	0.69	0.74
P10	R_678910	0.39	0.78
P11	R_678910	0.30	0.72
Average	–	0.51 ± 0.14	0.72 ± 0.05

4.4 Summary and discussion

In this study, an anatomy-wise lung ventilation imaging method by considering the both air transport and the feature of lung parenchyma was developed to generate surrogate ventilation images directly from CT images. For the analysis of the lung parenchyma feature, the SLIC method was employed to generate super-voxels inside the lung volume, and the $D_{\overline{\overline{Mean}}}$ of the super-voxels was used as a surrogate for the mean ventilation value. This novel CTVI_{AW} method achieved a mean Spearman's correlation coefficient of 0.59 (range: 0.31 to 0.82) with the RefVI, which was significantly higher than the correlation coefficients of RefVI with the DIR-based methods CTVI_{HU} (0.34 $\pm$ 0.18, p <0.05), CTVI_{Jac} (0.20 $\pm$ 0.18, p <0.05), $\text{CTVI}_{\text{SVHU}}$ (0.38 $\pm$ 0.20, p <0.05), and $\text{CTVI}_{\text{SVJac}}$ (0.25 $\pm$ 0.24, p <0.05) for the 55 patients without tumor blockage. By using this novel method, the complexity of a ventilation imaging problem can be reduced from calculating millions of ventilation values for all voxels to only calculating hundreds of $Vent_{mean}$ values for super-voxels. The $Vent_{mean}$ of a super-voxel can be directly derived from super-voxel features. For the 11 patients with tumor blocking the airway, the mean Spearman correlation between CTVI_{AW} with RefVI was 0.72 $\pm$ 0.05 which was higher than the mean Spearman correlation between CTVI_{SVD} and RefVI with value of 0.51 $\pm$ 0.14. Thus, by considering the segment lost function due to the tumor blockage (represented by CTVI_{AW}) leads to a higher correlation with the actual ventilation distribution.

This study shows that the $D_{\overline{\overline{Mean}}}$ of a super-voxel is strongly correlated with the $Vent_{mean}$ of a super-voxel, which means that a lower or higher super-voxel density is usually associated with less functional ventilation than a higher super-voxel density. Similar results have been shown in other studies [69, 70]. As shown in Figure 17, the

region with low ventilation function (indicated by arrows) is darker than the region with normal function. The low-functioning region may correspond to a defective lung region caused by emphysema, where healthy pulmonary tissue has been replaced increasingly by air due to alveolar damage and weakening and rupture of the inner walls of the air sacs. This was a preliminary study of the use of the mean density of super-voxels to generate ventilation images. Other super-voxel features can be analyzed and combined with $D_{\overline{\overline{Mean}}}$ to build a more accurate and robust model for future CTVI studies involving more patient data.

This study has some limitations. Pulmonary ventilation refers to the air exchange between the atmosphere and the lungs. It involves the inflow of air through the airway to the alveoli, where the air exchange occurs, followed by outflow through the airway. Our results show that lung regions with lower density values exhibit lower ventilation values than those with higher density values. As previously mentioned, the damaged alveoli in a patient with emphysema lost their ability to expel air, leading to decreased intensity. However, in some cases, abnormal lung regions associated with pulmonary diseases can exhibit increased density, known as opacities, and fall into four patterns: consolidation, interstitial, nodules or masses, and atelectasis [119]. These diseases can also obstruct the airway or damage to the parenchyma, leading to a loss of air exchange capability. Consequently, some pulmonary diseases may affect the CTVI results in this study. However, the clinical presentation of pulmonary diseases on CT images can vary. Raju et al. categorized the signs of the lung disease into 22 groups [120]. These signs can increase the difficulty of automatically recognizing defect regions. In this study, the super-voxel was the smallest unit of analysis and its features can be used directly to classify it as a defect or normal region. In future work,

we will create a super-voxel-based model to automatically identify defect regions and correct the ventilation value to increase the accuracy of our method.

5 Anatomy-wise lung ventilation image for functional lung avoidance planning

5.1 Introducion

Studies have revealed that lung function can change during or after RT treatment [48, 51, 94, 113, 121]. According to Yuan's study [48], low ventilation in certain lung regions may arise due to tumor-induced pressure on the airway and blood vessels. However, these regions may experience recovery after RT, particularly in lung cancer patients with centrally located tumors. These lung regions must be carefully protected during the treatment with minimum dose deposition since the lung function may recover after tumor shrinkage [113, 114]. However, to the best of our knowledge, no study has been conducted to consider the recoverable low functional volume (rLFV) during the planning design before the treatment.

To further analyze the blocked regions and ascertain whether they are normal or dysfunctional due to lung disease, one approach could be to utilize CTVI methods to evaluate blocked regions on CT images. For the DIR-based method, blocked regions would be classified as dysfunctional since the lack of airflow into these areas causes density/volume changes. The current deep learning methods may also classify all blocked regions as dysfunctional if the model has been trained on patterns observed in RefVI. In this study, we employed a super-voxel-based method in previous chapter, which specifically considers lung parenchymal features without airway circulation [122]. This approach aids in identifying whether the lung regions are normal or dysfunctional due to lung parenchymal variation.

5.2 Methods and materials

5.2.1 The overview of the study

In this study, we propose a novel approach for anatomy-wise lung ventilation imaging that takes into account both the air transport in the airway and the air exchange ability in the pulmonary alveoli. To assess the air exchange ability, we employ a super-voxel feature-based method to evaluate the function of each super-voxel and generate the initial CTVI_{SVD}. For air transport, we used the Atlas-based method to automatically segment pulmonary segments, which allows us to identify tumor-blocked segments. In CTVI_{SVD}, the functional value of the tumor-blocked segments is assigned as 0, generating the final anatomy-wise ventilation image CTVI_{AW}. Subsequently, the overlap between the tumor-blocked segments with the high function regions identified by super-voxel feature-based method was considered as the rLFV. Lastly, we explore the integration of rLFV into treatment planning to evaluate its effectiveness in preserving lung function. We compared this approach to conventional treatment planning and the current FLART approach, which does not consider rLFV.

5.2.2 Patient data

The data collection for this study comprises images obtained from 20 patients with locally-advanced, non-small cell lung cancer who underwent chemoradiotherapy [123, 124]. The images consist of 4D fan beam CTs (4D-FBCT) and 4D cone beam CTs (4D-CBCT). The 4D-FBCT images were acquired using a 16-slice helical CT scanner (Brilliance Big Bore, Philips Medical Systems, Andover, MA) as respiration-correlated CTs, capturing 10 breathing phases (0 to 90%, phase-based binning) with a slice thickness of 3 mm. These 4D-FBCT images were obtained during the initial

simulation before therapy and were used for treatment planning. Additionally, in 13 of the 20 subjects, 4D-FBCT images were acquired weekly on the same scanner during the course of therapy. The target structures were delineated by a physician on the weekly 4D-FBCTs images. However, due to the extensive size of the dataset, contouring of organs at risk (OARs) was performed only on a subset of images. From this subset, five patients with central tumors exhibited positive responses (the tumor size reduced at least 30%) to treatment. As shown in Figure 21, two selected patients demonstrated tumors that blocked the airway bronchial connecting to the corresponding lung segment initially. However, after undergoing treatment, the tumors shrank, and the airway obstruction was relieved. This observation is in line with the hypothesis that tumor-induced airway blockages may impact downstream lung function, and radiotherapy can lead to tumor regression and subsequent lung ventilation improvement. For these five patients, the rLFV was first identified and then used for treatment planning, while the treatment plans of the other 15 patients were performed without rLFV. For treatment planning, the ten phases of 4DCT were utilized to generate an average-CT, which was used as the basis for treatment planning. The prescription dose was 66 Gy using daily 2 Gy fractions.

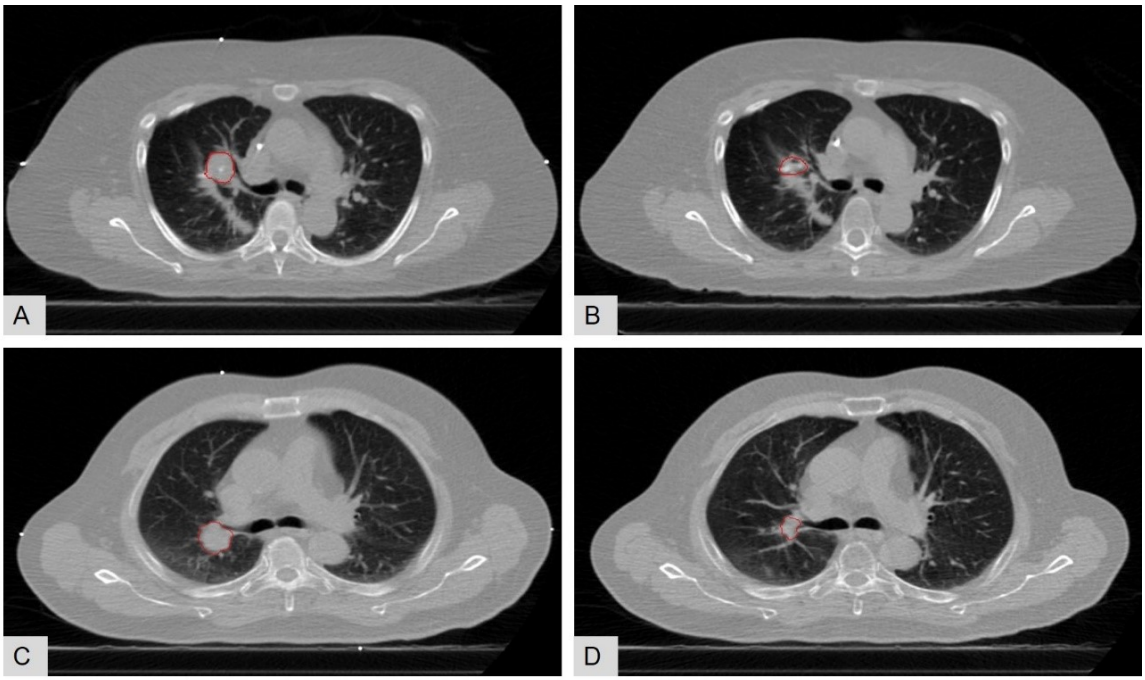

Figure 21: The comparisons of the tumor before and after the treatment. The upper row figures are for the first patient. Figure (A) is before the treatment, and Figure (B) is after the treatment. The lower row figures are for the first patient. Figure (C) is before the treatment, and figure (D) is after the treatment.

5.2.3 Ventilation image generation and classification

In our study, the ventilation images ($CTVI_{SVD}$ and $CTVI_{AW}$) were generated using the method described in abovementioned parts. As Figure 22 shown, to distinguish between HFV and LFV regions for each patient, the 66^{th} percentile ventilation value in the lung will be used as the threshold value. Based on this threshold, the $CTVI_{AW}$, which represents the ventilation image considering tumor blockages, will be divided into HFV and LFV regions. Furthermore, for the five patients with temporarily blocked segment regions, the overlap between the tumor-blocked segments with the high function regions identified by super-voxel feature-based method was considered as the rLFV. These rLFV contours represent regions with temporary airway blockages that could potentially recover and become high function after treatment. The rest of the LFV regions were formed to be the uLFV, representing the regions that won't recover to become high function after treatment. The overlap regions between the planning target volume (PTV) and the high ventilation regions (HFV and rLFV) will be excluded from the high ventilation regions. These contours, including HFV, rLFV, and uLFV, will play a crucial role in functional lung avoidance treatment planning. This approach is designed to minimize radiation exposure to high-functional regions of the lung, aiming to better preserve lung function and reduce the risk of RILI.

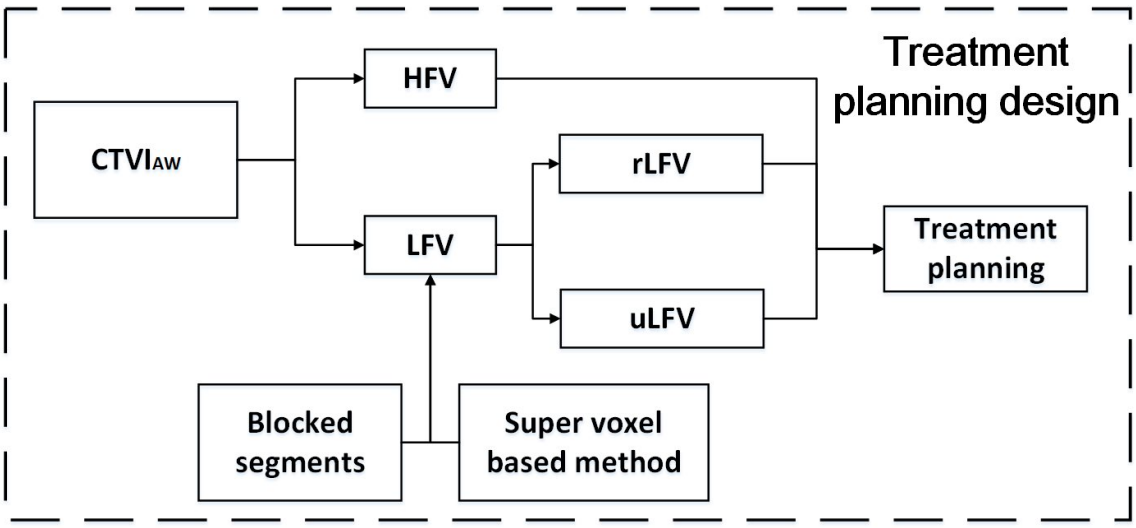

Figure 22: The overall workflow of the identification of the tumor-blocked regions and apply to the treatment planning. The rLFV regions is the lung regions with normal parenchyma feature in the blocked segments. Abbreviations: LFV, low functional volume; HFV, high functional volume; rLFV, recoverable LFV; uLFV, unrecoverable LFV.

5.2.4 Planning technique

In this study, three IMRT plans, namely aPlan, fPlan, and rfPlan, were created for the five patients with tumors that shrank after treatment. The first plan, aPlan, was optimized solely for anatomical lungs. Subsequent IMRT plans, fPlan, and rfPlan, were optimized for HFV or HFV + rLFV lung functional volumes, respectively. For rfPlan, HFV has higher priority than rLFV. For the other 15 patients, only aPlan and fPlan were created since no rLFV was found in these patients. The goal of these subsequent plans was to minimize the dose to functional volumes while attempting to meet dose constraints based on RTOG 0617 guidelines, including MLD <20 Gy and V20 <37%. To evaluate the dose to the functional volumes, functional dose metrics such as $sV5$, $sV20$, and $sMLD$ were calculated.

The IMRT planning was carried out using the Eclipse TPS version 11 (Varian Medical Systems, Palo Alto, California, USA). The dose calculation was performed using an analytic anisotropic algorithm (AAA V.11.0.21) with a calculation grid of 2.5 mm. The prescription dose was 66 Gy, aiming to cover 95% of the PTV using 5-8 coplanar 6MV X-ray beams. The same beam number were employed in all three-treatment plans for each patient. For aPlan, beam arrangements were defined based on the tumor volume's position to limit beam paths through the contralateral lung, without considering the functional lung geometry. Beam arrangements for fPlan were designed based on the tumor's position to limit beam paths through the HFV, while for rfPlan, the beams directions were also assigned to avoid the rLFV. The optimization of OARs dose included the spinal cord, esophagus, heart, and lungs relevant to each plan using RTOG 0617 guidelines [125] listed in Table 7.

Table 7: The dose constrain for organ at risk from RTOG 0617 guidelines [125]. Abbreviation: OAR, Organ at risk

OAR name	Constrain value
Lungs	$V20$ <37% Mean dose <20 Gy
Spinal cord	Max dose <47 Gy
Esophagus	Max dose <70 Gy Mean dose <34 Gy
Heart	Max dose <70 Gy $V45$ <66%

5.3 Results

5.3.1 Dose evaluation for functional lung avoidance treatment plans without rLFV

The dose comparison of the aPlan and fPlan for the 15 patients was presented in Table 8. Both plans had similar dose coverage for the targets. By implementing the functional information into treatment planning led to dose reduction for the HFV. The $V5$, $V20$ and mean dose of the HFV in fPlan were 6.5% ± 22.1%, 15.5% ± 23.0%, and 8.2% ± 13.7% lower, respectively, than those in aPlan. The $V5$, $V20$, and mean dose of lungs in fPlan were higher than in aPlan by 3.4% ± 8.0%, 5.9% ± 14.0%, and 2.6% ± 15.4%, respectively. Regarding other evaluation parameters, all three plans showed comparable results and remained within tolerance as shown in Table 8.

Table 8: The comparison of the dose value of organ at risk between aPlan abd fPlan. Abbreviation: OAR, Organ at risk; HFV, high functional volume.

OAR name	Parameter	aPlan	fPlan
HFV	Mean dose	8.1 ± 5.5 Gy	7.6 ± 5.3 Gy
	$V5$	26.3 ± 18.5%	24.8 ± 16.4%
	$V20$	15.4 ± 10.9%	14.2 ± 10.9%
Lungs	Mean dose	8.6 ± 2.9 Gy	8.9 ± 3.1 Gy
	$V20$	17.0 ± 5.8%	18.0 ± 7.0%
Spinal cord	Max dose	39.5 ± 6.4 Gy	38.3 ± 10.2 Gy
Esophagus	Max dose	53.2 ± 20.8 Gy	51.7 ± 22.7 Gy
	Mean dose	9.1 ± 5.7 Gy	9.5 ± 6.2 Gy
Heart	Max dose	48.2 ± 29.4 Gy	48.1 ± 29.7 Gy
	$V45$	2.4 ± 3.4%	2.4 ± 3.7%

5.3.2 Identify the temporary hypo-ventilation regions for the classification of the functional lung regions

Figure 23 illustrates the segmentation of the functional lung volume for two patients with tumors that blocked a segment before the treatment and subsequently shrank after the treatment. To enhance the preservation of lung function for these patients, the lung volume was divided into three distinct parts, each representing different functional regions. Figure 23 (A) and (D) demonstrate the contours of the HFV obtained from the $\mathrm{CTVI_{AW}}$, which represents the final version of the ventilation image considering both the parenchyma and the airway. Figure 23 (B) and (E) display the high functional ability volume in the temporarily blocked segment, referred to rLFV. By dividing the lung volume into these three parts, the treatment plan can better take into account the functional lung regions, particularly in cases where tumor-induced blockage affected specific segments initially but improved after treatment. This approach aims to preserve lung function more effectively during the treatment process.

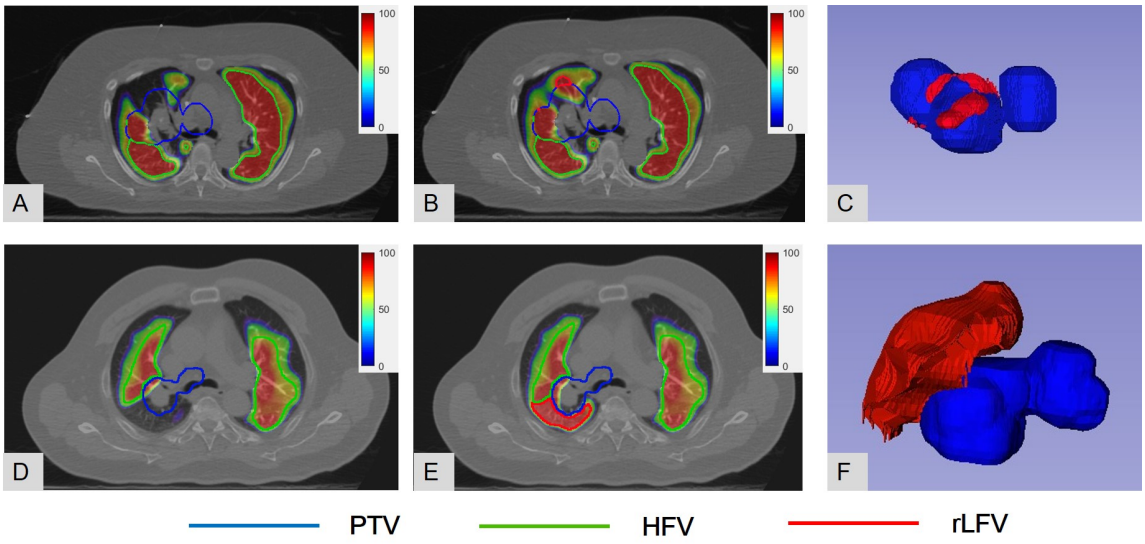

Figure 23: The two patients with the tumor blocked the segment before and shrank after the treatment. Figures (A)-(B) and Figures (D)-(E) are the $\mathrm{CTVI_{AW}}$ and the $\mathrm{CTVI_{SVD}}$ of the patient 1 and patient 2, respectively. In Figures (A) and (D), the blue contours represent the PTV, while the red contours represent the HFV. In Figures (B) and (E), the blue contours represent the PTV, while the red contours represent the rLFV in the tumor temporarily blocked segments. Figures (C) and (F) show the 3D view of the PTV and rLFV.

5.3.3 Dose evaluation for functional lung avoidance treatment plans with rLFV

The comparison of the dose distribution and the dose volume histogram (DVH) between aPlan, fPlan, and rfPlan for one typical patient is presented in Figure 24. During the treatment planning design of fPlan, doses were delivered to the tumor through the posterior segment in the right upper lobe to protect the HFV region as shown in Figure 24 (B). As a result, the fPlan and rfPlan demonstrated improvements in various parameters for HFV compared to aPlan as shown in Table 9. For the comparison of the five patients treatment plans, the $V5$, $V20$ and mean dose of the HFV in fPlan were 10.6% ± 25.3%, 14.3% ± 9.5%, and 10.0% ± 9.3% lower, respectively, than those in aPlan. By incorporating dose constraints to rLFV, the dose of rLFV in rfPlan was lower compared to fPlan and aPlan. As Figure 24 illustrates, the dose in the rLFV of fPlan was significantly higher than aPlan and rfPlan, with rfPlan showing the lowest dose. The $V5$, $V20$, and mean dose of rLFV in rfPlan were lower than in aPlan by 0.3% ± 0.5%, 12.1% ± 8.4%, and 13.0% ± 6.4%, respectively. These parameters in rfPlan were substantially lower than in fPlan by 1.0% ± 2.1%, 14.9% ± 9.8%, and 15.9% ± 6.5%, respectively. The dose to the HFV in rfPlan was similar to that in aPlan. Regarding other evaluation parameters, all three plans showed comparable results and remained within tolerance as shown in Table 9.

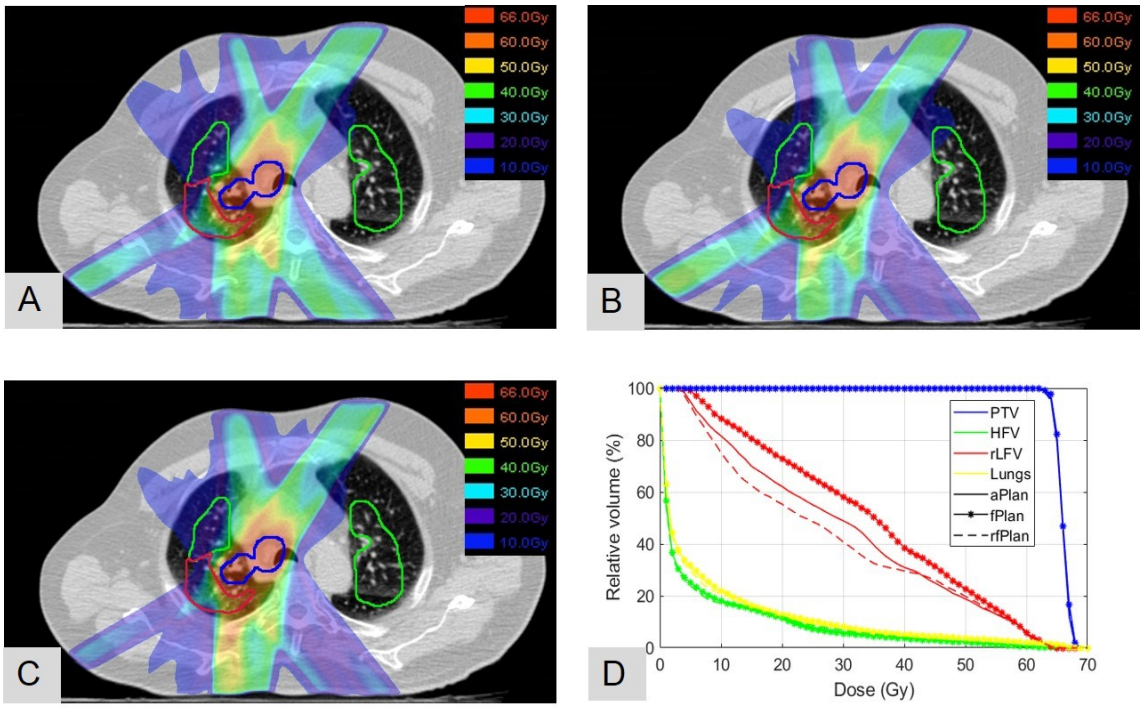

Figure 24: The comparison of the dose distribution between aPlan (A), fPlan (B), and rfPlan (C). D is the DVH comparison. Abbreviations, PTV: planning target volume, HFV: high functional volume, rLFV: recoverable low functional volume, aPlan: an anatomical-based plan, fPlan: a functional-guided plan that only considered HFV, and rfPlan: a functional-guided plan that protected both HFV and rLFV.

Table 9: The comparison of the dose value of organ at risk between aPlan, fPlan, and rfPlan. Abbreviation: OAR, Organ at risk; HFV, high functional volume; rLFV, recoverable low functional volume.

OAR name	Parameter	aPlan	fPlan	rfPlan
HFV	Mean dose	9.1 ± 1.6 Gy	8.2 ± 1.7 Gy	8.3 ± 1.7 Gy
	$V5$	46.1 ± 15.7%	38.4 ± 10.7%	38.7 ± 11.4%
	$V20$	13.0 ± 3.2%	11.1 ± 3.1%	11.3 ± 3.0%
rLFV	Mean dose	43.0 ± 11.5 Gy	44.2 ± 10.5 Gy	37.7 ± 12.2 Gy
	$V5$	99.1 ± 1.9%	100.0 ± 0.3%	98.8 ± 2.4%
	$V20$	88.8 ± 13.4%	91.3 ± 9.3%	78.3 ± 15.4%
Lungs	Mean dose	14.1 ± 3.4 Gy	14.1 ± 3.3 Gy	13.9 ± 3.4 Gy
	$V20$	23.8 ± 6.0%	23.9 ± 5.9%	23.3 ± 6.1%
Spinal cord	Max dose	42.2 ± 3.5 Gy	42.7 ± 2.3 Gy	43.2 ± 2.1 Gy
Esophagus	Max dose	62.4 ± 6.2 Gy	63.5 ± 4.7 Gy	64.2 ± 4.7 Gy
	Mean dose	15.7 ± 7.9 Gy	16.2 ± 8.2 Gy	15.8 ± 8.0 Gy
Heart	Max dose	65.2 ± 3.8 Gy	65.9 ± 2.9 Gy	65.8 ± 3.2 Gy
	$V45$	10.0 ± 12.0%	10.0 ± 10.8%	9.9 ± 10.1%

5.4 Summary and discussion

In this study, we proposed a novel functional lung avoidance treatment planning strategy based on anatomy-wise lung ventilation imaging. By using the Atlas-based pulmonary segments segmentation method, we can identify the blocked segments. After analyzing these blocked segments, the potential recoverable regions with high functional ability can be identified for careful protection during the treatment plan design, which can help patient preserve lung function after the radiation therapy. For the comparisons between aPlan, fPlan, and rfPlan of the five patients with rLFV, the V20 and mean dose of rLFV in rfPlan were lower than those in rfPlan by 12.1% and 13.0%, respectively, 14.9% and 15.9% lower than fPlan, respectively. This is the first study that takes into account the potentially recoverable lung defects in lung functional image guided planning.

For the five patients selected for treatment plan design in this study, the blocked segments were attached to the tumor. During the design of the treatment plan with multiple beams, the beams were selected to pass through the blocked segments since it can go through less lung volume compared to other beams for aPlan. For the fPlan, the blocked segments would be considered as a low function area and lots of dose would be deposited in these regions. In that case, even if the tumor disappears after the treatment, these regions may be damaged and cannot be able to regain function. By identifying this blocked region with our method before the treatment planning, the patient's lung function has the potential to increase after the treatment.

By classifying the high function region in the blocked segments, we can determine if the blocked segments needed protection before the treatment. It is important to note that this study is retrospective, so the tumor shrinkage (response to treatment)

information is acquired from the CT image obtained after the treatment. Except the lung parenchyma is normal, another reason that the blocked region can regain the function is the tumor shrink and no longer block the airway. Future research should develop models that can predict tumor response to identify if and how the blocked segments will be affected after treatment [126–130]. Furthermore, it is crucial to consider the type of tumor compression when interpreting model predictions, as the mechanisms and outcomes differ significantly between tumor invasion and external physical compression. In cases of tumor invasion, the malignant cells may infiltrate and damage the structural integrity of the airway, potentially leading to persistent obstruction even if the tumor size is reduced. This contrasts with external compression, where alleviating the physical pressure might more directly restore airway patency. Therefore, future studies should explicitly differentiate between these types of compression in the analyses, as this distinction is critical for accurately predicting treatment outcomes and understanding the underlying pathophysiology of airway obstruction. Incorporating this factor would improve the precision and clinical applicability of predictive models.

In this study, we assumed that the loss of the function in the lung was caused by airway blockage or lung parenchyma damage. The healthy lung parenchyma regions in temporarily blocked segments were identified as recoverable regions. The lung parenchyma of these recoverable regions was assumed to have similar features as the regions outside the blocked segments. The super-voxel-based method that was used to analyze the lung parenchyma damage that caused lung function loss was validated in 55 patients without an airway blockage and had a mean Spearman correlation of 0.60 ± 0.10. However, our direct use of this super-voxel-based method to classify

lung regions with healthy parenchyma in blocked segments as recoverable area needs to be verified using serial ventilation images. The validation could be challenge, since the some regions in the blocked segments have been irradiated and the characteristic of these regions could be change. The verification experiment need to collect the patients that shown tumor blocked before the treatment and tumor response and shown no tumor blocked after the treatment. The comparison may focus on the low dose regions and show no clear feature change in the blocked segments.

There were five patients among thirteen who met the treatment planning selection criteria in this study. Further validation is needed to determine if our treatment planning strategy can benefit a larger number of patients, particularly those with central-type lung cancer. However, individual treatment planning should consider various factors to achieve the most suitable plan for each patient. Another limitation of our study is the reliance on visual inspection for identifying the blocked segments, which can introduce inter-observer bias. Further research is needed to develop automated methods for recognizing the blocked segments.

6 Conclusions

In this study, we develop a novel anatomy-wise lung ventilation imaging method to generate surrogate ventilation images directly from CT images for functional lung avoidance radiotherapy planning. The anatomy-wise lung ventilation imaging method is based on the causes of the lung ventilation defect by considering the both air transport and the feature of lung parenchyma. For the anatomy-wise lung ventilation imaging method, it involves several key steps to generate and analyze the lung ventilation images. First, we develop an Atlas-based method to divide the lung into eighteen segments, which can help to identify the blocked segments. The blocked segments are defected regions caused by the airway blocked. Second, we develop a super-voxel-based method to analyze the feature of the lung parenchyma of the non-blocked segments and combine with the first step to generate the surrogate of the ventilation image. This method can yield moderate-to-high voxel-wise approximations of lung ventilation image. For the application of the anatomy-wise lung ventilation image into the treatment planning design, we analyze the feature of the blocked segments to identify and reduce the dose to the potential recoverable region which could become high function after the treatment if the tumor shrink. This is the first time that considering the recoverable regions into the treatment planning process, which has the potential to preserve more lung function for the patients. Our study can enhance the understanding of lung ventilation defect base on the CT images. The findings will contribute to the development of more precise and personalized treatment planning methods, ultimately leading to improved outcomes for lung cancer patients undergoing radiation therapy.

7 References

[1] Jacques Ferlay ME et al. “Global cancer statistics 2022: GLOBOCAN estimates of incidence and mortality worldwide for 36 cancers in 185 countries”. In: (2024).

[2] Shalini K Vinod and Eric Hau. “Radiotherapy treatment for lung cancer: Current status and future directions”. In: *Respirology* 25 (2020), pp. 61–71.

[3] Shirish M Gadgeel, Suresh S Ramalingam, and Gregory P Kalemkerian. “Treatment of lung cancer”. In: *Radiologic Clinics* 50.5 (2012), pp. 961–974.

[4] David S Ettinger et al. “Non–small cell lung cancer, version 3.2022, NCCN clinical practice guidelines in oncology”. In: *Journal of the National Comprehensive Cancer Network* 20.5 (2022), pp. 497–530.

[5] Hiroshi Onishi et al. “Stereotactic body radiotherapy (SBRT) for operable stage I non–small-cell lung cancer: can SBRT be comparable to surgery?” In: *International Journal of Radiation Oncology* Biology* Physics* 81.5 (2011), pp. 1352–1358.

[6] Joe Y Chang et al. “Stereotactic ablative radiotherapy versus lobectomy for operable stage I non-small-cell lung cancer: a pooled analysis of two randomised trials”. In: *The lancet oncology* 16.6 (2015), pp. 630–637.

[7] Joe Y Chang et al. “Stereotactic ablative radiotherapy for operable stage I non-small-cell lung cancer (revised STARS): long-term results of a single-arm, prospective trial with prespecified comparison to surgery”. In: *The Lancet Oncology* 22.10 (2021), pp. 1448–1457.

[8] Varsha Jain and Abigail T Berman. “Radiation pneumonitis: old problem, new tricks”. In: *Cancers* 10.7 (2018), p. 222.

[9] Mandeep Singh Rahi et al. “Radiation-induced lung injury—current perspectives and management”. In: *Clinics and Practice* 11.3 (2021), pp. 410–429.

[10] Lorena Giuranno et al. “Radiation-induced lung injury (RILI)”. In: *Frontiers in oncology* 9 (2019), p. 877.

[11] Vivek Mehta. “Radiation pneumonitis and pulmonary fibrosis in non–small-cell lung cancer: Pulmonary function, prediction, and prevention”. In: *International journal of radiation oncology* biology* physics* 63.1 (2005), pp. 5–24.

[12] Jeffrey D Bradley et al. “Standard-dose versus high-dose conformal radiotherapy with concurrent and consolidation carboplatin plus paclitaxel with or without cetuximab for patients with stage IIIA or IIIB non-small-cell lung cancer (RTOG 0617): a randomised, two-by-two factorial phase 3 study”. In: *The lancet oncology* 16.2 (2015), pp. 187–199.

[13] Hoon K Lee et al. “Postoperative pulmonary complications after preoperative chemoradiation for esophageal carcinoma: correlation with pulmonary dose–volume histogram parameters”. In: *International Journal of Radiation Oncology* Biology* Physics* 57.5 (2003), pp. 1317–1322.

[14] Joseph M Baisden et al. “Dose as a function of lung volume and planned treatment volume in helical tomotherapy intensity-modulated radiation therapy-based stereotactic body radiation therapy for small lung tumors”. In: *International Journal of Radiation Oncology* Biology* Physics* 68.4 (2007), pp. 1229–1237.

[15] Douglas A Hoover et al. “SPECT-based functional lung imaging for the prediction of radiation pneumonitis: A clinical and dosimetric correlation”. In: *Journal of medical imaging and radiation oncology* 58.2 (2014), pp. 214–222.

[16] Soo Jin Lee and Hae Jin Park. “Single photon emission computed tomography (SPECT) or positron emission tomography (PET) imaging for radiotherapy planning in patients with lung cancer: a meta-analysis”. In: *Scientific Reports* 10.1 (2020), p. 14864.

[17] Yevgeniy Vinogradskiy et al. “Results of a multi-institutional phase 2 clinical trial for 4DCT-ventilation functional avoidance thoracic radiation therapy”. In: *International Journal of Radiation Oncology* Biology* Physics* 112.4 (2022), pp. 986–995.

[18] Nicholas W Bucknell et al. “Functional lung imaging in radiation therapy for lung cancer: A systematic review and meta-analysis”. In: *Radiotherapy and Oncology* 129.2 (2018), pp. 196–208.

[19] Liesbeth J Boersma et al. “Recovery of overall and local lung function loss 18 months after irradiation for malignant lymphoma.” In: *Journal of clinical oncology* 14.5 (1996), pp. 1431–1441.

[20] JCM Theuws et al. “Dose–effect relations for early local pulmonary injury after irradiation for malignant lymphoma and breast cancer”. In: *Radiotherapy and Oncology* 48.1 (1998), pp. 33–43.

[21] Yvette Seppenwoolde et al. “Radiation dose-effect relations and local recovery in perfusion for patients with non–small-cell lung cancer”. In: *International Journal of Radiation Oncology* Biology* Physics* 47.3 (2000), pp. 681–690.

[22] Daniel Rocky Owen et al. “Modeling patient-specific dose-function response for enhanced characterization of personalized functional damage”. In: *International Journal of Radiation Oncology* Biology* Physics* 102.4 (2018), pp. 1265–1275.

[23] Yvette Seppenwoolde et al. “Optimizing radiation treatment plans for lung cancer using lung perfusion information”. In: *Radiotherapy and oncology* 63.2 (2002), pp. 165–177.

[24] Judith A Christian et al. “The incorporation of SPECT functional lung imaging into inverse radiotherapy planning for non-small cell lung cancer”. In: *Radiotherapy and oncology* 77.3 (2005), pp. 271–277.

[25] Sarah M McGuire et al. “A methodology for using SPECT to reduce intensity-modulated radiation therapy (IMRT) dose to functioning lung”. In: *International Journal of Radiation Oncology* Biology* Physics* 66.5 (2006), pp. 1543–1552.

[26] Yoshiyuki Shioyama et al. “Preserving functional lung using perfusion imaging and intensity-modulated radiation therapy for advanced-stage non–small cell lung cancer”. In: *International Journal of Radiation Oncology* Biology* Physics* 68.5 (2007), pp. 1349–1358.

[27] Konstantin Lavrenkov et al. “A potential to reduce pulmonary toxicity: the use of perfusion SPECT with IMRT for functional lung avoidance in radiotherapy of non-small cell lung cancer”. In: *Radiotherapy and oncology* 83.2 (2007), pp. 156–162.

[28] Iram Munawar et al. “Intensity modulated radiotherapy of non-small-cell lung cancer incorporating SPECT ventilation imaging”. In: *Medical physics* 37.4 (2010), pp. 1863–1872.

[29] Giulia Anna Follacchio et al. “Functional lung volume mapping with perfusion Single-Photon Emission Computed Tomography scan for radiotherapy planning in patients with locally advanced nonsmall cell lung cancer”. In: *Nuclear Medicine Communications* 41.10 (2020), pp. 1026–1033.

[30] Shankar Siva et al. “High-resolution pulmonary ventilation and perfusion PET/CT allows for functionally adapted intensity modulated radiotherapy in lung cancer”. In: *Radiotherapy and Oncology* 115.2 (2015), pp. 157–162.

[31] Gazi Md Daud Iqbal et al. “Four-dimensional computed tomography-based ventilation imaging in intensity-modulated radiation therapy treatment planning for pulmonary functional avoidance”. In: *Journal of Applied Clinical Medical Physics* 24.6 (2023), e13920.

[32] Kazuyoshi Suga et al. “Clinical utility of co-registered respiratory-gated 99m Tc-Technegas/MAA SPECT-CT images in the assessment of regional lung functional impairment in patients with lung cancer”. In: *European journal of nuclear medicine and molecular imaging* 31 (2004), pp. 1280–1290.

[33] SJ Ament et al. “PET lung ventilation/perfusion imaging using 68 Ga aerosol (Galligas) and 68 Ga-labeled macroaggregated albumin”. In: *Theranostics, Gallium-68, and Other Radionuclides: A Pathway to Personalized Diagnosis and Treatment*. Springer. 2013, pp. 395–423.

[34] John Kipritidis et al. “The VAMPIRE challenge: a multi-institutional validation study of CT ventilation imaging”. In: *Medical physics* 46.3 (2019), pp. 1198–1217.

[35] Geoffrey P Schembri et al. “Artifacts and anatomical variants affecting ventilation and perfusion lung imaging”. In: *Seminars in nuclear medicine*. Vol. 45. 5. Elsevier. 2015, pp. 373–391.

[36] Justus E Roos et al. “Hyperpolarized gas MR imaging: technique and applications”. In: *Magnetic Resonance Imaging Clinics* 23.2 (2015), pp. 217–229.

[37] Jing Cai et al. “MR grid-tagging using hyperpolarized helium-3 for regional quantitative assessment of pulmonary biomechanics and ventilation”. In: *Magnetic Resonance in Medicine: An Official Journal of the International Society for Magnetic Resonance in Medicine* 58.2 (2007), pp. 373–380.

[38] Jing Cai et al. “Dynamic MRI of grid-tagged hyperpolarized helium-3 for the assessment of lung motion during breathing”. In: *International Journal of Radiation Oncology* Biology* Physics* 75.1 (2009), pp. 276–284.

[39] Nicholas J Tustison et al. “Pulmonary kinematics from tagged hyperpolarized helium-3 MRI”. In: *Journal of Magnetic Resonance Imaging: An Official Journal of the International Society for Magnetic Resonance in Medicine* 31.5 (2010), pp. 1236–1241.

[40] Yevgeniy Vinogradskiy. “CT-based ventilation imaging in radiation oncology”. In: *BJR—Open* 1.1 (2019), p. 20180035.

[41] Adam Szmul et al. “Patch-based lung ventilation estimation using multi-layer supervoxels”. In: *Computerized Medical Imaging and Graphics* 74 (2019), pp. 49–60.

[42] Edward Castillo et al. “On the spatial correlation between robust CT-ventilation methods and SPECT ventilation”. In: *Medical physics* 47.11 (2020), pp. 5731–5738.

[43] John Kipritidis et al. “Estimating lung ventilation directly from 4D CT Hounsfield unit values”. In: *Medical physics* 43.1 (2016), pp. 33–43.

[44] Ge Ren et al. “Investigation of a novel deep learning-based computed tomography perfusion mapping framework for functional lung avoidance radiotherapy”. In: *Frontiers in Oncology* 11 (2021), p. 644703.

[45] Ge Ren et al. “Deep learning-based computed tomography perfusion mapping (DL-CTPM) for pulmonary CT-to-perfusion translation”. In: *International Journal of Radiation Oncology* Biology* Physics* 110.5 (2021), pp. 1508–1518.

[46] Yuncheng Zhong et al. “Deriving ventilation imaging from 4 DCT by deep convolutional neural network”. In: *Medical physics* 46.5 (2019), pp. 2323–2329.

[47] Zhiqiang Liu et al. “A deep learning method for producing ventilation images from 4DCT: First comparison with technegas SPECT ventilation”. In: *Medical Physics* 47.3 (2020), pp. 1249–1257.

[48] Kirk A Frey et al. “Changes in global function and regional ventilation and perfusion on SPECT during the course of radiotherapy in patients with non-small-cell lung cancer”. In: *International Journal of Radiation Oncology* Biology* Physics* 82.4 (2012), e631–e638.

[49] Xue Meng et al. “Changes in functional lung regions during the course of radiation therapy and their potential impact on lung dosimetry for non-small cell lung cancer”. In: *International Journal of Radiation Oncology* Biology* Physics* 89.1 (2014), pp. 145–151.

[50] John Kipritidis et al. “Measuring interfraction and intrafraction lung function changes during radiation therapy using four-dimensional cone beam CT ventilation imaging”. In: *Medical physics* 42.3 (2015), pp. 1255–1267.

[51] Tokihiro Yamamoto et al. “Changes in regional ventilation during treatment and dosimetric advantages of CT ventilation image guided radiation therapy for locally advanced lung cancer”. In: *International Journal of Radiation Oncology* Biology* Physics* 102.4 (2018), pp. 1366–1373.

[52] Paula Ugalde, Jose de Jesus Camargo, and Jean Deslauriers. “Lobes, fissures, and bronchopulmonary segments”. In: *Thoracic surgery clinics* 17.4 (2007), pp. 587–599.

[53] Jan-Martin Kuhnigk et al. “New tools for computer assistance in thoracic CT. Part 1. Functional analysis of lungs, lung lobes, and bronchopulmonary segments”. In: *Radiographics* 25.2 (2005), pp. 525–536.

[54] Christina Stoecker et al. “Determination of lung segments in computed tomography images using the Euclidean distance to the pulmonary artery”. In: *Medical Physics* 40.9 (2013), p. 091912.

[55] Zhi Chen et al. “Deep learning-based bronchial tree-guided semi-automatic segmentation of pulmonary segments in computed tomography images”. In: *Quantitative Imaging in Medicine and Surgery* 14.2 (2024), p. 1636.

[56] Hisashi Saji et al. “Segmentectomy versus lobectomy in small-sized peripheral non-small-cell lung cancer (JCOG0802/WJOG4607L): a multicentre, open-label, phase 3, randomised, controlled, non-inferiority trial”. In: *The Lancet* 399.10335 (2022), pp. 1607–1617.

[57] Nasser Altorki et al. “Lobar or sublobar resection for peripheral stage IA non–small-cell lung cancer”. In: *New England Journal of Medicine* 388.6 (2023), pp. 489–498.

[58] Eva M Van Rikxoort et al. “Automatic segmentation of pulmonary segments from volumetric chest CT scans”. In: *IEEE transactions on medical imaging* 28.4 (2009), pp. 621–630.

[59] Kaiming Kuang et al. “What makes for automatic reconstruction of pulmonary segments”. In: *International Conference on Medical Image Computing and Computer-Assisted Intervention*. Springer. 2022, pp. 495–505.

[60] Xinya Zhao et al. “Bronchial anatomy of left lung: a study of multi-detector row CT”. In: *Surgical and radiologic anatomy* 31 (2009), pp. 85–91.

[61] Asha Kandathil and Murthy Chamarthy. “Pulmonary vascular anatomy & anatomical variants”. In: *Cardiovascular diagnosis and therapy* 8.3 (2018), p. 201.

[62] Brett A Simon. “Non-invasive imaging of regional lung function using x-ray computed tomography”. In: *Journal of clinical monitoring and computing* 16 (2000), pp. 433–442.

[63] Joseph M Reinhardt et al. “Registration-based estimates of local lung tissue expansion compared to xenon CT measures of specific ventilation”. In: *Medical image analysis* 12.6 (2008), pp. 752–763.

[64] Peng Xue et al. “Effective lung ventilation estimation based on 4D CT image registration and supervoxels”. In: *Biomedical Signal Processing and Control* 79 (2023), p. 104074.

[65] Edward Castillo et al. “Robust CT ventilation from the integral formulation of the Jacobian”. In: *Medical physics* 46.5 (2019), pp. 2115–2125.

[66] Edward Castillo, Yevgeniy Vinogradskiy, and Richard Castillo. “Robust hu-based ct ventilation from an integrated mass conservation formulation”. In: *Medical physics* 46.11 (2019), pp. 5036–5046.

[67] Radhakrishna Achanta et al. “SLIC superpixels compared to state-of-the-art superpixel methods”. In: *IEEE transactions on pattern analysis and machine intelligence* 34.11 (2012), pp. 2274–2282.

[68] Yuan Tian et al. “Availability of a simplified lung ventilation imaging algorithm based on four-dimensional computed tomography”. In: *Physica Medica* 65 (2019), pp. 53–58.

[69] Zhenyu Yang et al. “Quantification of lung function on CT images based on pulmonary radiomic filtering”. In: *Medical Physics* 49.11 (2022), pp. 7278–7286.

[70] Kyle J Lafata et al. “An exploratory radiomics approach to quantifying pulmonary function in CT images”. In: *Scientific reports* 9.1 (2019), p. 11509.

[71] Yu-Hua Huang et al. “Respiratory Invariant Textures From Static Computed Tomography Scans for Explainable Lung Function Characterization”. In: *Journal of Thoracic Imaging* 38.5 (2023), pp. 286–296.

[72] Yvette Seppenwoolde et al. “Regional differences in lung radiosensitivity after radiotherapy for non–small-cell lung cancer”. In: *International Journal of Radiation Oncology* Biology* Physics* 60.3 (2004), pp. 748–758.

[73] Yevgeniy Vinogradskiy et al. “Use of 4-dimensional computed tomography-based ventilation imaging to correlate lung dose and function with clinical outcomes”. In: *International Journal of Radiation Oncology* Biology* Physics* 86.2 (2013), pp. 366–371.

[74] Katherina P Farr et al. “Inclusion of functional information from perfusion SPECT improves predictive value of dose–volume parameters in lung toxicity outcome after radiotherapy for non-small cell lung cancer: A prospective study”. In: *Radiotherapy and Oncology* 117.1 (2015), pp. 9–16.

[75] Tomoki Kimura et al. “Combined ventilation and perfusion imaging correlates with the dosimetric parameters of radiation pneumonitis in radiation therapy planning for lung cancer”. In: *International Journal of Radiation Oncology* Biology* Physics* 93.4 (2015), pp. 778–787.

[76] Lawrence B Marks et al. “The utility of SPECT lung perfusion scans in minimizing and assessing the physiologic consequences of thoracic irradiation”. In: *International Journal of Radiation Oncology* Biology* Physics* 26.4 (1993), pp. 659–668.

[77] Brian P Yaremko et al. “Reduction of normal lung irradiation in locally advanced non–small-cell lung cancer patients, using ventilation images for functional avoidance”. In: *International Journal of Radiation Oncology* Biology* Physics* 68.2 (2007), pp. 562–571.

[78] Rob H Ireland et al. “Feasibility of image registration and intensity-modulated radiotherapy planning with hyperpolarized helium-3 magnetic resonance imaging for non–small-cell lung cancer”. In: *International Journal of Radiation Oncology* Biology* Physics* 68.1 (2007), pp. 273–281.

[79] Emma L Bates et al. “Functional image-based radiotherapy planning for non-small cell lung cancer: A simulation study”. In: *Radiotherapy and Oncology* 93.1 (2009), pp. 32–36.

[80] Tokihiro Yamamoto et al. “Impact of four-dimensional computed tomography pulmonary ventilation imaging-based functional avoidance for lung cancer radiotherapy”. In: *International Journal of Radiation Oncology* Biology* Physics* 79.1 (2011), pp. 279–288.

[81] Timothy Waxweiler et al. “A complete 4 DCT-ventilation functional avoidance virtual trial: Developing strategies for prospective clinical trials”. In: *Journal of applied clinical medical physics* 18.3 (2017), pp. 144–152.

[82] Yoshiro Ieko et al. “The impact of 4DCT-ventilation imaging-guided proton therapy on stereotactic body radiotherapy for lung cancer”. In: *Radiological Physics and Technology* 13 (2020), pp. 230–237.

[83] Nobuko Utsumi et al. “VMAT Planning With Xe-CT Functional Images Enables Radiotherapy Planning With Consideration of Lung Function”. In: *Cancer Diagnosis & Prognosis* 1.3 (2021), p. 193.

[84] Yi Ding et al. “A pilot study of function-based radiation therapy planning for lung cancer using hyperpolarized xenon-129 ventilation MRI”. In: *Journal of Applied Clinical Medical Physics* 23.3 (2022), e13502.

[85] Jing Cai et al. “Helical tomotherapy planning for lung cancer based on ventilation magnetic resonance imaging”. In: *Medical Dosimetry* 36.4 (2011), pp. 389–396.

[86] Noriyuki Kadoya et al. “Dosimetric impact of 4-dimensional computed tomography ventilation imaging-based functional treatment planning for stereotactic body radiation therapy with 3-dimensional conformal radiation therapy”. In: *Practical radiation oncology* 5.5 (2015), e505–e512.

[87] Shankar Siva et al. “Ga-68 MAA perfusion 4D-PET/CT scanning allows for functional lung avoidance using conformal radiation therapy planning”. In: *Technology in cancer research & treatment* 15.1 (2016), pp. 114–121.

[88] Austin M Faught et al. “Evaluating the toxicity reduction with computed tomographic ventilation functional avoidance radiation therapy”. In: *International Journal of Radiation Oncology* Biology* Physics* 99.2 (2017), pp. 325–333.

[89] Yevgeniy Vinogradskiy et al. “Interim analysis of a two-institution, prospective clinical trial of 4DCT-ventilation-based functional avoidance radiation therapy”. In: *International Journal of Radiation Oncology* Biology* Physics* 102.4 (2018), pp. 1357–1365.

[90] Katherina P Farr et al. “Functional perfusion image guided radiation treatment planning for locally advanced lung cancer”. In: *Physics and Imaging in Radiation Oncology* 11 (2019), pp. 76–81.

[91] Faegheh S Mounessi et al. “Image-based lung functional radiotherapy planning for non-small cell lung cancer”. In: *Strahlentherapie und Onkologie* 196 (2020), pp. 151–158.

[92] Jingjing M Dougherty et al. “Functional avoidance-based intensity modulated proton therapy with 4DCT derived ventilation imaging for lung cancer”. In: *Journal of applied clinical medical physics* 22.7 (2021), pp. 276–285.

[93] Qijie Huang et al. “Dosimetric feasibility of 4DCT-ventilation imaging guided proton therapy for locally advanced non-small-cell lung cancer”. In: *Radiation Oncology* 13 (2018), pp. 1–10.

[94] Yevgeniy Y Vinogradskiy et al. “Use of weekly 4DCT-based ventilation maps to quantify changes in lung function for patients undergoing radiation therapy”. In: *Medical physics* 39.1 (2012), pp. 289–298.

[95] Douglas A Hoover et al. “Functional lung avoidance for individualized radiotherapy (FLAIR): study protocol for a randomized, double-blind clinical trial”. In: *BMC cancer* 14 (2014), pp. 1–10.

[96] Nicholas Bucknell et al. “Single-arm prospective interventional study assessing feasibility of using gallium-68 ventilation and perfusion PET/CT to avoid functional lung in patients with stage III non-small cell lung cancer”. In: *BMJ open* 10.12 (2020), e042465.

[97] Tokihiro Yamamoto et al. “Four-dimensional computed tomography ventilation image-guided lung functional avoidance radiation therapy: A single-arm prospective pilot clinical trial”. In: *International Journal of Radiation Oncology* Biology* Physics* 115.5 (2023), pp. 1144–1154.

[98] N Drenkow et al. “A systematic review of robustness in deep learning for computer vision: Mind the gap? arXiv 2021”. In: *arXiv preprint arXiv:2112.00639* ().

[99] Sata Busayarat and Tatjana Zrimec. “Detection of Bronchopulmonary Segments on High-Resolution CT–Preliminary Results”. In: *Twentieth IEEE International Symposium on Computer-Based Medical Systems (CBMS’07)*. IEEE. 2007, pp. 199–204.

[100] Hao Tang, Chupeng Zhang, and Xiaohui Xie. "Automatic pulmonary lobe segmentation using deep learning". In: *2019 IEEE 16th international symposium on biomedical imaging (ISBI 2019)*. IEEE. 2019, pp. 1225–1228.

[101] Minghui Zhang et al. "Cfda: Collaborative feature disentanglement and augmentation for pulmonary airway tree modeling of covid-19 cts". In: *International conference on medical image computing and computer-assisted intervention*. Springer. 2022, pp. 506–516.

[102] Hao Zheng et al. "Alleviating class-wise gradient imbalance for pulmonary airway segmentation". In: *IEEE transactions on medical imaging* 40.9 (2021), pp. 2452–2462.

[103] Weihao Yu et al. "Break: Bronchi reconstruction by geodesic transformation and skeleton embedding". In: *2022 IEEE 19th International Symposium on Biomedical Imaging (ISBI)*. IEEE. 2022, pp. 1–5.

[104] Yulei Qin et al. "Airwaynet: a voxel-connectivity aware approach for accurate airway segmentation using convolutional neural networks". In: *International conference on medical image computing and computer-assisted intervention*. Springer. 2019, pp. 212–220.

[105] Minghui Zhang et al. "Multi-site, Multi-domain Airway Tree Modeling". In: *Medical Image Analysis* 90 (2023), p. 102957.

[106] Enid M Eslick et al. "CT ventilation imaging derived from breath hold CT exhibits good regional accuracy with Galligas PET (CT-vs-PET-Ventilation-Imaging) (Version 1) [Data set]". In: *The Cancer Imaging Archive* (2022). https://doi.org/10.7937/3ppx-7s22.

[107] Tokihiro Yamamoto et al. "Pulmonary ventilation imaging based on 4-dimensional computed tomography: comparison with pulmonary function tests and SPECT ventilation images". In: *International Journal of Radiation Oncology* Biology* Physics* 90.2 (2014), pp. 414–422.

[108] Michael S Hofman et al. "68Ga PET/CT ventilation–perfusion imaging for pulmonary embolism: a pilot study with comparison to conventional scintigraphy". In: *Journal of Nuclear Medicine* 52.10 (2011), pp. 1513–1519.

[109] Jason Callahan et al. “High-resolution imaging of pulmonary ventilation and perfusion with 68 Ga-VQ respiratory gated (4-D) PET/CT”. In: *European journal of nuclear medicine and molecular imaging* 41 (2014), pp. 343–349.

[110] Shankar Siva et al. “A prospective observational study of Gallium-68 ventilation and perfusion PET/CT during and after radiotherapy in patients with non-small cell lung cancer”. In: *BMC cancer* 14 (2014), pp. 1–8.

[111] Johannes Hofmanninger et al. “Automatic lung segmentation in routine imaging is primarily a data diversity problem, not a methodology problem”. In: *European Radiology Experimental* 4 (2020), pp. 1–13.

[112] Fausto Milletari, Nassir Navab, and Seyed-Ahmad Ahmadi. “V-net: Fully convolutional neural networks for volumetric medical image segmentation”. In: *2016 fourth international conference on 3D vision (3DV)*. Ieee. 2016, pp. 565–571.

[113] RM Whitaker and EC Osmundson. “Prolonged Time of Lung Collapse Associated With Decreased Recovery of Functional Lung Following Palliative Radiotherapy”. In: *International Journal of Radiation Oncology, Biology, Physics* 111.3 (2021), S118–S119.

[114] JM Goldman et al. “Physiological effect of endobronchial radiotherapy in patients with major airway occlusion by carcinoma.” In: *Thorax* 48.2 (1993), pp. 110–114.

[115] GJG Rees et al. “Palliative radiotherapy for lung cancer: two versus five fractions”. In: *Clinical Oncology* 9.2 (1997), pp. 90–95.

[116] Ren and Malik. “Learning a classification model for segmentation”. In: *Proceedings ninth IEEE international conference on computer vision*. IEEE. 2003, pp. 10–17.

[117] Alex Zwanenburg et al. “The image biomarker standardization initiative: standardized quantitative radiomics for high-throughput image-based phenotyping”. In: *Radiology* 295.2 (2020), pp. 328–338.

[118] Alicia Chen et al. “Quantitative CT analysis of diffuse lung disease”. In: *Radiographics* 40.1 (2020), pp. 28–43.

[119] Robin Smithuis. “Chest X-Ray - Lung disease Four-Pattern Approach”. In: *radiologyassistant* (2014). https://radiologyassistant.nl/chest/chest-x-ray/lung-disease.

[120] Shine Raju, Subha Ghosh, and Atul C Mehta. “Chest CT signs in pulmonary disease: a pictorial review”. In: *Chest* 151.6 (2017), pp. 1356–1374.

[121] Christina Schröder et al. “Changes in pulmonary function and influencing factors after high-dose intrathoracic radio (chemo) therapy”. In: *Strahlentherapie und Onkologie* 193.2 (2017), p. 125.

[122] Zhi Chen et al. “A super-voxel-based method for generating surrogate lung ventilation images from CT”. In: *Frontiers in Physiology* 14 (2023), p. 1085158.

[123] Salim Balik et al. “Evaluation of 4-dimensional computed tomography to 4-dimensional cone-beam computed tomography deformable image registration for lung cancer adaptive radiation therapy”. In: *International Journal of Radiation Oncology* Biology* Physics* 86.2 (2013), pp. 372–379.

[124] Geoffrey D Hugo et al. “A longitudinal four-dimensional computed tomography and cone beam computed tomography dataset for image-guided radiation therapy research in lung cancer”. In: *Medical physics* 44.2 (2017), pp. 762–771.

[125] Jeffrey D Bradley et al. “Long-term results of NRG oncology RTOG 0617: standard-versus high-dose chemoradiotherapy with or without cetuximab for unresectable stage III non–small-cell lung cancer”. In: *Journal of Clinical Oncology* 38.7 (2020), p. 706.

[126] Jiabao Sheng et al. “Multi-view contrastive learning with additive margin for adaptive nasopharyngeal carcinoma radiotherapy prediction”. In: *Proceedings of the 2023 ACM International Conference on Multimedia Retrieval*. 2023, pp. 555–559.

[127] Madhurima R Chetan and Fergus V Gleeson. “Radiomics in predicting treatment response in non-small-cell lung cancer: current status, challenges and future perspectives”. In: *European radiology* 31 (2021), pp. 1049–1058.

[128] Yiwen Xu et al. “Deep learning predicts lung cancer treatment response from serial medical imaging”. In: *Clinical Cancer Research* 25.11 (2019), pp. 3266–3275.

[129] Yoshiharu Ohno et al. “Diffusion-weighted MRI versus 18F-FDG PET/CT: performance as predictors of tumor treatment response and patient survival in patients with non–small cell lung cancer receiving chemoradiotherapy”. In: *American Journal of Roentgenology* 198.1 (2012), pp. 75–82.

[130] Jacob T Antunes et al. “RADIomic Spatial TexturAl descripTor (RADISTAT): Quantifying spatial organization of imaging heterogeneity associated with tumor response to treatment”. In: *IEEE journal of biomedical and health informatics* 26.6 (2022), pp. 2627–2636.